

**EVOLUTION OF STRESS AND SEISMICITY IN  
FRACTURED GEOTHERMAL RESERVOIRS**

Zur Erlangung des akademischen Grades eines

DOKTORS DER NATURWISSENSCHAFTEN

von der Fakultät

Bauingenieur-, Geo- und Umweltwissenschaften

des Karlsruher Instituts für Technologie (KIT)

genehmigte

DISSERTATION

von

Dipl.-Geophys. Martin Schoenball

aus Freital

Tag der mündlichen

Prüfung: 05. Mai 2014

Referent: Prof. Dr. Thomas Kohl

Korreferent: Prof. Dr. Friedemann Wenzel

Karlsruhe 2014



---

## ABSTRACT

---

Geothermal power has the potential to contribute a good share of future energy needs. The International Energy Agency estimates that by 2050, geothermal will deliver about 3.5 % of the world-wide power production. The technology of enhanced geothermal systems (EGS) will play an important role in the geothermal future. To develop the hot rock in the subsurface, wells are drilled to three kilometers and more. By high pressure injection of fluids, pre-existing fractures are enlarged or new fluid pathways are created. Currently, the EGS technology is still under research and development, with only small power plants and several obstacles on the path to future large scale application with power plants in the order of 100 MW.

Besides reduction of drilling costs and maintaining long-term production, the mitigation and control of induced seismicity has become a major challenge for the future of EGS. At the Deep Heat Mining Project Basel, a magnitude 3.4 event was induced during the development phase. Following a comprehensive risk assessment study, the project was finally abandoned and large investments were lost.

The goal of this thesis is an improved understanding of seismicity induced in the surrounding of EGS. I analyze seismicity induced during the development of the EGS at Soultz-sous-Forêts (France). The project in Soultz was initiated in 1987 as the European pilot site and has more than 25 year of experience in developing an EGS. During this period, a database which is unique worldwide was assembled, making Soultz the most advanced EGS project so far.

The main part of this thesis consists of an analysis of the stimulation of well GPK2, conducted in June and July 2000. During the six days of stimulation, 23 400 m<sup>3</sup> of water were injected under pressures as high as 14.5 MPa. The surface seismometer network allowed localization of 7215 events. Focal mechanism solutions of 715 events with M > 1 could be obtained. This dataset, courtesy of Université de Strasbourg and GEIE Heat Mining, Soultz, forms the basis of the studies.

The PhD project was conducted partly within the FP7 GEISER (Geothermal Engineering Integrating Mitigation of Induced Seismicity in Reservoirs) project, funded by the European Commission and it benefited largely from fruitful collaborations with Université de Strasbourg, Geowatt AG, Zürich, GFZ German Research Centre for Geosciences, Potsdam and CSIRO Earth Science and Resources Engineering, Perth.

In the first study, I analyze whether interaction of seismicity by static stress transfer plays a significant role on the spatio-temporal

evolution of seismicity. I follow an analytical approach to compute the displacement field of a rectangular earthquake source. Through stacking of several sources, realistic slip distributions are obtained. The analysis reveals seemingly random distributed patches of stress increase and stress decrease of less than  $\pm 1$  MPa, except for very localized areas. Since the fracture planes have varying orientations, they form a volumetric fracture network. About 60 % of hypocenters are found in areas with increased Coulomb stress where their potential for failure was increased by static stress transfer. A different behavior is observed for slippage of neighboring asperities on larger fault zones. Here, failure of asperities leads to a direct stress increase in adjacent asperities, which are then more likely to fail. This is exemplified on a cluster of events occurring on the largest fault zone in Soultz, after shut-in of the well GPK2.

Subsequently, the peculiar behavior of seismicity and the hydraulic regime following shut-in of the well GPK2 is highlighted and investigated by further analysis of focal mechanism solutions. An increase of the thrust faulting component following shut-in is observed. The changes of the stress field are derived from spatio-temporally resolved inversions of focal mechanism solutions. A very strong reduction of the maximum horizontal stress and an increase of the minimum horizontal stress is revealed, which leads to a change of the stress regime from a transitional strike-slip / normal faulting regime to a pure normal faulting regime. This is the reason, why almost only normal faulting events are observed during the stimulation. These stress changes are not compatible with the coseiseismic stress changes. Thus, a large proportion of aseismic movements during the stimulation of well GPK2 is proposed.

In the next study I focus on time-dependency in geomechanics in connection with stress transfer. In a numerical finite element model a time-dependent failure criterion combined with a damage mechanics approach is used to study time-dependency of borehole breakout development. The failure criterion is based on the observation of creep failure at loads considerably lower than the short-term strength of the rock samples. It is shown that breakouts grow both in width and depth. Through progressive stress transfer to neighboring elements peak loads at the wellbore wall are reduced and breakout growth slows down. The rate of breakout growth follows Omori's law, which is used in seismology to describe the decline of aftershock activity following a main shock.

---

## ZUSAMMENFASSUNG

---

Die geothermische Energiegewinnung hat das Potenzial, zum Energiemix der Zukunft einen beträchtlichen Teil beizutragen. Die Internationale Energie Agentur (IEA) schätzt, dass im Jahr 2050 3,5 % der weltweiten Stromproduktion durch Nutzung der Geothermie erzielt werden kann. Dabei soll mittels der EGS-Technologie (*enhanced geothermal system*) den ingenieurtechnisch verbesserten geothermischen Reservoirn eine zentrale Rolle zukommen. Hierbei werden Bohrungen von über drei Kilometern Länge abgeteuft, um das heiße Gestein im Untergrund zu erschließen. Durch Verpressen von Fluiden, zu meist Frischwasser, unter hohem Druck kann das Gestein aufgebrochen werden um natürliche Klüfte zu weiten oder neue Fluidwegsamkeiten zu schaffen. Derzeit befindet sich die EGS-Technologie jedoch noch in der Erprobungsphase mit nur kleinen Kraftwerken und zahlreichen Hindernissen auf dem Weg zur großtechnischen Anwendung für Kraftwerken der Größenordnung von 100 MW.

Neben der Reduzierung der Bohrkosten sowie der Sicherung des Langzeitbetriebs hat sich die Reduzierung induzierter Seismizität zu einer der großen Herausforderungen, für einen breiten Einsatz dieser Technologie entwickelt. So wurde zum Beispiel beim geplanten EGS-Projekt in Basel während der Entwicklungsphase des EGS ein Erdbeben der Magnitude 3,4 ausgelöst. Einem Gutachten zur Risikobewertung folgend, wurde das Projekt daraufhin eingestellt, was finanzielle Verluste in Millionenhöhe mit sich brachte.

Das Ziel der vorliegenden Arbeit ist es, ein tieferes Verständnis induzierter Seismizität zu erreichen. Dazu analysiere ich Seismizität, die während der Stimulationen am Geothermiestandort Soultz-sous-Forêts (Frankreich) induziert worden ist. Die Anlage in Soultz ist seit 1987 europäischer Pilotstandort für EGS. In den mehr als 25 Jahren hat sich ein reicher Erfahrungsschatz entwickelt. Während dieser Zeit wurde ein weltweit einmaliger Datensatz geschaffen, der Soultz zum fortgeschrittensten EGS-Projekt überhaupt macht.

Im Hauptteil der Arbeit beschäftige ich mich mit der Stimulation der Bohrung GPK2 vom Juni und Juli 2000. Damals wurden während der sechstägigen Stimulation  $23\,400\text{ m}^3$  Wasser unter Drücken von bis zu 14,5 MPa verpresst. Dabei konnten durch die Aufzeichnungen des Oberflächen-Seismometer-Netzwerkes 7215 seismische Ereignisse lokalisiert, sowie von 715 Ereignissen mit einer Magnitude  $M > 1$  Herdflächenlösungen bestimmt werden. Dieser von der Université de Strasbourg sowie von der GEIE Heat Mining, Soultz, zur Verfügung gestellte Datensatz ist die Basis der Studien dieser Arbeit.

Die Dissertation wurde im Rahmen des FP7 GEISER (Geothermal Engineering Integrating Mitigation of Induced Seismicity in Reservoirs) Projekt durchgeführt, das von der Europäischen Kommission gefördert wurde. Die Arbeit hat von ertragreichen Kollaborationen mit der Université de Strasbourg, der Geowatt AG, Zürich, dem Helmholtz-Zentrum Potsdam Deutsches GeoForschungsZentrum und der CSIRO Earth Science and Resources Engineering, Perth enorm profitiert.

In der ersten Studie gehe ich der Frage nach, ob die Wechselwirkung der Erdbeben miteinander durch Triggerung einen entscheidenden Einfluss auf die räumlich-zeitliche Ausbreitung der Seismizität hat. Dazu wähle ich einen analytischen Ansatz für das Verschiebungsfeld eines rechteckigen Versatzes im Halbraum und überlagerre dabei mehrere Quellen, um eine realistische Versatzverteilung auf den Bruchflächen berücksichtigen zu können. Aus der Analyse ergibt sich ein scheinbar zufälliges Muster von Spannungsaufbau und Spannungsabbau. Abgesehen von sehr kleinräumigen Bereichen, sind die durch das Verschiebungsfeld hervorgerufenen Spannungen kleiner als  $\pm 1$  MPa. Zudem haben die Herdflächen verschiedene Orientierungen und bilden somit ein volumetrisches Kluftnetzwerk. Es zeigt sich, dass etwa 60 % aller Hypozentren in Bereichen erhöhter Coulomb-Spannung liegen, also zuvor durch Spannungstransfer näher an die Versagensgrenze gebracht wurden. Das Verhalten ändert sich, wenn Beben, die sich auf einer großen Störungszone befinden, betrachtet werden. Hier kann es insbesondere bei geringen Fluideindrücken, z. B. am Rand des stimulierten Bereichs, zu einer sukzessiven Triggerung von Seismizität kommen, bei der angrenzende Bereich der Störungszone erhöhten Spannungen ausgesetzt werden. Das wird am Beispiel einer Sequenz von Beben, die nach Beendigung der Stimulation auf der größten Störungszone des Soultzer Reservoirs aufgetreten sind, demonstriert.

Im Anschluss wird das besondere Verhalten der Seismizität und des hydraulischen Regimes nach Beendigung der Stimulation in der Bohrung GPK2 genauer untersucht. Die Besonderheiten des anomalen Ausbreitungsverhaltens und Hinweise auf einen verstärkten Fluidfluss während der Druckeinschlusssphase geben Anlass, die Herdmechanismen und die Änderungen des Spannungsfeldes zu betrachten. Dabei zeigt sich zunächst eine systematische Änderung der Herdmechanismen, die eine größere Aufschiebungskomponente aufweisen. Das Spannungsfeld wiederum wurde mit zeitlich und räumlich aufgelösten Inversionen der Herdflächenlösungen analysiert. Es ergibt sich eine sehr starke Reduktion der maximalen Horizontalspannung beziehungsweise eine Erhöhung der minimalen Horizontalspannung, was einen Wechsel des Spannungsregimes von einem Zustand zwischen Abschiebungs- und Blattverschiebungsregime zu einem reinen Abschiebungsregime bewirkt. Daraus erklärt sich, dass nahezu ausschließlich Abschiebungsbeben beobachtet wer-

den. Die beobachteten Spannungsänderungen sind mit den coseismischen Spannungsänderungen nicht kompatibel. Diese Diskrepanz wird vermutlich durch aseismische Deformationsprozesse hervorgerufen.

In einer weiteren Studie beschäftigte ich mich etwas näher mit zeitabhängigem Verhalten in Verbindung mit Spannungstransfer. In einem numerischen Modell, basierend auf der Finite-Elemente-Methode, wende ich das Modell der Schädigungsmechanik kombiniert mit einem zeitabhängigen Versagenskriterium auf den Fall von Bohrlochrandausbrüchen an. Das Versagenskriterium basiert auf der experimentellen Beobachtung von Kriechbrüchen, die bei Lasten, die deutlich unter der Kurzzeit-Festigkeit der Gesteinsproben liegen, auftreten. Es zeigt sich, dass Bohrlochrandausbrüche sowohl in der Breite wie auch in der Tiefe mit der Zeit wachsen. Durch sukzessiven Spannungstransfer von geschädigten Elementen auf benachbarte Elemente werden die maximalen Spannungen mit der Zeit reduziert und das Wachstum der Bohrlochrandausbrüche verlangsamt sich. Dies folgt dem Omori-Gesetz, das in der Seismologie zur Charakterisierung des Abklingverhaltens von Nachbeben verwendet wird.



---

## CONTENTS

---

1	INTRODUCTION	1
1.1	Enhanced Geothermal Systems	1
1.2	Induced seismicity	3
1.3	Thesis structure	5
2	FOUNDATIONS OF GEOMECHANICS AND FAULTING	7
2.1	Coupled processes in fractured reservoirs	7
2.2	Stress and strain	11
2.2.1	Stress in two and three dimensions	12
2.2.2	Elastic moduli	14
2.2.3	Role of pore fluid pressure	15
2.3	Failure of rock	16
2.3.1	Stress regimes	18
2.4	Time-dependent behavior	19
2.4.1	Brittle creep	21
2.5	Earthquake sources	24
2.5.1	Source models	24
2.5.2	Fundamental relations in seismology	26
2.5.3	Two empirical relations of earthquake statistics	27
2.6	Back to geomechanics	29
2.6.1	Static stress transfer	29
2.6.2	Inversion of focal mechanism solutions	30
3	SOULTZ-SOUS-FORÊTS PILOT EGS	33
3.1	Field development	33
3.2	Field operation	36
3.3	Results of geophysical analyses	40
4	THE ROLE OF TRIGGERING BY STATIC STRESS TRANSFER DURING GEOTHERMAL RESERVOIR STIMULATION	45
4.1	Introduction	45
4.2	Data description	47
4.3	Method	49
4.4	Partitioning of source zones	51
4.5	$\Delta$ CFS During Stimulation of GPK2	53
4.5.1	Sensitivity to Limiting Magnitude	54
4.5.2	Triggering Potential and Stress Drop	55
4.5.3	Triggering: An Example	58
4.6	Discussion	60
4.7	Conclusions	63

5	THE PECULIAR SHUT-IN BEHAVIOR OF THE WELL GPK2 AT SOULTZ-SOUS-FORÊTS	65
5.1	Introduction	65
5.2	Stimulation of GPK2	66
5.3	Conclusions	70
6	CHANGE OF STRESS REGIME DURING GEOTHERMAL RESERVOIR STIMULATION	73
6.1	Introduction	73
6.2	Observations	74
6.3	Fault plane identification	75
6.4	Stress inversions and results	79
6.5	Conclusions	83
7	TIME-DEPENDENT BRITTLE CREEP AS A MECHANISM FOR TIME-DELAYED WELLBORE FAILURE	85
7.1	Introduction	86
7.2	Time-Dependent Brittle Creep	88
7.3	Numerical Model	89
7.4	Results	92
7.5	Discussion	96
7.6	Conclusions	97
8	CONCLUSIONS	99
8.1	Major findings	100
8.2	Outlook	103
	REFERENCES	120
	DECLARATION OF AUTHORSHIP	121
	ACKNOWLEDGMENTS	125

# 1

---

## INTRODUCTION

---

Geothermal power is envisioned to supply a substantial part of future energy production. The International Energy Agency (IEA) projects, that by 2050 geothermal could contribute about 1400 TWh per year, or 3.5 % of the world total electricity production and 5.8 EJ of heat [IEA, 2011]. Given that in 2012 about 11 224 MW of installed world-wide capacity produced 73.3 TWh [Jennejohn et al., 2012], a lot of research and development has to be done to reach this goal. Major advantages of geothermal power over other forms of renewable energies are the capability to provide base load power, the low environmental impact and CO<sub>2</sub> emissions and the principal availability everywhere on the Earth.

Countries, such as Iceland, El Salvador, Kenya or the Philippines, with a favorable geological environment, can cover already a substantial part of their required electric power from geothermal energy using hydrothermal resources. In less favorable geological environments, such as they are predominant in central Europe, geothermal resources need to be harnessed from deep rocks, which provide much less natural permeability. Here the concept of enhanced geothermal systems (EGS) is the great white hope with huge prospective potential. In their agenda, the IEA sees enhanced geothermal systems as a major pillar of geothermal energy production, with more than half of projected increase of installed capacity being of EGS-type by 2050 (Figure 1.1).

### 1.1 ENHANCED GEOTHERMAL SYSTEMS

Enhanced geothermal systems exploit the heat stored at great depth by forced fluid circulation between two or more boreholes (Figure 1.2). Since the hydraulic conductivity of the pre-existing fracture network is often not sufficient for economically viable operation of a power plant, it is enhanced by different engineering methods. Most important are massive hydraulic stimulations and acidizations. For massive hydraulic stimulations, fluid is induced under high pressures in the order of several MPa, to overcome the shear strength of pre-existing fractures to induce faulting. In this process, the hydraulic conductiv-

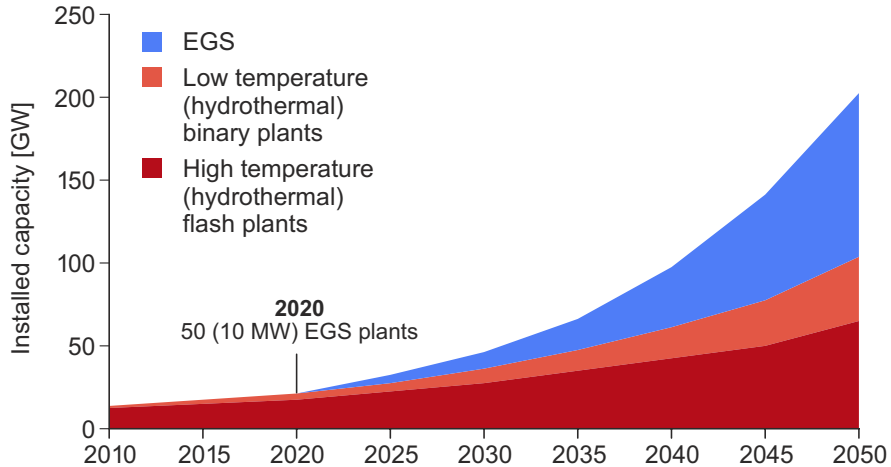


Figure 1.1: Projected growth of geothermal power capacities by technology type [modified from IEA, 2011].

ity increases substantially and production rates in the order of several tens of liter per second per well can be achieved.

Research on enhanced geothermal systems began in the 1970s with the development of the Fenton Hill, New Mexico research project. Two wells were connected by the hydraulic fracturing technique at about 3000 m depth. A flow rate of up to  $141\text{s}^{-1}$  yielded to 10 MW thermal output [Jung, 2013]. The project was eventually abandoned.

In 1987 research around a new European pilot EGS started in Soultz-sous-Forêts, in the French section of the Upper Rhine graben. Today, after 25 years of research and development, the EGS at Soultz is the most advanced site world-wide providing an outstanding data base for research on EGS (Chapter 3). The experiences gained in the course of this project lead to several commercial projects in the geological surroundings of Soultz, such as the projects in Landau, Insheim and Rittershoffen with several more being in the planning phase.

### *Future challenges*

Currently, only very few enhanced geothermal systems are in operation and their net produced power output is relatively low. In order to achieve the goal for EGS in 2050 as envisioned by IEA [2011] several key actions and milestones have to be reached. On the research and development side the following milestones are defined by IEA:

- Development of at least 50 more EGS in next 10 years funded as research & development projects.
- Development of cheaper drilling technologies.
- Development of EGS pilot plants in different geological environments.

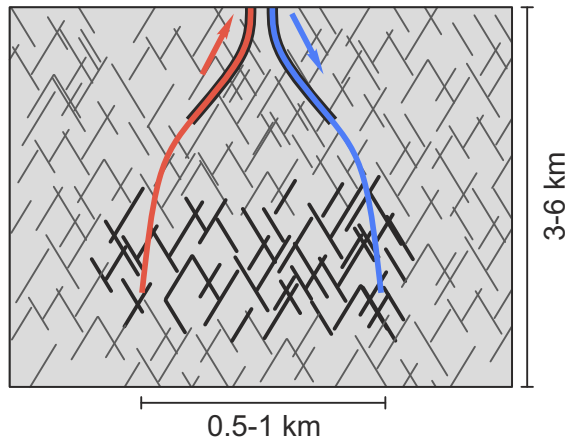


Figure 1.2: Concept of an enhanced geothermal system with engineered fracture network as subsurface heat exchanger in the host rock.

- Improvement of health, safety and environment issues of EGS, which includes the problem of induced seismicity.
- Realization of long-term availability of the resource.
- Upscaling of power plants: in the next decade from 3 to 10 MW<sub>e</sub> and eventually to 200 MW<sub>e</sub> through stacking of EGS modules in series and parallel by 2050.

Currently geothermal power production is competitive where high-temperature hydrothermal resources are available. Cost projections for EGS are difficult to be calculated [IEA, 2011], since current projects are pilot-scale with a large amount of research and development, particularly in the drilling and the stimulation phases of the projects. Cost reductions can be achieved by improved drilling techniques but also by improved understanding of the geological formations drilled through. Problems of wellbore stability that arose during the drilling of several geothermal wells in the Upper Rhine graben, have caused substantial additional cost, which endangered the whole project. Furthermore, the exploration risk lead to abandonment of several projects and substantial loss of investments. When geothermal resources at a site or region is developed by many wells, drilling pilot wells with a large research component might be economically advisable [Stjern et al., 2003].

## 1.2 INDUCED SEISMICITY

The connection between injection of fluids and the occurrence of seismicity was first made by Healy et al. [1968], who related the waste water injection at the Rocky Mountain Arsenal with the unusual series of earthquakes of up to magnitude 5.5 near Denver, Colorado. They related it to the reduction of friction through elevated pore fluid pres-

sure as proposed by Hubbert and Rubey [1959]. Diffusion of pore fluid pressure was proposed as responsible for delayed occurrence of aftershock activity [Nur and Booker, 1972]. Furthermore, earthquakes occurred many times after impoundment of water reservoirs, several of them causing large damage and even fatalities [Simpson, 1976]. Some observations of reservoir impoundment seismicity revealed a clear migration of seismicity, interpreted as diffusion of pore fluid pressure, triggering the seismicity [Talwani and Acree, 1984]. More recently it became more and more accepted that deep fluid flow in the Earth's crust is the mechanism for many natural sequences of seismicity, e.g. the Vogtland swarm earthquakes [Hainzl, 2004]. With the advent of exploitation of unconventional hydrocarbons, where large amounts of waste-water need to be disposed off by deep injection, induced seismicity became a hot topic, both in the scientific community and in the public [Ellsworth, 2013]. Likewise, induced seismicity in connection with geothermal power production and CO<sub>2</sub> sequestration has aroused public awareness and the urgent need for better understanding of the processes involved for future mitigation of seismicity [Evans et al., 2012].

In the process of engineering the natural fracture network to create an EGS, seismicity is deliberately induced and routinely monitored. During the stimulation treatments of the Soultz reservoirs about 100 000 events have been recorded. The maximum magnitudes reached  $M_w = 2.9$  with many events above magnitude 2. While no confirmed damage was caused by these events, the shaking caused public awareness and fear of larger events and lead to some opposition against the project. During the stimulation conducted for the Basel Deep Heat Mining project an event of local magnitude  $M_L = 3.4$  was induced which lead to the temporary stop of the project [Häring et al., 2008]. After a comprehensive risk analysis, which took into account geological and economical considerations [Baisch et al., 2009], the project was eventually abandoned. Seismicity induced by the geothermal power plant in Landau, Germany [Bönnemann et al., 2010] lead to the temporary halt of the power plant. Later, production continued but under further conditions imposed by the authorities. Therefore induced seismicity is perceived as a potential show stopper of the EGS technology or at least imposes large barriers for future large scale operation of EGS plants [Majer et al., 2007; Evans et al., 2012].

These barriers are addressed by several large research projects, that focus on the understanding and mitigation of induced seismicity. The GEISER Project [2013] was conducted on a European level between 2010 and 2013. It consisted of work packages on data analysis, modelling, hazard analysis, mitigation strategies. The outcome of the project should help authorities in the licensing procedures for new projects. Part of this thesis was conducted within the framework of this project. Since seismicity has occurred in several geother-

mal plants producing in Germany jeopardizing public acceptance of geothermal energy, the German project MAGS – »Mikroseismische Aktivität geothermischer Systeme« was initiated to develop better monitoring and mitigation strategies.

### 1.3 THESIS STRUCTURE

This thesis is a »cumulative« dissertation, comprised of four individual studies on time-dependency of stress and seismicity in geothermal reservoirs and wellbores. Three studies are published in or submitted to international journals, one study appeared in a conference proceedings. The studies are ordered such, that a closed image of the processes can be drawn.

Facing the challenge of induced seismicity as one major obstacle for future application of enhanced geothermal systems, the main goals of this thesis are an increased understanding of the physical processes relevant for induced seismicity. The main questions to answer in this thesis are: (1) In which manner are concepts successful in describing the processes of natural earthquake sequences applicable to induced seismicity? (2) How do the stress perturbations caused by forced fluid flow relate to the seismic response of the reservoir? And (3) Since the stress perturbation by fluid injection is time-dependent in magnitude and spatial extend; how do time-dependent processes affect induced seismicity?

To answer these questions, different approaches are taken. They base on analysis of data measured at the EGS at Soultz-sous-Forêts, specifically of catalogs of locations, magnitudes and focal mechanism solutions of induced earthquakes. These and other data of the EGS were used to model stress changes in the reservoir by semi-analytical and numerical methods. Additionally, stress changes were also derived by an inversion technique.

In Chapter 2 the basic geomechanical and seismological background for the individual studies is established. Since I used diverse data from the outstanding dataset of the EGS at Soultz-sous-Forêts extensively during the work on this thesis, a brief overview of the activities and results of 25 years of research at this site are given in Chapter 3. Then, the studies are presented in separate chapters, as outlined below.

#### *Static stress transfer*

In the first study (Chapter 4) the contribution of static stress transfer caused by co-seismic dislocations to the total stress perturbation arising during a geothermal reservoir stimulation of well GPK2 at Soultz was analyzed. The role of triggering of seismicity by static stress transfer was quantified. This model is very successful in explain-

ing mainshock-aftershock sequences. However, the relevance of inter-event triggering during massive hydraulic stimulation was unknown before. The major outcome of this study is that during the injection phase the contribution of inter-event triggering is small since seismicity develops in a dense fracture network and displacement induced stress changes are both, positive and negative, in adjacent parts of the reservoir. Therefore no systematic triggering is observed. During the post-injection phase however, the pattern of seismicity evolution changes. Then, seismicity is confined to large scale faults. On these faults the contribution of stress transfer to the total stress perturbation is quite significant and the triggering is much more effective.

#### *GPK2 shut-in and stress field*

Subsequently, the changing behavior of seismicity during the post-injection period of the stimulation of well GPK2 is analyzed in further detail. The short study presented in Chapter 5 focuses on the spatial evolution of seismicity following shut-in. While the seismicity cloud was stationary during stimulation, it starts to migrate in a preferred direction after injection ceased. The results gave rise to the next study (Chapter 6), where the hypothesis, if stress changes arising in the course of the stimulation are causing the observed changes of the seismicity pattern is tested. In this study the same data set of focal mechanism solutions as before was used to invert for the stress field and in particular its changes in space and time in the course of the stimulation and the post-injection period. A strong reduction of the intermediate principal stress is observed, which leads to a change of the stress regime with implications for the faulting mechanisms observed.

#### *Time-dependent breakout development*

In the study presented in Chapter 7 I leave the reservoir scale to analyze effects of time-dependency and stress transfer on the simpler case of a wellbore. Specifically in this study, I analyze the time-dependent development of borehole breakouts, as it has been observed before in many wells and in different lithologies. In this numerical analysis, I apply the mechanism of time-dependent brittle creep to the stress field at a wellbore using a damage mechanics approach. This leads to a time-dependent growth of breakouts. The trend of the wellbore to reach a stable regime can be described by the same relation, that is used to describe the activity of aftershocks following a main shock, namely Omori's law.

# 2

---

## FOUNDATIONS OF GEOMECHANICS AND FAULTING

---

In the following chapter, basic concepts of continuum mechanics with application to geomechanics and seismology are introduced. Since aspects from a broad field from geomechanics to seismology are covered in this thesis, only concise outlines can be drawn. The introduction of geomechanical aspects follows the monographs of Jaeger et al. [2007]; Fjaer et al. [2008]; Scholz [2002]; Segall [2010]; Zang and Stephansson [2010] and Zoback [2010]. Seismological foundations are covered based on the books of Lay and Wallace [1995]; Scholz [2002]; Shearer [2009] and the review paper of Kanamori and Brodsky [2004].

In the following section I give a brief overview of the principal coupled mechanisms relevant for the case of cold water injection in a fracture rock mass and their respective role in the engineering process for geothermal systems. Then, the fundamentals of geomechanics, elasticity and failure are covered in more detail quantitatively, with a side-step to time-dependent behavior. This is followed by a brief description of some seismological concepts, which are then exploited by more advanced techniques to obtain insights on the geomechanical processes and the state of stress in geo-reservoirs, which are the focus of this thesis.

### 2.1 COUPLED PROCESSES IN FRACTURED RESERVOIRS

In geothermal fields, fault systems are the main targets for drilling, hydraulic stimulation and circulation of water since they are expected to yield high production rates that are needed for economical operation of the power plant [Held et al., 2014]. Geothermal reservoirs are thus composed of fractures embedded in the rock matrix, both of which contain geothermal brine. This system of rock matrix, fractures and fluids hosts a large number of coupled processes with influence on the geomechanical state of the reservoir.

Fluid flow is governed by the principle of mass balance and the continuity equation. In highly fractured geothermal reservoirs, fluid flow is dominated by flow in faults and fractures rather than by flow in the rock matrix. This is fundamentally different from porous reservoirs usually exploited for oil and gas and underground storage fa-

cilities and hydrothermal systems. In such porous reservoirs, faults are mostly acting to seal and confine the reservoir. As a consequence, many processes dominant in porous reservoirs are negligible in fractured reservoirs and vice versa. Flow in a porous rock matrix is described by Darcy's law [Darcy, 1856]:

$$\mathbf{v} = -K \cdot \nabla p, \quad (2.1)$$

where  $v$  is the Darcy velocity,  $K$  the hydraulic conductivity and  $\nabla p$  the pressure gradient. Darcy's law can be derived from the Navier-Stokes equations and describes the diffusional process. In a fractured medium the flow rate  $Q$  can be expressed with:

$$Q = a \cdot \frac{k}{\mu} \cdot \nabla p, \quad (2.2)$$

where  $a$  is the fracture aperture,  $k$  the permeability and  $\mu$  the dynamic viscosity. Permeability  $k$  can be related to:

$$k \approx \frac{a^2}{12}, \quad (2.3)$$

resulting in the cubic law with  $Q \propto a^3$  [Snow, 1965]. It represents the common approximation of fluid flow in fractures as flow between parallel plates. The hydraulic field in a fractured medium is thus strongly dependent on the fracture aperture. When pressurizing a fracture, its aperture changes by an elastic response, leading to an increase in fracture aperture and, consequently, permeability. Different models can be used to describe the increase of fracture aperture by elastic response and shearing. The most commonly used are those described by Barton et al. [1985] and Willis-Richards et al. [1996]. For granite, they are experimentally compared by Chen et al. [2000]. They find them to generally perform equally well with regard to the tested rock samples and no clear preference could be given to either of these models.

Due to the elastic response of fractures to pressure, the hydraulic response of a reservoir is characterized by a rapid increase in pressure also relatively far from the injection source, as seen e.g. in the stimulation of well GPK<sub>3</sub> at Soultz, where pressure could be monitored also in well GPK<sub>2</sub>, 600 m away from the injection point (Figure 2.1). Another feature is an equilibrium pressure that develops between constant injection rate and permeability creation. Increases of injection rate are followed only by small increases of pressure, as the previous pressurization created additional permeability by elastic opening of the fractures. All these features of flow in a fractured reservoir have been observed in a large number of well stimulations, indicating the dominance of fracture flow [Baisch and Harjes, 2003; Häring et al., 2008, and Figure 2.1]. To demonstrate these effects, Figure 2.2 shows typical pressures response of a reservoir under stimulation,

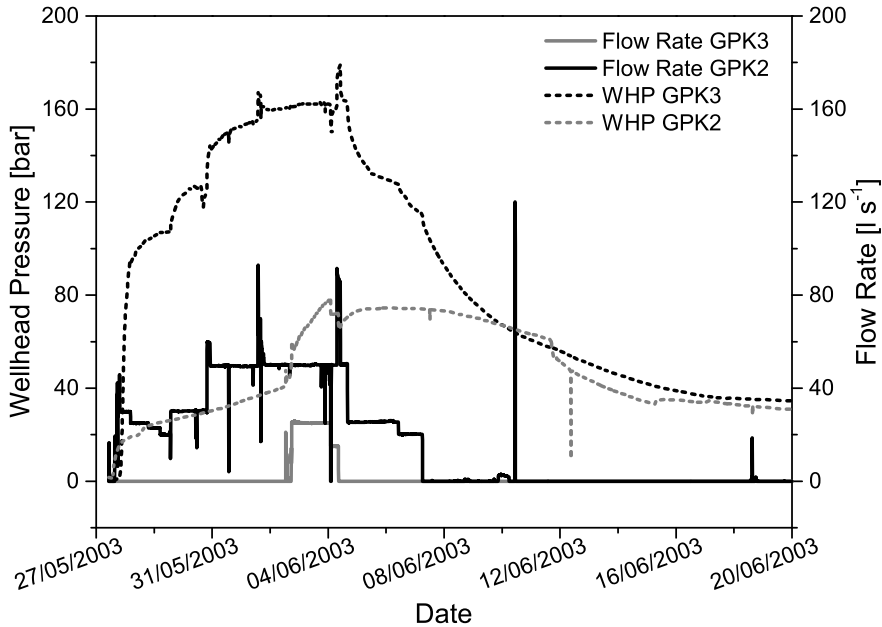


Figure 2.1: Injection flow rates and wellhead pressures (WHP) of the stimulation treatment of wells GPK<sub>3</sub> and GPK<sub>2</sub> in May/June 2003. Note the quick pressure rise in GPK<sub>2</sub> after commencement of injection in GPK<sub>3</sub> and the relatively small pressure increase after strong increases of injection rate.

away from the injection well, modeled with (a) a poroelastic model in a homogeneous effective medium with diffusional spreading of the pressure perturbation [Rudnicki, 1986] and with (b) a fracture mechanical model considering the interaction between the pore pressure and the hydraulic properties of the fractures [Kohl and Mégel, 2007]. In nature, fractures have a rough, heterogeneous aperture which reduces flow compared to a smooth surface and thus decreases the effective hydraulic fracture aperture [Witherspoon et al., 1980]. If rough fractures are subject to shear, anisotropy of hydraulic conductivity is introduced [Auradou et al., 2005; Schoenball et al., 2013].

In addition to fluid transport, heat transport occurs in the presence of temperature gradients, and is driven by three mechanisms: advection, conduction, and radiation, the latter being of no relevance in geo-reservoirs. Advective heat flow is coupled to mass transfer of fluids and thus dominant in rock fractures that serve as a heat exchanger. Conductive heat flow, governed by Fourier's law, is the ruling mechanism in an impermeable rock matrix. In the course of temperature changes of the rock and the fluid, they expand or contract under temperature increases or decreases, respectively, causing thermal stresses. As the coefficient of volumetric expansion of water is typically five times larger than that of rock, changes in pore pressure are strongly dependent on the rock permeability [Gens et al., 2007]. Furthermore, several material parameters of the brine and the rock are dependent

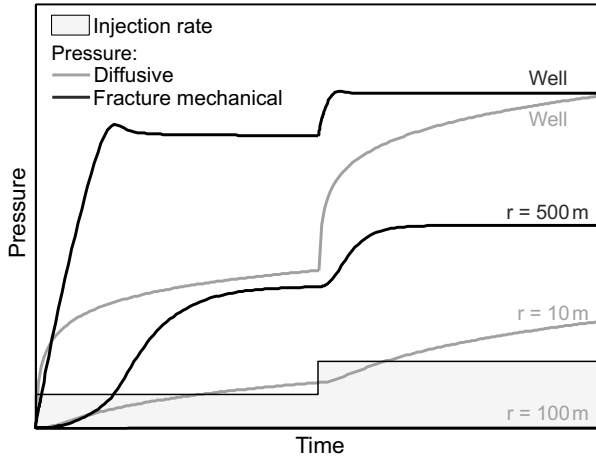


Figure 2.2: Typical fluid pressure responses at distances from the injection source (well) as obtained from fluid flow confined to fractures [HEX-S numerical model by Kohl and Mégel, 2007] (black lines) compared to fluid flow in a 3D matrix after poroelastic solutions by Rudnicki [1986] (gray lines).

on temperature. Notable is the fluid viscosity, varying by an order of magnitude between  $20\text{ }^{\circ}\text{C}$  and  $100\text{ }^{\circ}\text{C}$  [Ershaghi et al., 1983].

Geomechanics is governed by force equilibrium and constitutive equations for the different materials. Examples include Hooke's law for a rock matrix with elastic behavior (Section 2.2.2), or other laws for more complex rock behavior like poroelasticity, plasticity, and creep [Jaeger et al., 2007; Fjaer et al., 2008]. Constitutive equations relate displacement and strain to stress. The total stress is intrinsically tied to the pore fluid pressure to form effective stress (Section 2.2.3), which is relevant for failure criteria (Section 2.3). Increasing or decreasing the fluid content in a continuous porous rock matrix will increase or decrease the pore fluid pressure, but also tends to expand the volume of the rock matrix, including the pore space, inducing additional stresses. These additional pressures and stresses are distributed over time by diffusion, depending on the permeability and the poroelastic stiffness properties of the porous matrix and its constituents. These processes are described by the theory of poroelasticity [Biot, 1941, 1962; Rice and Cleary, 1976; Wang, 2000], in which the pore fluid pressure and the stress field are coupled. An analogous coupling exists between the temperature and the stress field [Zimmerman, 2000], it is described by the theory of thermoelasticity [Nowacki, 1986]. To handle both, they have to be unified to form the theory of thermo-poroelasticity. Analytical solutions exist for a few special cases [Kurashige, 1989; McTigue, 1986; Palciauskas and Domenico, 1982; Wang and Papamichos, 1994]. For complex problems however, numerical tools have to be used. These tools either solve the complex system of fully coupled differential equations [e.g.

Ghassemi et al., 2007; Koh et al., 2011; Simulia Inc., 2012] or rely on a solution scheme that couples sequentially [Rutqvist, 2011].

Besides the thermo-poroelastic coupling between fluid flow, heat transfer, and stress in porous rocks, several other coupling mechanisms exist in fractured reservoirs. Tsang [1991] and Rutqvist and Stephansson [2003] give comprehensive reviews of them. The most important mechanisms relevant for geothermal applications are summarized below.

Massive hydraulic stimulation, production and injection of water under operation conditions cause a massive perturbation of pore fluid pressure and temperature. Both pore fluid pressure increase and temperature decrease through injection of cold water can result in rock failure through a lowering of the effective stresses (Section 2.3). A temperature decrease diminishes the total stress and the associated effective stress by the thermo-elastic effect.

Before a fracture comes to a critical state of stress that induces shearing, the increased pore fluid pressure increases the fracture aperture elastically [Jaeger et al., 2007]. Through the increasing fracture aperture by elastic opening, the available space for the fluid and the hydraulic conductivity increase considerably (see Equation 2.3), which in turn reduces pore fluid pressure build-up. If, however, pore fluid pressure increases further and a failure criterion is met, shearing occurs that is accompanied by further increases of fracture aperture through dilation.

Following shearing in a rupture, stresses are redistributed around the fracture plane. Close to the fracture tips, stresses are built-up while along the perimeters stresses are released (Section 2.6.1).

## 2.2 STRESS AND STRAIN

Crustal tectonic stresses are the result of forces and strains acting on the Earth's crust. They are of dimension force per area, i.e. pressure and act parallel or perpendicular to internal and external planes of a rock volume. Stress is an expression of force  $\vec{F}$  applied to a surface of area  $A$ . At a point the stress vector  $\vec{T}$  is defined as:

$$\vec{T} = \lim_{\Delta A \rightarrow 0} \frac{\Delta \vec{F}}{\Delta A}. \quad (2.4)$$

To every side of an elementary volume, stresses can act in three directions of space. The stress tensor  $\sigma$  is comprised of the three stress vectors acting on a volume. Thus, the stress tensor consists of 9 components  $\sigma_{ij}$  with  $i, j = 1, 2, 3$ . The first index denotes the direction of the plane normal, the second denotes the direction in which the stress is acting (Figure 2.3). Normal stresses, acting in direction of the plane normal, are denoted with  $\sigma_{ii}$ , these are the diagonal elements of the stress tensor. All other components are called shear stresses and are denoted by  $\tau_{ij}$ . Due to conservation of angular momentum the stress

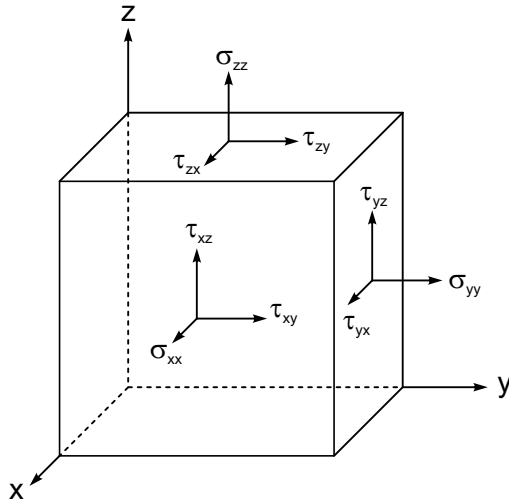


Figure 2.3: Stress tensor components acting on an elementary volume.

tensor needs to be symmetric and the number of independent components reduces to 6. Thus, the stress tensor is

$$\sigma = \begin{pmatrix} \sigma_{xx} & \tau_{xy} & \tau_{xz} \\ \tau_{xy} & \sigma_{yy} & \tau_{yz} \\ \tau_{xz} & \tau_{yz} & \sigma_{zz} \end{pmatrix}. \quad (2.5)$$

The stress tensor  $\sigma$  can be transformed to take a diagonal form through calculation of the eigenvalues, which represent the principal stresses  $\sigma_1, \sigma_2$  and  $\sigma_3$ :

$$\sigma = \begin{pmatrix} \sigma_1 & 0 & 0 \\ 0 & \sigma_2 & 0 \\ 0 & 0 & \sigma_3 \end{pmatrix}. \quad (2.6)$$

The eigenvectors then yield the orientation of the stress tensor in the former  $(x, y, z)$  coordinate system. Typically, the principal stresses are in descending order:

$$\sigma_1 \geq \sigma_2 \geq \sigma_3. \quad (2.7)$$

$\sigma_1$  is thus commonly called the maximum principal stress and  $\sigma_3$  the minimum principal stress. This is as defined in rock mechanics, where  $\sigma > 0$  means compression and  $\sigma < 0$  means tension.

### 2.2.1 Stress in two and three dimensions

To assess if a fault plane is prone to failure, we need to consider the normal and shear stresses acting on that fault plane. In Figure 2.4, a fault plane at an angle  $\theta$  from the direction of  $\sigma_{xx}$  is sketched. Using

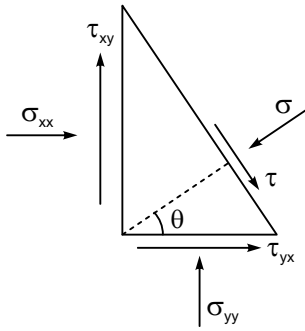


Figure 2.4: Orientation of a failure plane at an angle  $\theta$  with respect to  $\sigma_{xx}$ , with normal stress  $\sigma$  and shear stress  $\tau$ .

trigonometry, the normal stress  $\sigma$  and the shear stress  $\tau$  acting on the plane is obtained:

$$\sigma = \sigma_{xx} \cos^2 \theta + \sigma_{yy} \sin^2 \theta + 2\tau_{xy} \sin \theta \cos \theta \quad (2.8)$$

$$= \frac{1}{2}(\sigma_{xx} + \sigma_{yy}) + \frac{1}{2}(\sigma_{xx} - \sigma_{yy}) \cos 2\theta + \tau_{xy} \sin 2\theta \quad (2.9)$$

$$\begin{aligned} \tau &= \sigma_{yy} \sin \theta \cos \theta - \sigma_{xx} \cos \theta \sin \theta + \tau_{xy} \cos^2 \theta \\ &\quad - \tau_{yx} \sin^2 \theta \end{aligned} \quad (2.10)$$

$$= \frac{1}{2}(\sigma_{yy} - \sigma_{xx}) \sin 2\theta + \tau_{xy} \cos 2\theta \quad (2.11)$$

From these equations, we see that  $\tau$  vanishes when

$$\tan 2\theta = \frac{2\tau_{xy}}{\sigma_{xx} - \sigma_{yy}}. \quad (2.12)$$

The two solutions  $\theta_1$  and  $\theta_2$  of Equation 2.12 yield the directions with no shear stresses on the fault plane, i.e. the principal stresses:

$$\sigma_1 = \frac{1}{2}(\sigma_{xx} + \sigma_{yy}) + \sqrt{\tau_{xy}^2 + \frac{1}{4}(\sigma_{xx} - \sigma_{yy})^2}, \quad (2.13)$$

$$\sigma_2 = \frac{1}{2}(\sigma_{xx} + \sigma_{yy}) - \sqrt{\tau_{xy}^2 + \frac{1}{4}(\sigma_{xx} - \sigma_{yy})^2}. \quad (2.14)$$

In a coordinate system made up by principal stresses with x-axis in direction of  $\sigma_1$ , the stresses  $\sigma$  and  $\tau$  become:

$$\sigma = \frac{1}{2}(\sigma_1 + \sigma_2) + \frac{1}{2}(\sigma_1 - \sigma_2) \cos 2\theta, \quad (2.15)$$

$$\tau = -\frac{1}{2}(\sigma_1 - \sigma_2) \sin \theta. \quad (2.16)$$

These relations can be plotted in a  $\tau$ - $\sigma$ -diagram and we obtain the Mohr circle [Mohr, 1914], which is a graphic representation in 2D of the normal and the shear stresses acting on any plane at an angle  $\theta$  to the maximum principal stress (Figure 2.5a). Going to 3D, we can either use the nine direction cosines, representing the rotations to go

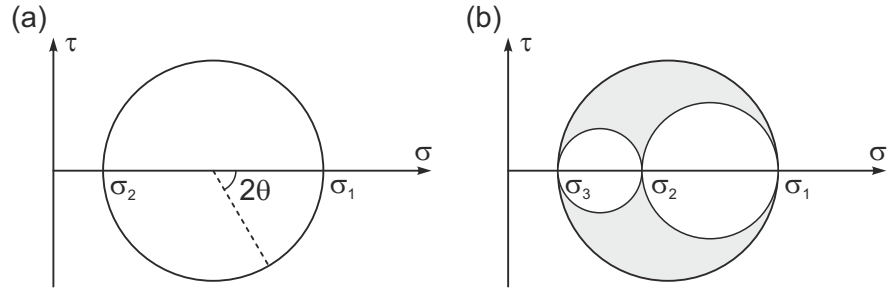


Figure 2.5: (a) Mohr circle for failure planes with angle  $\beta$  to the maximum principal stress  $\sigma_1$  in a 2D stress field. (b) Mohr circles in a 3D stress field. The stress state of any plane lies within the shaded area (after Fjaer et al. [2008]).

from one coordinate system to the other or the three Euler angles to transform stresses from one coordinate system to another and hence to identify principal stress directions in space [Fjaer et al., 2008].

As we have seen, stresses are dependent on the reference system. It is therefore helpful to derive expressions of stress that are independent on the coordinate system in use, so-called stress invariants. Three basic invariants are:

$$I_1 = \sigma_{xx} + \sigma_{yy} + \sigma_{zz} \quad (2.17)$$

$$I_2 = -(\sigma_{xx}\sigma_{yy} + \sigma_{yy}\sigma_{zz} + \sigma_{zz}\sigma_{xx}) + \tau_{xy}^2 + \tau_{yz}^2 + \tau_{xz}^2 \quad (2.18)$$

$$I_3 = \sigma_{xx}\sigma_{yy}\sigma_{zz} + 2\tau_{xy}\tau_{yz}\tau_{xz} - \sigma_{xx}\tau_{yz}^2 - \sigma_{yy}\tau_{xz}^2 - \sigma_{zz}\tau_{xy}^2 \quad (2.19)$$

Any combination of stress invariants is of course also an invariant of stress. One more, very useful invariant is the von Mises stress:

$$q = \sqrt{\frac{3}{2} \left( (\sigma_1 - \bar{\sigma})^2 + (\sigma_2 - \bar{\sigma})^2 + (\sigma_3 - \bar{\sigma})^2 \right)}, \quad (2.20)$$

where  $\bar{\sigma} = I_1/3$ , the mean normal stress.

### 2.2.2 Elastic moduli

Upon failure, slippage occurs on a plane, resulting in a displacement field  $\vec{u}$ . The strain tensor  $\epsilon$  is obtained through

$$\epsilon_{ij} = \frac{1}{2} \left( \frac{\partial u_i}{\partial x_j} + \frac{\partial u_j}{\partial x_i} \right). \quad (2.21)$$

In a linear elastic material, the stress tensor is related to the strain tensor  $\epsilon$  by the generalized Hooke's law

$$\sigma_{ij} = C_{ijkl} \epsilon_{kl}, \quad (2.22)$$

where  $C_{ijkl}$  is the symmetric fourth-rank stiffness tensor. Since the strain and stress tensors are symmetric,  $C_{ijkl}$  must be symmetric in

$(k, l)$  and  $(i, j)$ , respectively. Furthermore, the strain energy function requires  $C_{ijkl} = C_{klji}$  [Segall, 2010]. For an isotropic medium, the most general form following these symmetries is

$$C_{ijkl} = \lambda \delta_{ij} \delta_{kl} + G(\delta_{ik} \delta_{jl} + \delta_{il} \delta_{jk}). \quad (2.23)$$

This yields the isotropic form of Hooke's law

$$\sigma_{ij} = 2G\epsilon_{ij} + \lambda\epsilon_{kk}\delta_{ij}, \quad (2.24)$$

with the elastic moduli  $\lambda$  and  $G$ , known as Lamé parameters.  $G$  is also commonly known as the shear modulus. The bulk modulus  $K$  of a volume  $V$  is obtained from

$$K = -V \frac{dP}{dV} = \lambda + \frac{2}{3}G. \quad (2.25)$$

Finally, Young's modulus  $E$  and Poisson's ratio  $\nu$  are found from

$$E = G \frac{3\lambda + 2G}{\lambda + G} \quad (2.26)$$

$$\nu = \frac{\lambda}{2(\lambda + G)}. \quad (2.27)$$

Thus, any two of the moduli  $(\lambda, G, K, E, \nu)$  represent a full set of elastic parameters. Table 2.1 gives an overview of the conversion formulae between elastic parameters.

### 2.2.3 Role of pore fluid pressure

The previous description of rock mechanics neglects the fact that rocks are porous. The pores of subsurface rocks are typically saturated with fluids which can be water, hydrocarbons and also rock melt for very deep rocks. Terzaghi [1936] has proposed that the pore fluid pressure  $p$  plays an important role in the fracturing of rock. He argued that the pore fluid pressure counteracts the applied stress and acts as a kind of tensile stress on the pores and hence introduced the effective stress

$$\sigma_{i,\text{eff}} = \sigma_{i,\text{tot}} - p, \quad (2.28)$$

which should be used when considering a failure criterion (Section 2.3).

Under hydrostatic conditions, i.e. the pore space of the overburden is interconnected, pore pressure is obtained from integrating fluid density in the column above the point of interest at depth  $D$ :

$$p = \int_0^D \rho_w(z)g dz \approx \rho_w g D. \quad (2.29)$$

	E	$\nu$	G	K	$\lambda$
(E, $\nu$ )	E	$\nu$	$\frac{E}{2(1+\nu)}$	$\frac{E}{3(1-2\nu)}$	$\frac{E\nu}{(1+\nu)(1-2\nu)}$
(E, G)	E	$\frac{E-2G}{2G}$	G	$\frac{EG}{3(3G-E)}$	$\frac{G(E-2G)}{3G-E}$
(E, K)	E	$\frac{3K-E}{6K}$	$\frac{3KE}{9K-E}$	K	$\frac{3K(3K-E)}{9K-E}$
( $\nu$ , G)	$2G(1+\nu)$	$\nu$	G	$G \frac{2(1+\nu)}{3(1-2\nu)}$	$G \frac{2\nu}{1-2\nu}$
( $\nu$ , K)	$3K(1-2\nu)$	$\nu$	$3K \frac{1-2\nu}{2+2\nu}$	K	$3K \frac{\nu}{1+\nu}$
( $\nu$ , $\lambda$ )	$\lambda \frac{(1+\nu)(1-\nu)}{\nu}$	$\nu$	$\lambda \frac{1-2\nu}{2\nu}$	$\lambda \frac{1+\nu}{3\nu}$	$\lambda$
(G, K)	$\frac{9KG}{3K+G}$	$\frac{3K-2G}{6K+2G}$	G	K	$\frac{3K-2G}{3}$
(G, $\lambda$ )	$\frac{G(3\lambda+2G)}{\lambda+G}$	$\frac{\lambda}{2(\lambda+G)}$	G	$\frac{3\lambda+2G}{3}$	$\lambda$
(K, $\lambda$ )	$9K \frac{K-\lambda}{3K-\lambda}$	$\frac{\lambda}{3K-\lambda}$	$3 \frac{K-\lambda}{2}$	K	$\lambda$

Table 2.1: Formulas for conversion of two elastic parameters to the remaining ones [from Zoback, 2010].

### 2.3 FAILURE OF ROCK

In a stressed crust with pre-existing fractures, the state of stress can be considered to be in a frictional faulting equilibrium [Sibson, 1974; Townend and Zoback, 2000]. Shear failure is caused if shear stresses are high enough. In frictional faulting equilibrium shear stresses  $\tau$  parallel to the fracture are balanced by frictional forces acting through stresses normal to fractures  $\sigma$  and stabilizing the rock. Failure occurs if a certain threshold  $f(\sigma)$  of shear stress is exceeded [Mohr, 1914]:

$$|\tau| = f(\sigma). \quad (2.30)$$

This relation divides stable from unstable conditions. A simple and widely used failure criterion is that of Coulomb [1773]. It is based on two assumptions. First, fracture occurs on a plane which is assumed

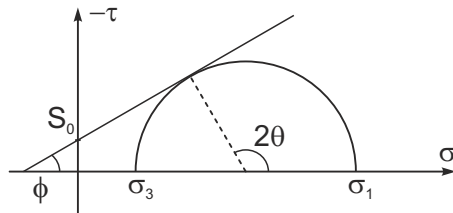


Figure 2.6: Mohr diagram with failure curve of Equation 2.31 [after Jaeger et al., 2007].

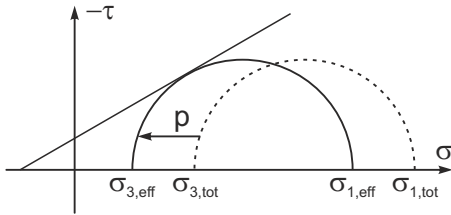


Figure 2.7: Mohr-Coulomb criterion with effect of pore pressure on total stresses  $\sigma_{i,tot}$  and the Coulomb failure criterion.

to resist through a frictional force created by the normal stresses multiplied by a coefficient of friction. Second, the rock has some strength even in the absence of any normal stresses. This strength is represented by a cohesion coefficient  $S_0$ . Failure occurs if the shear stresses are larger than the cohesion plus the frictional strength:

$$|\tau| \geq S_0 + \mu\sigma. \quad (2.31)$$

The parameter  $\mu$  is known as the coefficient of internal friction. In laboratory experiments on crustal rocks and below normal stresses exceeding 200 MPa, the friction coefficient  $\mu$  typically takes values in the order of 0.85, which is known as Byerlee's law [Byerlee, 1978]. For clayey formations  $\mu$  can take much smaller values of 0.2 and even below [Tembe et al., 2009], leading to very weak fault zones that deform by creep rather than seismically. Figure 2.6 shows a graphical representation of Coulomb failure criterion along with the Mohr circle. The Mohr circle touches the failure line for a plane at an angle  $2\theta$  with the  $\sigma_1$  direction. Then

$$|\tau| = \frac{1}{2}(\sigma_1 - \sigma_3) \sin \theta, \quad (2.32)$$

$$\sigma = \frac{1}{2}(\sigma_1 + \sigma_3) + \frac{1}{2}(\sigma_1 - \sigma_3) \cos \theta, \quad (2.33)$$

and the angle  $\theta$  of a fault plane which is optimally oriented for failure and the friction angle  $\phi = \arctan \mu$  are related by:

$$\theta = \frac{\pi}{4} + \frac{\phi}{2}. \quad (2.34)$$

If we consider the Coulomb criterion with the effective stress concept, we find that the Mohr circle approaches the failure envelope to the right and the rock mass is in a more critical state at an elevated pore fluid pressure compared to the total stresses. A stress state not critical before considering pore fluid pressure may be overcritical and failure occurs if the Mohr circle touches the failure curve (Figure 2.7).

Due to its simplicity, the Mohr-Coulomb criterion is the most-widely used failure criterion in rock mechanics. One major drawback is the neglect of the intermediate principal stress  $\sigma_2$  on the strength of rock (c.f. Figure 2.5b). Several other failure criteria, some of them include the intermediate stress, are presented and discussed in Zoback [2010].

### 2.3.1 Stress regimes

It is generally assumed that the vertical stress is a principal stress. This is often a good approximation, but might not be valid in areas of strong topography changes and is certainly not the case when viscous processes play a role, such as in salt tectonics [Zoback, 2010]. However, if this approximation can be made, the vertical stress  $\sigma_v$  at depth D is given by the weight of the overburden:

$$\sigma_v = \int_0^D \rho(z)g dz, \quad (2.35)$$

with the depth-dependent density of the rock formation  $\rho(z)$ . The other principal stresses are the maximum and minimum horizontal stresses,  $\sigma_H$  and  $\sigma_h$ . Their magnitudes are determined by the tectonic setting and constraint by faulting as outlined in the following.

Based on earthquake mechanisms and many structural geological indicators (Figure 2.8) slippage of rock is generally grouped in three principal styles of faulting. Anderson [1951] identified tectonic stresses as responsible for observations of different faulting style. He defined the three principal stress regimes according to the relative magnitudes of the principal stresses:

Normal faulting  $\sigma_v \geq \sigma_H \geq \sigma_h$ ,

Strike slip faulting  $\sigma_H \geq \sigma_v \geq \sigma_h$ ,

Thrust faulting  $\sigma_H \geq \sigma_h \geq \sigma_v$ .

Faulting restricts possible stress states for each faulting type even further. Combined with the Mohr-Coulomb faulting theory in geomechanics, the stress state for each faulting type can be further bounded, and a stress polygon of allowed stress states can be drawn [Zoback, 2010]. A stress state is allowed, if no faulting occurs, that is, if the

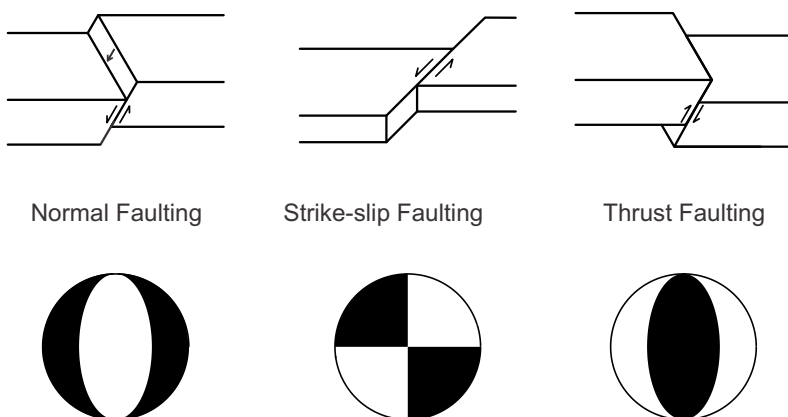


Figure 2.8: Andersonian stress regimes and corresponding focal mechanisms [after Lay and Wallace, 1995].

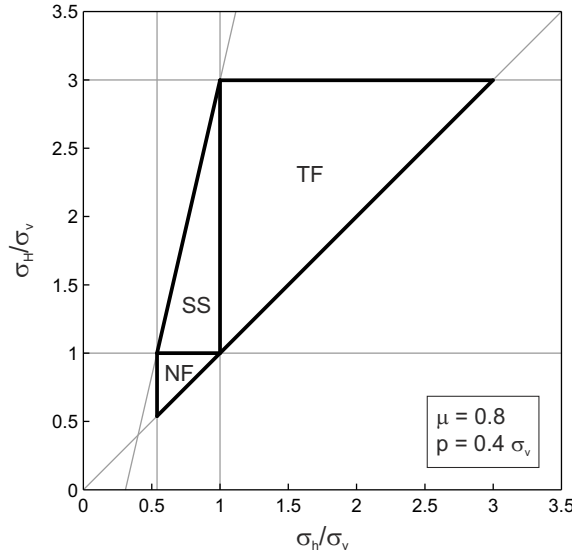


Figure 2.9: Stress polygon of allowed stress states following Mohr-Coulomb faulting theory with  $\mu = 0.8$ , after Zoback [2010]. Andersonian faulting regimes are bound by triangles in  $\sigma_H$ - $\sigma_h$ -space. NF is normal faulting, SS is strike-slip faulting, TF is thrust faulting.

point of observation is in mechanical equilibrium. Then, the following inequalities (plus the trivial condition  $\sigma_H \geq \sigma_h$ ), bounding the stress polygon (Figure 2.9), are full-filled:

$$\sigma_h \geq \frac{\sigma_v - p}{(\sqrt{\mu^2 + 1} + \mu)^2} + p \quad (2.36)$$

$$\sigma_H \leq (\sqrt{\mu^2 + 1} + \mu)^2 (\sigma_v - p) + p \quad (2.37)$$

$$\sigma_H \leq (\sqrt{\mu^2 + 1} + \mu)^2 (\sigma_h - p) + p \quad (2.38)$$

## 2.4 TIME-DEPENDENT BEHAVIOR

The previously discussed aspects of elasticity and rock failure are independent of time. However, the process of plate tectonics and seismic cycles give broad evidence for time-dependent behavior of the Earth's crust [Gomberg et al., 2000]. Therefore inelastic concept shall be discussed, the describe the evolution of stress and faulting taking into account time.

Tectonic processes load faults mechanically until a certain threshold is reached and accumulated stress and strain are released in the sudden sliding of an earthquake. Brace and Byerlee [1966] developed this stick-slip mechanism for earthquake cycles, which can be visualized by a blockslider attached to a spring, exerting a force on it

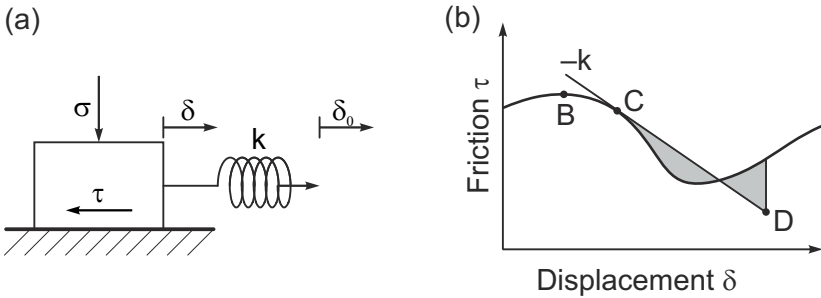


Figure 2.10: (a) Blockslider model of stick-slip behavior, loaded by a spring  $k$  and resisted by  $\tau$ . (b) Variation of friction as a function of displacement with a dynamic instability between points B and D, where the system cannot follow decreasing friction by stable sliding and the spring loading force [after Kanamori and Brodsky, 2004].

(Figure 2.10a). Under stable conditions the pulling force acted by the spring is equilibrated by the frictional resistance:

$$\tau = k(\delta_0 - \delta) = \mu\sigma. \quad (2.39)$$

Key to this model is a variation of the frictional resistance during sliding which might lead to a dynamic instability with a sudden large slip accompanied by a stress drop (Figure 2.10b). The spring attached to the blockslider tends to drag the slider along the line with slope  $-k$  in the  $\tau$ - $\delta$  graph. However, it is restricted by the frictional force  $\tau$  until a maximum of  $\tau$  is reached in the process (B). When the negative slope of  $\tau$  gets larger than that of the pulling force by the spring, the block moves suddenly from (C) to (D). Then the block remains stationary at (D) before the load reaches  $\tau$  and (very slow) stable sliding continues until an instability is encountered again [Scholz, 2002].

A large number of laboratory data has validated the blockslider model by showing that friction is not constant in time but varies as a function of the state of the sample defined by the sliding speed  $\dot{\delta}$  and the history of sliding of the sample defined by the state variable  $\theta$ . This was formulated in the rate- and-state dependent friction law, developed by Dieterich [1979] and Ruina [1983]:

$$\mu = \mu_0 + A \ln \dot{\delta} + B \ln \theta. \quad (2.40)$$

This model not only describes the initiation of failure, once the frictional forces are overcome, but also can be used to describe the coseismic slippage [McClure and Horne, 2012]. Furthermore, this is the basis for describing seismicity rates as results of varying stressing rate [Dieterich, 1994]. Assuming a uniform loading  $\tau(t) = \tau_0 + \dot{\tau}t$ , Equations 2.39 and 2.40 yield to a time-to-failure, that is when  $\dot{\delta}$  becomes

infinitely large, i.e. an earthquake occurs [Kanamori and Brodsky, 2004]:

$$t_f = \frac{A\sigma}{\dot{\tau}} \ln \left( \frac{\dot{\tau}}{H\sigma\delta_0} + 1 \right), \quad (2.41)$$

where  $H$  is a parameter of the fault.

In order to understand time-dependent failure from a different perspective, it is helpful to study crack growth in geological materials. The stress field around a crack is given by [Gross and Seelig, 2011]:

$$\sigma_{ij} = \frac{K_L}{\sqrt{2\pi r}} f_{ij}(\theta), \quad (2.42)$$

where  $r$  is the distance from the crack tip,  $K_L$  is the stress intensity factor describing the loading configuration of the crack and its failure mode.  $f_{ij}$  are functions of the angle  $\theta$  measured from the crack tip and depend on the failure mode (mode I, II or III) of the crack [Scholz, 2002]. Catastrophic crack growth occurs for  $K_L > K_c$ , where  $K_c$  is a critical stress intensity. Long-term experiments however, have shown that quasi-static crack growth occurs also for stress intensities substantially below  $K_c$  [Atkinson, 1984], a phenomenon known as subcritical crack growth. There are several micromechanical mechanisms leading to subcritical crack growth, such as stress corrosion, stress solution at crack tips [Rutter, 1976], mass transport by diffusion, ion exchange or microplasticity [Atkinson, 1984]. A simple description of subcritical crack growth as an Arrhenius-type temperature-dependent process is by the power law of Charles [1958]:

$$v = v_0 \exp \left( -\frac{H}{RT} \right) K_I^n, \quad (2.43)$$

where  $v$  is crack velocity,  $H$  is the activation enthalpy,  $R$  is the gas constant and  $T$  is temperature.  $v_0$  and  $n$  are material constants. Catastrophic brittle failure occurs once the crack density is high enough and cracks coalesce or crack velocity approaches sonic velocities. The complete time-dependent behavior under general loading conditions and including brittle deformation was obtained for Westerly granite by Lockner [1998]. The implications of this micromechanical behavior applied to tectonic earthquakes was discussed by Das and Scholz [1981] and can be used to naturally derive prominent phenomena of earthquake activity such as aftershocks [Gran et al., 2012], slow earthquakes, delayed multiple events, precursory slip and afterslip [Das and Scholz, 1981].

#### 2.4.1 Brittle creep

Laboratory creep tests have an important role in investigations for possible nuclear waste repositories, since prospective host rocks such

as rock salt or clayey formations have a pronounced subcritical creeping behavior [e.g. Fabre and Pellet, 2006; Carter et al., 1993]. However, also crystalline geomaterials such as granite and other sedimentary rocks such as sandstone and limestone show time-dependent deformation when subjected to long-term loading [Brantut et al., 2013].

Strain and strain rate curves for a typical creep experiment with constant load are shown in Figure 2.11. Three distinct phases can be seen: The primary creeping phase is marked by a high strain rate which reduces with time and accumulated creep strain. As strain rate is reduced, it approaches a constant value. According to Norton's law, this constant strain rate is dependent on the applied load by a power law [Norton, 1929]:

$$\dot{\epsilon} = A\sigma^n \exp\left(-\frac{H}{RT}\right). \quad (2.44)$$

If the load applied to a sample is high enough strain rate might increase at a certain point, which is related to the accumulated damage in the sample [Baud and Meredith, 1997]. Eventually, the accelerated creep leads to catastrophic failure. It is still under debate whether the secondary creeping phase is a distinct part of the creep process or if it is only the transition from the decelerating primary creeping phase to the accelerating tertiary creeping phase [Brantut et al., 2013].

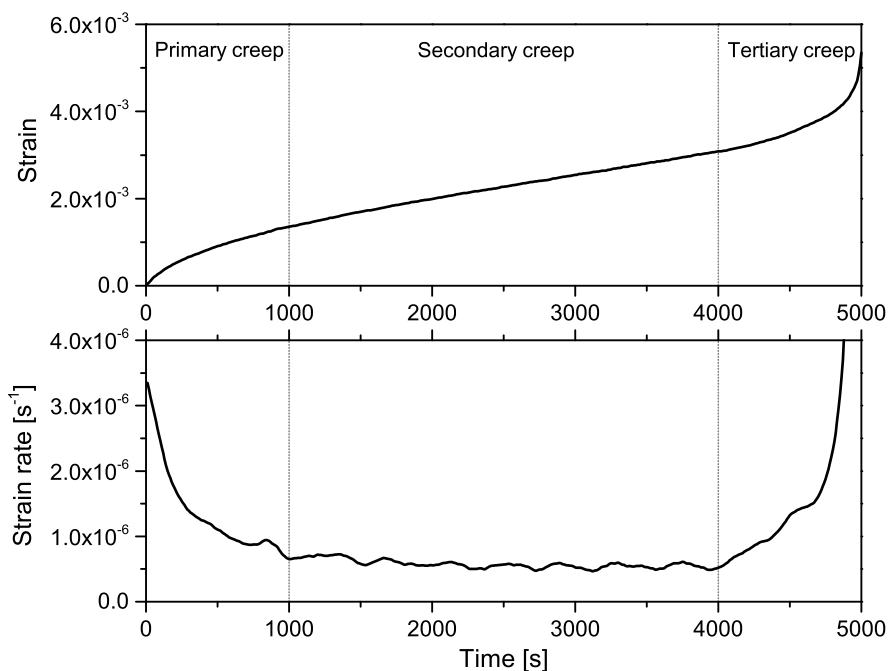


Figure 2.11: Creep curves for a sample of Thala limestone with  $p = 10$  MPa and differential stress of 95 MPa with the three creep regimes identified. Creep data is taken from Brantut et al. [2013]. The top figure shows creep strain, the bottom figure shows creep strain rate.

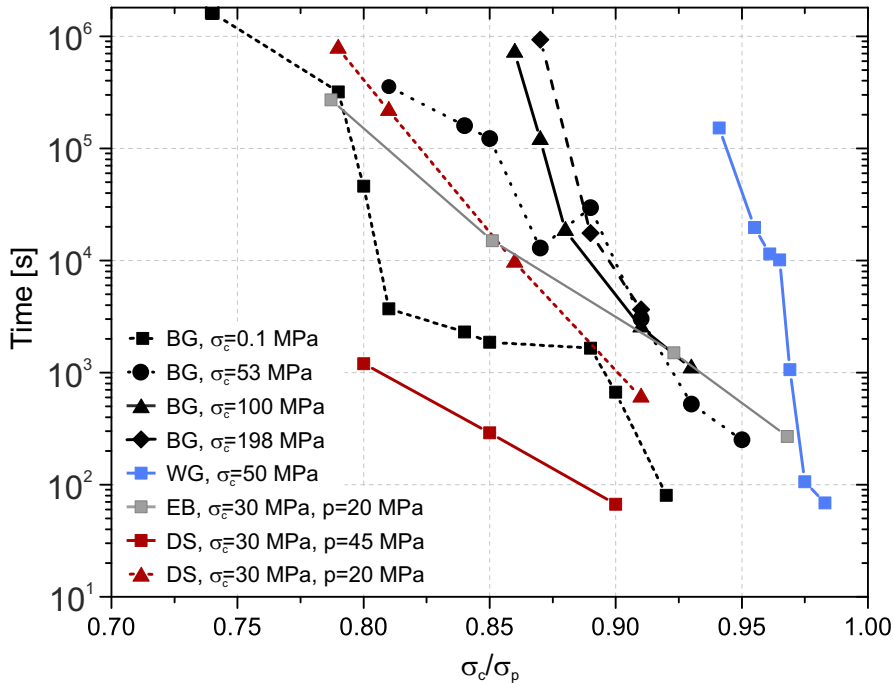


Figure 2.12: Experimental time-to-failure curves for Barre granite (BG), Westerly granite (WG), Etna basalt (EB) and Darley Dale sandstone (DS) for different confining pressures  $\sigma_c$  and fluid pressures  $p$ . Data from Brantut et al. [2013] and references therein.

Apart from creep strain rate  $\dot{\epsilon}$ , creep experiments can also be characterized by the time-to-failure  $t_f$ , that is the time from beginning of constant loading until macroscopic failure is reached. Since the creeping behavior is extremely non-linear for different stress loads,  $t_f$  varies over several orders of magnitude, when varying the applied load. Based on Equation 2.43, an empirical relation for  $t_f$  was derived [Charles, 1958]:

$$t_f = t_0 \left( \frac{\sigma}{\sigma_0} \right)^{-b}, \quad (2.45)$$

with instantaneous strength  $\sigma_0$  and material constants  $t_0$  and  $b$ . Since  $b$  is generally very large, taking values  $> 20$  also an exponential relation was derived by other authors [Wiederhorn and Bolz, 1970; Das and Scholz, 1981], describing experimental observations equally well [Brantut et al., 2013]:

$$t_f = t'_0 \exp \left( -b' \frac{\sigma}{\sigma_0} \right). \quad (2.46)$$

In Figure 2.12 time-to-failure curves for various rock types, collected from the literature [Brantut et al., 2013], are drawn.

## 2.5 EARTHQUAKE SOURCES

In the course of this thesis, results of seismological observations are used to evaluate the state of stress in the geothermal reservoir during stimulation (Chapters 4 and 6). In the following section, some fundamental basics of the seismological description of earthquake sources and their characterization are introduced.

### 2.5.1 Source models

Internal forces from slippage at a point must act in opposing directions in order to conserve momentum. If two force vectors are separated along the direction of a fault, a second couple of forces is necessary to conserve momentum (Figure 2.13). The resulting pair of force couples is called double couple. The force couple  $M_{ij}$  points in  $i$  direction and is separated along the  $j$  direction. Analogous to the stress tensor, the moment tensor build up by three double couples and three isotropic components, can be defined as:

$$M = \begin{pmatrix} M_{xx} & M_{xy} & M_{yz} \\ M_{yx} & M_{yy} & M_{yz} \\ M_{zx} & M_{zy} & M_{yy} \end{pmatrix}. \quad (2.47)$$

Since the moment tensor is symmetric ( $M_{ij} = M_{ji}$ ), each double couple describes two fault planes, termed nodal planes, which are equal from a seismological point of view (Figure 2.13). That means the displacement field, which can be derived from seismograms, is identical for displacements on either one of the nodal planes. Solving this ambiguity requires further geological constraints, a problem which is tackled for the geothermal reservoir in Soultz in Chapter 6. The moment tensor and the orientation of the fracture plane as given by the strike ( $0 \leq \phi \leq 360^\circ$ ), the dip ( $0 \leq \delta \leq 90^\circ$ ) and the rake ( $0 \leq \lambda \leq 360^\circ$ ) and the slip vector  $\vec{l}$  (Figure 2.14) define the most basic model of an earthquake [Shearer, 2009]. The seismic moment

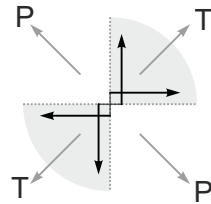


Figure 2.13: Single double couple in plane (black arrows) with nodal planes (dotted lines), domains of compression (gray shading) and the orientation of the P and T axes (gray arrows).

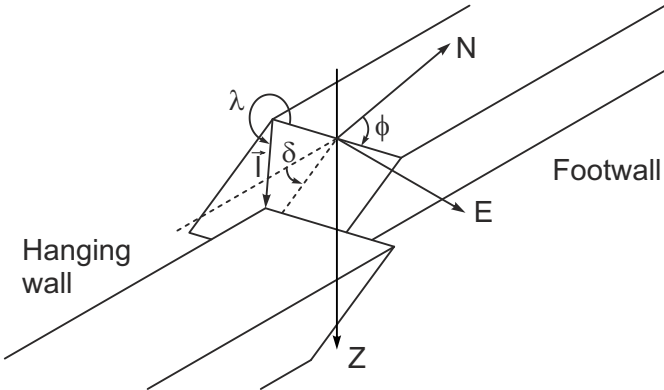


Figure 2.14: Naming convention of sliding blocks and definition of strike  $\phi$ , dip  $\delta$  and rake  $\lambda$  of a slip vector  $\vec{l}$  [after Lay and Wallace, 1995].

of an earthquake, the most basic measure of earthquake strength, is defined as

$$M_0 = G \bar{d} A, \quad (2.48)$$

with average displacement  $\bar{d}$  on the fault of area  $A$ . More generally,  $M_0$  can be computed from a moment tensor using:

$$M_0 = \frac{1}{\sqrt{2}} \left( \sum_{ij} M_{ij}^2 \right)^{1/2}. \quad (2.49)$$

In order to understand source processes of earthquakes, the sources need to be characterized based on seismological observation of displacement. The displacement field for P-waves of a spherically symmetric source (e.g. an explosion) is [Shearer, 2009]:

$$u(r, t) = \left( \frac{1}{r^2} \right) f(t - r/a) + \left( \frac{1}{r\alpha} \right) \frac{\partial f(t - r/a)}{\partial \tau}, \quad (2.50)$$

where  $a$  is the P-wave velocity and  $f(t - r/a)$  is the source-time function of the earthquake source. The first term, quadratic in  $r$ , is called the near-field term and represents the permanent static displacement. This part is the relevant term to compute the static displacement field, which increases and decreases stress in the vicinity of the fault plane and might lead to enhancement or inhibition of aftershock activity following a main shock [Toda and Stein, 2003]. This is used in the analysis of the triggering effect during reservoir stimulation by static stress transfer in Chapter 4. See Section 2.6.1 for further background. The second term in Equation 2.50 is linear in  $r$  and is called the far-field term. It represents the dynamic displacement radiated as seismic waves from the seismic source. This displacement field is used to derive the mechanism of faulting (Figure 2.8 bottom) based on the polarity of the first arrival [Shearer, 2009] and the moment tensor components  $M_{ij}$ . The displacement fields of double couple sources

is of course more complicated, but still contains near-field and far-field terms with their respective meaning as described above for the spherically symmetric source [Shearer, 2009].

### 2.5.2 Fundamental relations in seismology

Historically, the strength of earthquakes was quantified by an earthquake magnitude, based on the displacements recorded by seismographs and corrections representing the travel path of the seismic waves and the recording instrument [Lay and Wallace, 1995]. To represent the vast range of earthquake strength spanning many orders of magnitude in terms of seismic moment, all magnitude scales are logarithmic measures. The problem with these scales is, that they saturate for large earthquakes, that is above a certain earthquake strength a constant magnitude is obtained [Lay and Wallace, 1995]. Due to this limitations a new magnitude scale was introduced by Kanamori [1977], which is based on the seismic moment instead of frequency-dependent amplitudes. He defined the moment magnitude  $M_w$  as:

$$M_w = \frac{\log M_0}{1.5} - 6.07, \quad (2.51)$$

with  $M_0$  measured in Nm.

Earthquakes are the response of a rock volume to a stressing history above a certain failure criterion. Rupture stops when stresses on the fault plane are reduced such that stable conditions prevail. Therefore, stresses acting on the fault plane are reduced and we can define the stress drop  $\Delta\sigma$  as the difference in stress state on the fault plane before and after the event:

$$\Delta\sigma = \frac{1}{A} \int_S (\sigma(t_1) - \sigma(t_0)) dS. \quad (2.52)$$

For a penny-shaped fault in 3D space Eshelby [1957] obtained

$$\Delta\sigma = \frac{7\pi G \bar{d}}{16r} = \frac{7M_0}{16r^3}, \quad (2.53)$$

with the fault radius  $r$ . To derive stress drops from seismic recordings, a rupture model for earthquake sources needs to be established to obtain  $r$ . In the literature, two models are used: the Brune [1970] model, a simple kinematic model of a circular fault, and the Madariaga [1976] model, a dynamic model of a circular fault with an elliptical slip distribution. The fault radius is obtained from

$$r = \frac{k\beta}{f_c}, \quad (2.54)$$

where  $k$  is a constant depending on the model,  $\beta$  is the S-wave velocity and  $f_c$  is the corner frequency obtained from the seismogram spectrum [Shearer, 2009]. Since the Brune [1970] and the Madariaga [1976]

models yield different values of  $k$ , the estimates of  $\Delta\sigma$  by the Brune [1970] model are about 5 times smaller than that from the Madariaga [1976] model. Also we have to note the cubic dependency of stress drop on the source radius and therefore on the corner frequency.

Stress drops of fluid-injection induced seismicity has been specifically analyzed for the stimulation experiments at KTB [Jost et al., 1998], at Soultz-sous-Forêts [Charléty et al., 2007] and in Basel [Goertz-Allmann et al., 2011]. In general, similar values have been obtained as for natural seismicity. Here stress drops are regarded as approximately constant over a wide range of earthquake magnitudes with a log-mean value of about 3 MPa [Kanamori and Anderson, 1975; Abercrombie, 1995].

### 2.5.3 Two empirical relations of earthquake statistics

Gutenberg and Richter [1954] noted that the number  $N$  of the much more frequent small earthquakes and that of the larger earthquakes are related by a power law:

$$\log N = a - bM, \quad (2.55)$$

where  $N$  is the number of events with magnitude smaller than  $M$ ,  $a$  is a parameter representing the overall seismic activity and the  $b$ -value is the important scaling parameter. Typically,  $b$ -values in the order of 0.8-1.2 are found in natural seismicity.

Since earthquake magnitudes are determined by the rupture area, variations of the  $b$ -value may be attributed to changes of the size distribution of the natural fault network. Aki [1981] propose the relation  $b \approx D/2$ , where  $D$  is the fractal dimension of the fault net-

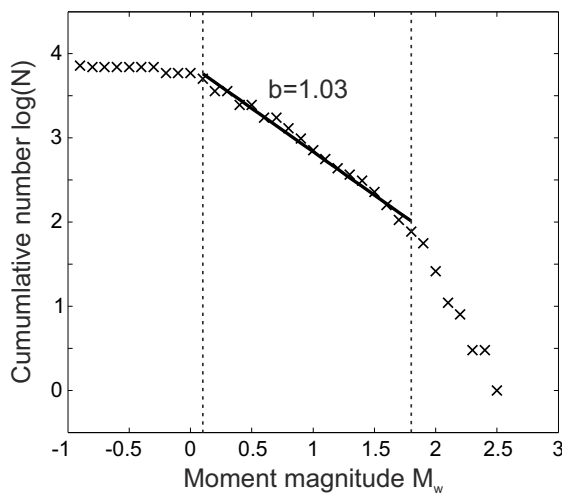


Figure 2.15: Magnitude-frequency plot of the stimulation of the GPK2 in June/July 2000 in Soultz-sous-Forêts with  $b$ -value estimate using routines from Wiemer [2001].

work. In other studies, changes of the b-value are related to changes of the stress regime. E.g. Schorlemmer et al. [2005] found that the b-value varies systematically with the stress regime with low values for areas of thrust faulting and high values for normal faulting areas. Similar observations and dependencies of the b-value on the level of stress have been obtained in the laboratory by Amitrano [2003]. For hydraulic fracturing, much higher b-values in excess of 2.0, are observed, meaning relatively more smaller earthquakes [Maxwell et al., 2010]. The reason is the different failure mode and the continuous fracture growth in hydraulic fracturing compared to the sudden slip-page of faults in natural or induced shear faulting. Figure 2.15 shows the magnitude-frequency plot for the stimulation of well GPK2 in Soultz in June/July 2000, a value of  $b = 1.03$  is obtained, which is a typical value also for natural seismicity. Choosing a different magnitude window for the fit might result in a different estimate of the b-value. For the same stimulation Dorbath et al. [2009] use the magnitude window [1 ... 1.8] for the b-value fit and obtain a considerably larger value of 1.23. Michelet [2002]; Bachmann et al. [2012] systematically studied the evolution of the b-value in geothermal reservoirs in Soultz and Basel, respectively. While Michelet [2002] found b-values increasing with distance from the injection point GPK2, Bachmann et al. [2012] found b-values decreasing with distance for the Basel stimulation.

The second empirical law I introduce here is Omori's law describing the rate of aftershock activity following a main shock [Omori, 1894]. He found that the number of aftershocks decreases with time, following a power law. Later, the law was modified to a more general relation [Utsu et al., 1995]:

$$n(t) = \frac{K}{(c + t)^p}, \quad (2.56)$$

where K and c are constants and the exponent p typically takes values in the order of 1-1.2 [Shcherbakov et al., 2004].

The aftershock activity following a main shock is an expression of localized stress increases due to the main shock. These stresses are dissipated by seismic activity that is much smaller than the main shock [Båth, 1965] and are equilibrated over time. Possible mechanisms for the power-law time dependency are fluid diffusion [Nur and Booker, 1972], rate-and state-dependent friction [Dieterich, 1994] and stress corrosion [Das and Scholz, 1981].

Langenbruch and Shapiro [2010] applied Omori's law to the decrease of seismic activity following shut-in phases of reservoir stimulations. They found that the law is still holding for such cases, albeit at much larger values of  $p > 2$ . Narteau et al. [2009] show that both statistical laws, the Gutenberg-Richter magnitude-frequency relationship and Omori's law on aftershock activity are dependent on the stress state in the Earth's crust.

It has been shown many times, that the mechanisms of time-dependent brittle failure, described in Section 2.4, naturally lead to seismic event rates as described by Omori's law [Das and Scholz, 1981; Gomberg et al., 2000; Amitrano and Helmstetter, 2006; Gran et al., 2012].

## 2.6 BACK TO GEOMECHANICS

Seismological observations deliver valuable data to learn about the sub-surface geomechanics. The following section describes some of the tools, that can be used.

### 2.6.1 *Static stress transfer*

Analytical solutions that describe the displacement field induced by static dislocations were derived by Okada [1992] for a homogeneous half-space and later extended to multi-layered elastic and viscoelastic media by Wang et al. [2003, 2006] using a Green's function approach. Based on this approach, aftershock sequences following large earthquakes could be successfully described by modeling static stress changes [King et al., 1994]. Several numerical models use the redistribution of stress after failure of a slip patch to propagate failure to neighboring slip patches and thus obtain rupture areas, and finally, seismic event magnitudes.

The displacement field arising from a slippage along a fault plane causes stress changes not only on the fault plane, but also in the 3D half-space around it (Figure 2.16). Observations of successive slippage of sections of big faults in sequences of earthquakes [e.g. Stein et al., 1997] gave rise to the model of earthquake triggering by static stress transfer [King et al., 1994]. This model is also used to explain the spatial clustering of aftershocks around the main shock rupture plane [King et al., 1994; Seeber and Armbruster, 2000; Toda and Stein, 2003]. The influence of static stress transfer on induced seismicity during geothermal reservoir stimulation is the central topic of Chapter 4, published in Schoenball et al. [2012] and was also analyzed for the Basel EGS by Catalli et al. [2013]. In the following, the principle of this kind of analysis is presented.

The analysis consists of several steps. First, the focal mechanism solutions of the potentially triggering earthquake sources need to be determined and fault planes need to be identified among the nodal planes. Second, the geometry of the slippage must be determined. This includes the dimensions of the fault plane and the displacement on the fault. While detailed models of the slip distribution are possible and available for large tectonic earthquakes [e.g. for the 2011 Tohoku-Oki earthquake see MacInnes et al., 2013, and references therein] assumptions need to be made for small earthquakes regard-

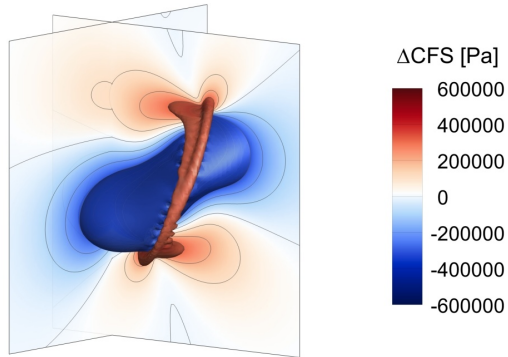


Figure 2.16: Changes of the Coulomb stress by static stress transfer on a right-lateral fault parallel to the rupture plane.

ing the stress drop  $\Delta\sigma$  and the actual slip distribution (see Chapter 4). Third, the static stress transfer is calculated. This can be done using analytical solutions for the displacement field in a half-space based on the work by Okada [1992] and implemented in e.g. the Coulomb software [Toda et al., 2011] or the EDCMP code [Wang et al., 2003] or using numerical means such as displacement discontinuity approach [e.g. in Yamashita, 1998; McClure and Horne, 2010].

Other models rely on a cellular automaton technique to transfer stresses from one fault element to neighboring elements by a generic stress transfer pattern [Bak and Tang, 1989]. This model is used e.g. in Baisch et al. [2010] to model the propagation of hydraulic enhancement of a fault zone.

Having obtained the displacement field from a dislocation, either from analytical or numerical methods, Hooke's law (Equation 2.22) can be used to obtain the stress change tensor for any point in the volume. The potential for slip will be enhanced or retarded by a change in Coulomb failure stress,  $\Delta\text{CFS}$  given by:

$$\Delta\text{CFS} = \Delta\tau - \mu(\Delta\sigma - \Delta p), \quad (2.57)$$

where the  $\Delta$  denotes the change in stress of  $\tau$ ,  $\sigma$  and  $p$ . To calculate the stress change towards or away from Coulomb failure a hypothetical receiver fault must be assumed. If no particular receiver fault is known, an optimally oriented fault, that is a fault whose orientation is closest to failure under given stress and frictional conditions, is typically assumed [King et al., 1994]

### 2.6.2 *Inversion of focal mechanism solutions*

A number of inversion methods exist which can be used to obtain the stress tensor from observations of slippage either based on slickensides or earthquake focal mechanisms [Angelier, 1979; Gephart and Forsyth, 1984; Michael, 1984; Rivera and Cisternas, 1990]. A review of these methods is given by Célérier et al. [2012] and Maury et al.

[2013]. This technique is the basis of the majority of the data points that are contained in the World Stress Map [Heidbach et al., 2010] and is widely used in understanding the mechanics of large earthquakes and to study the strength and stress states of fault zones [Hardebeck, 2012; Hasegawa et al., 2012]. In the following, the method of Michael [1984], further developed by Hardebeck and Michael [2006] is outlined, since it is used to analyze the stress field during the stimulation of well GPK2 in Chapter 6.

The strike, dip and rake angles from a focal mechanism solution yield the outward normal vector  $\vec{n}$  from the fault plane and  $\vec{l}$  the slip vector along the fault plane (see Figure 2.14). The primary hypothesis of stress inversion techniques is that the direction of tangential traction on the fracture plane is almost parallel to the slip vector [Bott, 1959]:

$$\frac{\vec{t}(\vec{n}, \sigma)}{|\vec{t}(\vec{n}, \sigma)|} = 1, \quad (2.58)$$

where  $\vec{t}(\vec{n}, \sigma)$  is the shear stress on the fault plane with normal vector  $\vec{n}$ , due to the stress tensor  $\sigma$ . Furthermore, it is assumed that the rocks are homogeneous for a set of focal mechanisms used for inversion, and that the focal mechanisms are independent of each other, i.e. events are not cross-triggered. The method proposed by Michael [1984] requires a fourth hypothesis, which assumes that the shear stress is the same on all fault planes. Since only relative magnitudes of stress can be obtained from inversion, the shear stress is set equal to 1.

$$|\vec{t}| = 1 \quad (2.59)$$

With the constraint that the isotropic stress is zero ( $\sigma_{33} = -(\sigma_{11} + \sigma_{22})$ ), an equation system for the slip vectors  $\vec{l}_i$  is obtained:

$$\begin{pmatrix} A_1 \\ A_2 \\ \vdots \\ A_k \end{pmatrix} \begin{pmatrix} \sigma_{11} \\ \sigma_{12} \\ \sigma_{13} \\ \sigma_{22} \\ \sigma_{23} \end{pmatrix} = \begin{pmatrix} \vec{l}_1 \\ \vec{l}_2 \\ \vdots \\ \vec{l}_k \end{pmatrix}, \quad (2.60)$$

where the  $A_i$  contains the orientation of the fault planes of the  $k$  focal mechanisms used for inversion. The least squares solution is then given by [Menke, 2012]:

$$A^T A \sigma = A^T \vec{l}. \quad (2.61)$$

Michael [1984] use Gaussian elimination to solve this system.

The method described above has been expanded by Hardebeck and Michael [2006] to invert for regionally or temporally varying stress

fields. They used a damped inversion scheme to obtain the simplest model that fits the spatially or temporally varying stress field. The model should contain complexities only when they are critically demanded by the data. This is achieved by introducing a damping matrix  $D$  and jointly minimizing the data misfit and the model complexity [Hardebeck and Michael, 2006]. This is achieved by solving [Menke, 2012]:

$$(A^T A + e^2 D^T D) \sigma = A^T \vec{l}, \quad (2.62)$$

where  $e$  is the parameter determining the strength of the damping.

A posteriori, uncertainties of the resulting stress field are accounted for by bootstrap resampling of the input data set [Michael, 1987b]. Thus, new data sets are generated by random sampling with replacement of  $k$  individual focal mechanisms. Thus, some mechanisms may be represented several times or be absent in a new data set. Hence, the scatter inherent in the data set can be captured, without assembling a whole new data set from repeated measurements. An example of a time-resolved stress inversion with bootstrap resampling for estimation of confidence intervals is shown in Figure 2.17.

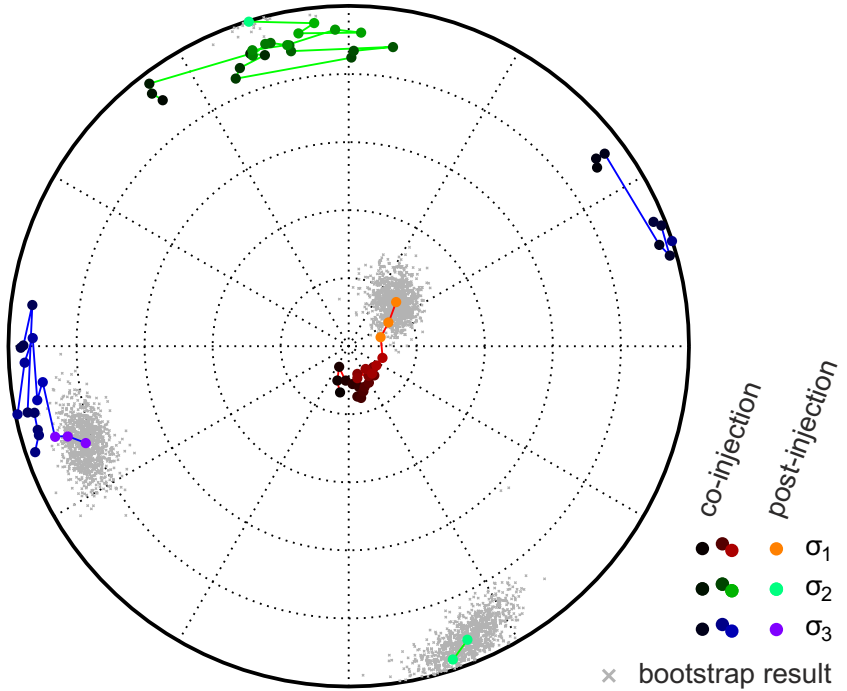


Figure 2.17: Temporally resolved orientation of the stress tensor on a lower hemisphere projection obtained from inversion of 715 focal mechanism solutions, recorded during the stimulation of well GPK2 at Soulz-sous-Forêts, France. See Chapter 6 for details on the dataset and method. Each bin contains 30 events. Brighter colors correspond to later times; bootstrap results are shown only for the last time bin.

# 3

---

## SOULTZ-SOUS-FORÊTS PILOT EGS

---

In this chapter a brief overview on the development of the Soultz-sous-Forêts pilot EGS is given [Baria et al., 1995; Genter et al., 2010]. Emphasis is laid on studies with implications for the work presented in this thesis, in particular to analyses involving the stimulation of well GPK2, which is the main subject of Chapters 4-6.

After the experiences collected at the Fenton Hill and Rosemanowes test sites, search for a new European pilot site was initiated under coordination of the European Commission [Baria et al., 1995]. The former Pechelbronn oilfield was very well characterized by old oil wells, with about 500 temperature measurements. Those measurements were used to identify and characterize the temperature anomaly at Soultz, which is trending NE-SW along the Soultz horst-and-graben structure, defined by normal faults. The thermal gradient down to 1000 m was known to exceed  $110 \text{ K km}^{-1}$ . However, the majority of existing wells were only 800 – 1000 m deep [Genter et al., 2010].

The Soultz horst-and-graben structure is situated close to the western main boundary fault of the Upper Rhine graben, which is part of the European Cenozoic rift system. The fractured granite is overlain by 1400 m of sediments. Genter et al. [2010] recognized two kinds of main natural fractures in the granitic rock: individual fractures seen on cores and in well logs and larger zones of highly clustered fractures with 10 – 20 m thickness. The reservoir stretches across two different granite facies. Down to a depth of about 4800 m a porphyritic monzo-granite is found, and below a fine-grained two-mica granite occurs [Hooijkaas et al., 2006; Genter et al., 2010].

Although the region of Soultz experienced natural earthquakes as large as magnitude 4.8 in 1954 10 – 20 km south-east of Soultz [Evans et al., 2012], the area was classified as a low seismic hazard region by Burkhard and Grünthal [2009].

### 3.1 FIELD DEVELOPMENT

In 1987, the project started with the drilling of well GPK1 to a depth of 2002 m where a temperature of 140 °C was reached [Baria et al., 1995]. While the temperature gradient was stable at around  $100 \text{ K km}^{-1}$

down to about 1000 m it decreased strongly to only  $5 \text{ K km}^{-1}$ , when the convective cell of the Soultz horst was reached (Figure 3.1). Three monitoring wells were created by deepening of former oil wells 4550, 4601 and 4616 in 1988 down to 1500 m, 1600 m and 1420 m, respectively and seismic monitoring stations were placed (Figure 3.2). The well EPS1 was deepened from 930 m by continuous coring to 2227 m. These cores are the basis of the characterization of the fracture network [Genter and Trainea, 1992; Meller et al., 2014]. In 1991, GPK1 was stimulated for the first time in the depth section from 1420 – 2002 m. One year later it was deepened to 3590 m and a temperature of  $168^\circ\text{C}$  was reached. The well was stimulated by massive fluid injection in September 1993 in the depth section of 2850 – 3590 m and tested in October of the same year. Shear stimulation was initiated and was followed by hydraulic fracturing once the wellhead pressures surpassed 10 MPa and seismicity started to migrate upwards [Cornet et al., 2007].

In 1995, well GPK2 was drilled to 3876 m targeting the previously stimulated volume 450 m away from GPK1. The open-hole section from 3211 – 3876 m was stimulated with wellhead pressures of up to 12 MPa. The well was restimulated in 1996 showing a prominent Kaiser effect [Baisch and Harjes, 2003] with seismicity starting only after the hydraulic pressures of the previous stimulation a year before were reached (Figure 3.3d). The demonstrated the long-term effect of shear stimulation on the hydraulic regime of the reservoir. In 1997, a four month circulation test between GPK1 as producer and GPK2 as injection well was conducted at flow rates of  $251 \text{ s}^{-1}$

With new funding available, well GPK2 was deepened to 5000 m with the objective of reaching a bottom hole temperature of  $200^\circ\text{C}$ . GPK2 was stimulated over 6 days, beginning with injection of  $400 \text{ m}^3$

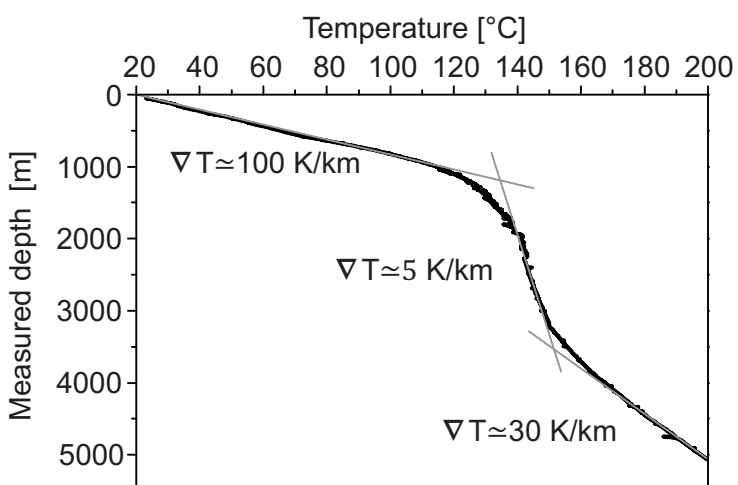


Figure 3.1: Temperature profile measured in well GPK3, showing the convection cell with a very low geothermal gradient between 1000 – 3500 m.

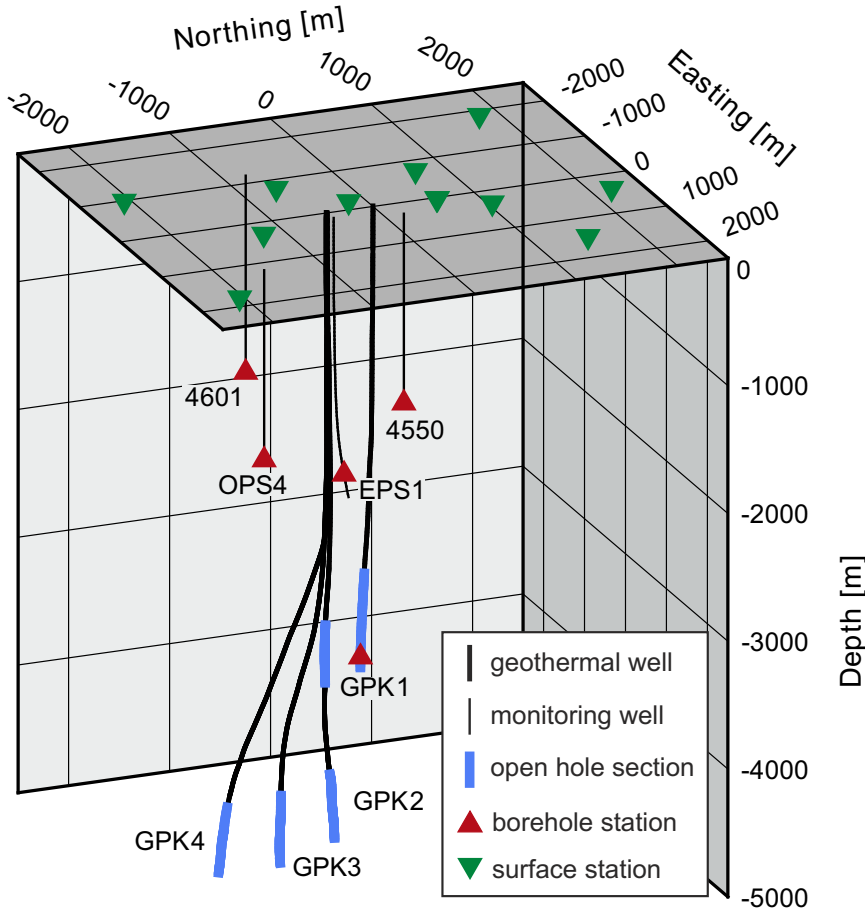


Figure 3.2: Current setup of the Soultz project, with the intermediate reservoir around 3500 m depth and the deep reservoir in around 5000 m depth.

of heavy brine with a density of  $1.2 \text{ g cm}^{-3}$  followed by  $23\,000 \text{ m}^3$  of fresh water. The heavy brine was chosen to encourage downward growth of the stimulated volume [Weidler et al., 2002]. The stimulation was followed by an injection test 7 days after the end of the stimulation. It lasted 2.5 days (Figure 3.4a) and only few seismic events were recorded. However, one day after this test, which means ten days after the end of the stimulation, the largest seismic event was recorded with a magnitude of 2.6 [Dorbath et al., 2009]. The well GPK3 was subsequently drilled to a target zone at 5093 m depth, defined by the results of the microseismic monitoring of the GPK2 2000 stimulation, which is 650 m away from GPK2. It was stimulated by the largest stimulation run in Soultz, which included also a period of dual stimulation in GPK2 and GPK3 for about 40 hours (Figure 3.4c). In the course of this stimulation the largest event ever recorded in Soultz, which had a magnitude of  $M_w = 2.9$  [Dorbath et al., 2009], was induced. Starting in August 2004, the well GPK4 was drilled, again 650 m away further south-east of GPK3, reaching a

depth of 5105 m. During the stimulation of GPK4 no clear overlap of induced seismicity with the previously engineered reservoir around GPK2 and GPK3 could be achieved, leaving a zone of no seismic activity between the two wells. This can be either attributed to a highly conductive or a sealing structure, inhibiting hydraulic connection between GPK3 and GPK4 [Kohl et al., 2006]. The restimulation of GPK4 in 2005 did not improve the connectivity to the other wells, but again showed a very clear Kaiser effect (Figure 3.4d).

### 3.2 FIELD OPERATION

A first circulation test of the deep reservoir was run for more than 5 months in 2005, involving the wells GPK2-4 [Cuenot et al., 2011]. Tracer tests revealed different flow patterns in the reservoir, with a short-scale and a large-scale loop between wells GPK2 and GPK3 and weak connection of GPK4 to the large-scale loop [Sanjuan et al., 2006].

Construction of the ORC power plant with an electrical output of 1.5 MW<sub>e</sub> began in 2007 and was commissioned in 2009. Since then, the long-term testing of the reservoir and power production started. A 9 month circulation test was conducted in 2009 and the 2010 circulation lasted 11 months [Cuenot et al., 2011]. During the 2010 circulation, GPK2 was produced at 181 s<sup>-1</sup>, and GPK3 was used for injection. Later, injection into GPK3 was reduced to 151 s<sup>-1</sup> and the remainder was injected into GPK1. The wellhead pressure at GPK3 was at 5 MPa and reduced to 4 MPa after start of injection into GPK1. During this circulation, 411 events were detected with highest activity during the reinjection into GPK3 only, when the wellhead pressure was in the order of 5 MPa [Cuenot et al., 2011].

In 2011, the injection scheme was changed for the circulation in January-April [Genter et al., 2012], in order to reduce pressure in GPK3 and to mitigate seismicity. Production continued from GPK2 at a rate of up to 261 s<sup>-1</sup>, but reinjection was now about 131 s<sup>-1</sup> into GPK1 and 91 s<sup>-1</sup> into GPK3. As a consequence, the wellhead pressure in GPK3 never exceeded 2 MPa and was always below 1 MPa in GPK1. Only 4 events were recorded during the circulation test.

In summary it can be said, that there is a critical reinjection pressure of about 5 MPa, above which seismicity starts to occur. Circulation can be maintained with only negligible seismicity, when reinjection pressures above this critical pressure are avoided. This is a very important prerequisite for long-term production of an EGS. Today, the system of four production and injection wells (Figure 3.2), makes it the first multi-well EGS world-wide, and with potential for optimization of the reservoir management [Held et al., 2014].

Well	Date	Depth range [m MDI]	Volume [m <sup>3</sup> ]	Duration [days]	Rate [l s <sup>-1</sup> ]	Pressure [MPa]	Recorded Seismicity	Largest Event	Reference
GPK <sub>1</sub>	Sep 1993	2850 – 3400	25 300	17	38	11	Surface: 127 Downhole: 17 000	$M_d = 1.9$	Baria et al. [1995] Jones et al. [1995]
GPK <sub>1</sub>	Oct 1993	2850 – 3400	19 300	5	51	10	Surface: 38 Downhole: 1700	$M_d = 1.7$	Baria et al. [1995] Jones et al. [1995]
GPK <sub>2</sub>	1995	3200 – 3650	30 000	11	56	12	Downhole: 3916	$M_{w} = 0.1$	Gérard et al. [1997]
GPK <sub>2</sub>	1996	3200 – 3650	28 000	7	78	13	Downhole: 3465	$M_{w} = 0.3$	Gérard et al. [1997]
GPK <sub>2</sub>	2000	4400 – 5050	23 400	6	50	15	Surface: 7215 Downhole: 14 000	$M_{w} = 2.6$	Dorbath et al. [2009] Dyer [2001]
GPK <sub>3</sub> (+ GPK <sub>2</sub> )	2003	4556 – 5101 (4400 – 5050)	34 000 3400	11 2	80 25	16 8	Surface: 3253 Downhole: 21 979	$M_{w} = 2.9$	Dorbath et al. [2009] Dyer et al. [2004]
GPK <sub>4</sub>	2004	4500 – 5000	9 300	3.5	45	17	Surface: 794 Downhole: 22 718	$M_{w} = 2.3$	Dorbath et al. [2009] Dyer [2005]
GPK <sub>4</sub>	2005	4500 – 5000	12 300	4	45	18	Surface: 764 Downhole: 9570	$M_{w} = 2.7$	Dorbath et al. [2009] Dyer [2005]

Table 3.1: Overview of major hydraulic stimulations performed at the Soultz-sous-Forêts EGS site.  $M_d$  is duration magnitude,  $M_w$  is moment magnitude.

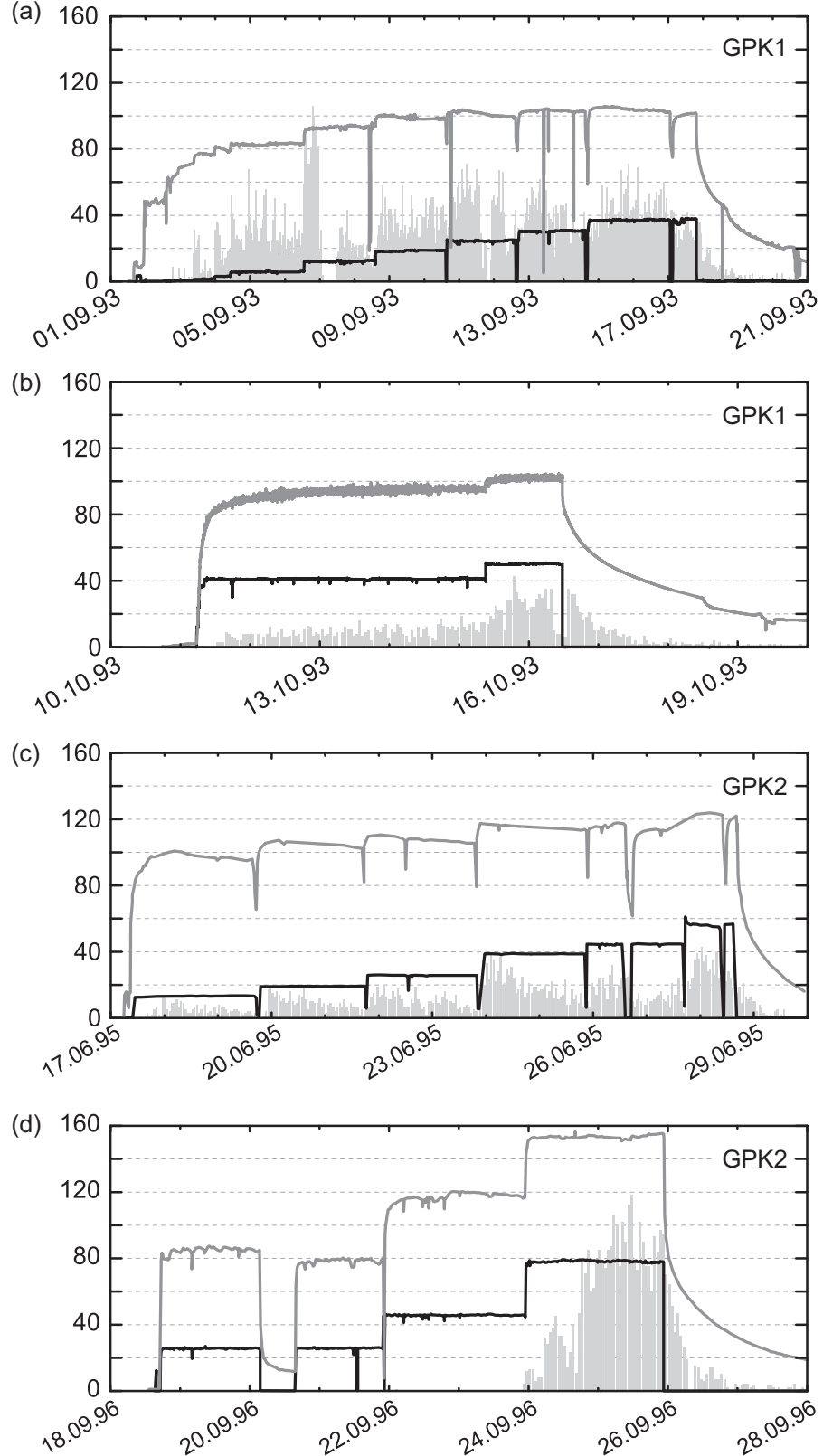


Figure 3.3: Stimulations of wells GPK1 and GPK2 (1993 - 1996) of the intermediate reservoir at around 3000 – 3500 m. See Table 3.1 for details. Flowrate [ $\text{l s}^{-1}$ ] is plotted in black, wellhead pressure [bar] in gray and hourly event rate is drawn as gray bars.

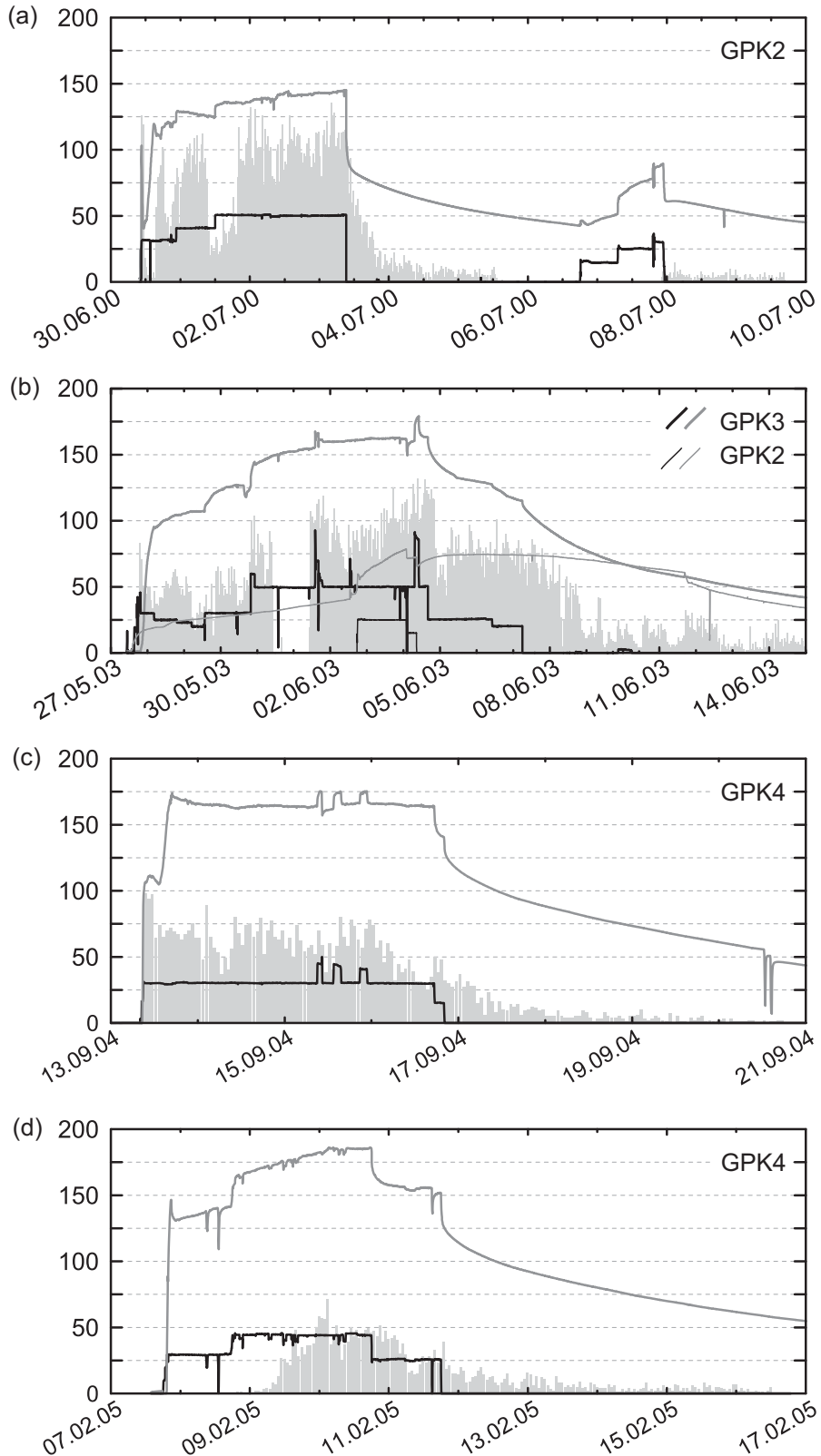


Figure 3.4: Stimulations of wells GPK2, GPK3 and GPK4 (2000 - 2005) of the deep reservoir at around 4500 – 5000 m, see Table 3.1 for details. Flowrate [ $\text{l s}^{-1}$ ] is plotted in black, wellhead pressure [bar] in gray and hourly event rate is drawn as gray bars.

### 3.3 RESULTS OF GEOPHYSICAL ANALYSES

The stress field in Soultz was determined by Cornet et al. [2007] based on observations along and of the stimulation of GPK1 down to 3590 m. The analysis was confirmed by Valley [2007] down to 5000 m. The orientation of  $\sigma_H$  is N169  $\pm$  14° and the principal stress magnitudes are [Cornet et al., 2007]:

$$\begin{aligned}\sigma_v &= 33.8 + 0.0255(z - 1377) \text{ MPa}, \\ \sigma_H &= [0.95 \dots 1.1]\sigma_v, \\ \sigma_h &= 0.54\sigma_v.\end{aligned}\tag{3.1}$$

and a pore fluid pressure of

$$p = 0.9 + 0.0098z \text{ MPa},\tag{3.2}$$

where the depth  $z$  is given in meters. The very large differential stresses imply a critically stressed rock mass which requires a large coefficient of friction in the order of 0.8 – 1.0 [Cornet et al., 2007; Evans et al., 2005] to prevent faulting and depending on the assumed value of cohesion. Although the stress field is at the verge of normal faulting to strike-slip faulting, focal mechanism solutions obtained are predominantly of normal fault type with only few strike-slip events [Cuenot et al., 2006; Charléty et al., 2007; Horálek et al., 2010]. This is particularly true for the GPK2 stimulation in 2000 (Figure 3.5). Stress drops for few large magnitude events were analyzed by Charléty et al. [2007] and found to be in the typical range observed for natural earthquakes [Abercrombie, 1995].

A 3D geological model was derived based on wellbore imaging, flow logs (e.g. Figure 3.6), VSP surveys and microseismic monitoring [Sausse et al., 2010]. Major fault structures with influence on the

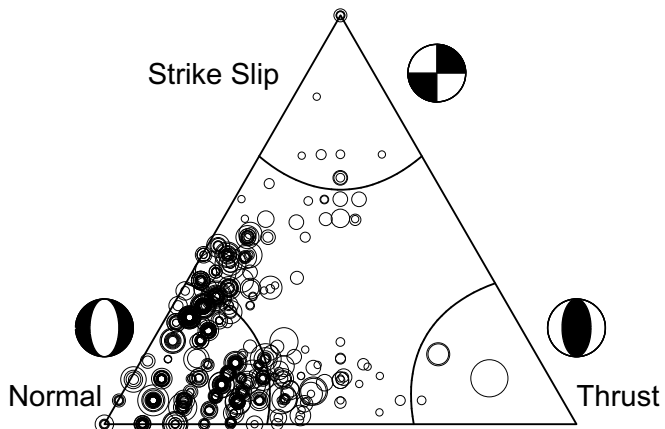


Figure 3.5: Focal mechanism solutions from the GPK2 stimulation in June to July 2000 in a ternary graph after Frohlich et al. [1992].

hydraulic flow in the reservoir or derived from the occurrence of microseismicity are shown in Figure 3.7. One major fault zone termed GPK3-FZ4770 could be traced from GPK3 to GPK2, where it is identical to GPK2-FZ3900, and continues at least up to GPK1. With the exception of GPK4, this fault zone connects all production and injection wells. This structure is also host to relatively large events during injection [Cuenot et al., 2008] and also during production [Genter et al., 2012]. Seismicity on this structure is analyzed in Chapter 4.

The occurrence of seismic multiplets was investigated for the 1993 stimulation of GPK1 by Bourouis and Bernard [2007] and Moriya [2003]. Several asperities exhibiting repeated rupture were identified, some of them accumulating slip in excess of 10 cm. Bourouis and Bernard [2007] proposed a conceptual fault model of locked asperities within an otherwise creeping fault, that loads the asperities continuously until the strength of the asperities is reached and a seismic event occurs and the cycle repeats. This model is analogous to the blockslider model discussed in Section 2.4. Further observations of aseismic motion could be made directly at the wells, where Cornet et al. [1997] identified slippage of up to 4.3 cm, which would correspond to a magnitude 3.5 earthquake. However, this is 2 orders of magnitude larger than the observed seismicity. Therefore, the slip can only be attributed to aseismic movement.

First efforts to derive a 4D tomographic image of the reservoir using P-waves were taken by Cuenot et al. [2008] and later refined by Calo et al. [2011]. They find a low velocity zone in the stimulated

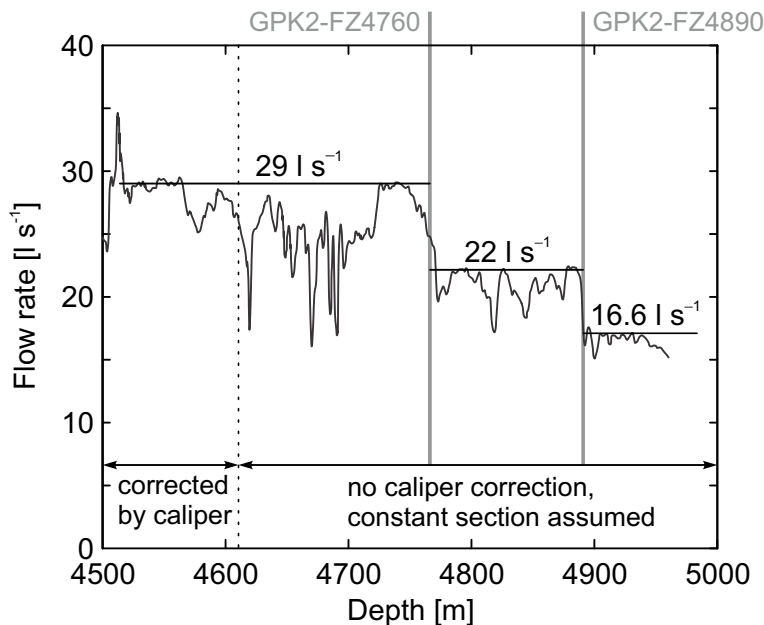


Figure 3.6: Flowlog obtained during the stimulation of the deep section of GPK2 in 2000 [Dyer, 2001], with identification of faults after Sausse et al. [2010].

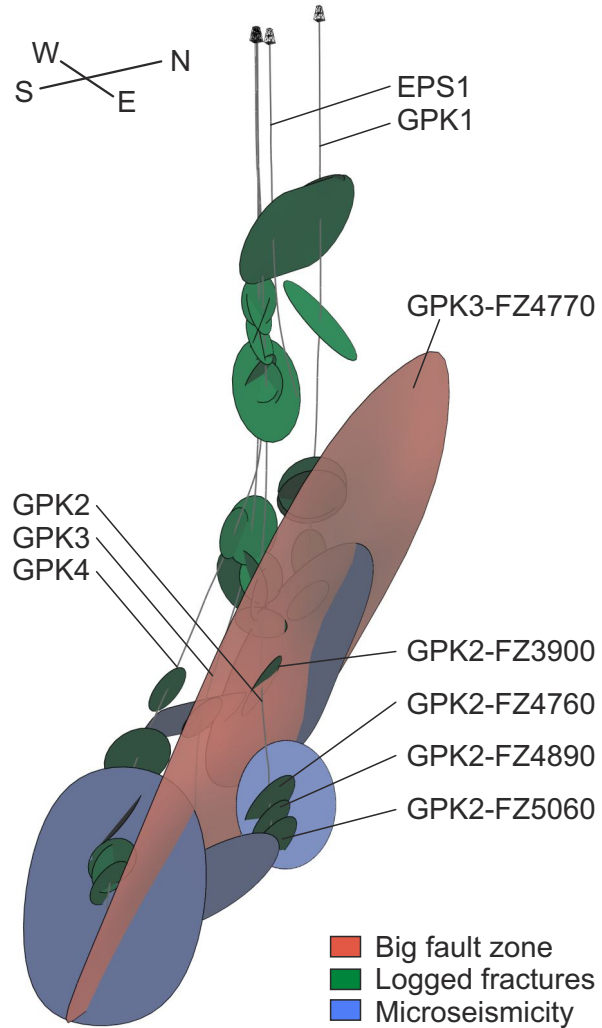


Figure 3.7: Geological model of the Soultz reservoir derived from wellbore imaging and microseismic monitoring [Sausse et al., 2010], with important structures identified along GPK2.

volume, which is interpreted as change of effective stress. To explain these large stress changes, they again refer to large-scale aseismic motions.

At least for the major stimulations between 2000 and 2004 the respective largest magnitude event occurred after shut-in of the well. Schindler et al. [2008] analyzed the average amplitude recorded during and after stimulation as a proxy of earthquake energy. They found a general up to two-fold increase of amplitudes for the post-injection period. The observation of the largest event after shut-in is common to many sites, e.g. Basel [Häring et al., 2008] and Landau [Bönnemann et al., 2010]. Few models are proposed to explain the effect [Baisch et al., 2006, 2010; Goertz-Allmann and Wiemer, 2013], but these are not sufficient to explain other observations, as is discussed in Chapter 6.

The spreading of the microseismic clouds were used to infer the hydraulic diffusivity of the reservoir rock, based on the assumption of diffusion of pore fluid pressure following Darcy's law. The seismicity based reservoir characterization (SBRC) approach was developed by Shapiro et al. [1999] and applied to the stimulation of GPK1 in 1993, and by Delépine et al. [2004] to the stimulation of GPK2 in 2000. The NW-SE elongation of the microseismic cloud was solely interpreted in terms of anisotropic permeability, and Shapiro et al. [1999] obtained the permeability tensor in a principle coordinate system as:

$$\mathbf{k} = \text{diag}(0.7; 1.9; 5.2) \times 10^{-17} \text{ m}^2. \quad (3.3)$$

This is in approximate agreement with the value of matrix permeability as determined from hydraulic modelling of the convection cell in Soultz [Kohl et al., 2000]. However, the permeability of the fractured zones were estimated by the modelling to be about three orders of magnitude larger than this [Kohl et al., 2000]. The apparent diffusivity exhibited by the microseismic event propagation therefore appears to be determined by the matrix permeability, rather than by the permeability of the fractured zones that act as primary fluid conduit. Hence, the validity of the SBRC approach in a fractured rock mass is disputed [Cornet, 2000]. The elongation of the microseismic cloud could for example be partially explained by the anisotropic far-field stresses in connection with a poroelastic coupling [Schoenball et al., 2010], and the assumption of pore pressure diffusion following Darcy's law is not valid in a fractured medium [Kohl et al., 1997].



# 4

---

## THE ROLE OF TRIGGERING BY STATIC STRESS TRANSFER DURING GEOTHERMAL RESERVOIR STIMULATION

---

This chapter is published in *Journal of Geophysical Research*, 117, B09307, doi:10.1029/2012JB009304.

### ABSTRACT

Understanding of induced seismicity during stimulation and production of geothermal reservoirs is a key aspect towards future large-scale application of deep geothermal energy. During creation of an Enhanced Geothermal System massive fluid injections are conducted to induce shear events which generate reservoir permeability. At the European research project at Soultz-sous-Forêts (Alsace, France) several well stimulation experiments have been conducted and a unique dataset has been assembled. In this study we analyze coseismic static stress transfer due to induced seismicity during a stimulation. For this purpose we developed an efficient method to calculate coseismic static stress changes from an elliptical slip distribution on a circular fracture using superposition of rectangular sources, which enables us to apply an analytical solution for fast computation. This method is applied on a dataset of 715 focal mechanisms derived from seismic recordings of the stimulation of the well GPK2 to calculate temporal evolution of static stress transfer. We find that the structure of coseismic stress changes can be divided into three parts: a quiet zone where no spreading of seismicity occurs, an active zone within the created reservoir with ongoing fracturing and a process zone where the growth of the reservoir occurs. Static stress changes in the active zone are of the order of  $\pm 1 \text{ MPa}$ , but may exceed this value considerably on a local scale. Analysis of stress changes from a cluster of events that occurred after shut-in lets us conclude, that triggering by coseismic static stress changes is possible for some events.

### 4.1 INTRODUCTION

The phenomenon of fluid induced seismicity is widely observed and may impose barriers for future large scale operation of EGS plants

[Evans et al., 2012]. For the prediction of future reservoir performance, knowledge of the thermo-hydro-mechanical response of the geothermal reservoir to hydraulic stimulation and production is a key issue. In previous studies on the mechanisms of induced seismicity the focus was mainly on the role of the pore pressure perturbation or thermal stresses [Bruel, 2002; Shapiro et al., 2002; Kohl and Mégel, 2007]. Little attention was paid to the possible interaction of such events. However in the field of seismology of tectonic earthquakes, interaction of earthquakes has gained significant attention. Aftershock sequences for tectonic earthquakes could be described as induced by changes of static stress due to the dislocation by the main shock [e.g. King et al., 1994; Toda and Stein, 2003]. The basis for such modeling was laid by Okada [1992] who derived analytical expressions for the displacements in an elastic half space caused by dislocations on a fault plane. Based on these stress changes and e.g. a rate and state law for seismicity rates [Dieterich, 1994] aftershock sequences could be modeled successfully [Toda and Stein, 2003; Catalli et al., 2008]. Apart from modeling of aftershock sequences, migrating seismicity on large faults could be explained by interaction of events [e.g. Stein et al., 1997], where increases of stress arising at the edge of the slipping plane triggered failure at neighboring fault patches.

Orlecka-Sikora et al. [2009] analyzed coseismic static stress changes and interaction of induced seismicity in a Polish coal mine environment. They observed that about 60 % of events are located in areas where Coulomb stress changes encouraged failure and 50 % in areas where the stress perturbation by static stress transfer surpassed 0.01 MPa, a value which is a generally accepted threshold perturbation for triggering of natural earthquakes [Hardebeck et al., 1998; Prejean et al., 2004; Xiong et al., 2010]. While Orlecka-Sikora et al. [2009] and this study focus on triggering by static stress changes, it shall be noted that dynamic triggering by the passing wave train has also been observed [e.g. Felzer and Brodsky, 2006; Prejean et al., 2004].

Phillips et al. [2002] performed a multiplet analysis and relative relocation of events induced during a stimulation operation in 1993 at Soultz-sous-Forêts and five other geothermal and hydrocarbon sites. From high precision relative locations they concluded that slip induced changes of static stress migrate seismicity along larger fault planes at hydrocarbon sites and state that such slip-induced stress could cause systematic migration of seismicity also at Soultz. Dorbath et al. [2008] studied static stress changes due to the microseismic events of the stimulation of the well GPK2 in the year 2000, by approximating the microseismic cloud with one unique plane. Using this approach, they found a shift in the azimuth of the faults optimally oriented for failure in two different depth zones of the reservoir. This result is in agreement with the observation of a change of the orientation of the microseismic cloud produced by the later stimulation of the well GPK3 in 2003. However, their hypothesis that the

microseismic activity in the reservoir could be depicted by one single fault has not been validated.

In this paper we present 3D computations of change of static stress during the stimulation of the well GPK2 at the EGS site Soultz-sous-Forêts to analyze the mechanical interaction of induced events. For this analysis we use an extensive database of 715 derived focal mechanisms [Dorbath et al., 2009]. In order to find a computationally efficient way to approximate circular sources taking into account an elliptical slip distribution, we test various idealized fault plane geometries. We then compute the time evolution of static stress changes due to events in the Soultz reservoir during the stimulation of the well GPK2. This allows us to conclude that the stress perturbation of all microseismic events induced during stimulation cannot be depicted by one single fault, but varies strongly on a local scale. Analysis of a cluster of 12 events, which occurred at the edge of the stimulated volume, demonstrates the effectiveness of static stress triggering for the propagation of seismicity along faults.

#### 4.2 DATA DESCRIPTION

At the European deep geothermal research project at Soultz-sous-Forêts (Alsace, France) [Genter et al., 2010] four wells were drilled to 5 km depth in a horst structure within the granite basement of the Upper Rhine Graben. In order to develop an Enhanced Geothermal System (EGS) several well stimulations have been conducted in order to enhance the reservoir productivity [Dorbath et al., 2009]. These operations were accompanied by thousands of induced microseismic events. During the stimulation of the well GPK2 about  $25\,000\text{ m}^3$  of fresh water were injected with flow rates of  $30$  to  $50\text{l s}^{-1}$  over a duration of 6 days [Weidler et al., 2002]. The stimulation of GPK2 was seismically recorded by both a down-hole and a surface network of seismometers. About 14 000 events could be located by the down-hole network [Dyer, 2001], from which three stations with 4-component accelerometers at about 1500 m depth (i.e. at the top of the granitic basement) were used for analysis. The temporary surface network consisted of 14 stations, 6 with 3-component velocimeters and 8 with 1-component vertical velocimeters. For further details on the monitoring network we refer to Dorbath et al. [2009]. Our input data consists of 715 focal mechanisms of events induced during and immediately after the stimulation of GPK2 with magnitudes  $> 1$  [Dorbath et al., 2009], for which relatively good signal-to-noise ratio waveforms were obtained from both networks. The microseismic sequence used does not contain the largest events induced during the operation with magnitudes 2.6 and 2.7, respectively. They occurred long after shut-in when the temporary monitoring network was already removed from the field. The hypocenter locations were obtained using a mod-

ified version of HYPOINVERSE [Klein, 1978] and station corrections. Uncertainties are about 50 m in horizontal and 70 m in vertical directions. Event magnitudes,  $M_W$ , were calculated from the duration of the coda [Charléty et al., 2007]. To calibrate this duration magnitude, Charléty et al. [2007] determined the moment magnitude for several events with magnitudes in the range 0.7 – 2.9 using waveforms with good signal-to-noise ratio recorded during the stimulation of the well GPK3 in 2003. The seismic moment,  $M_0$ , was calculated from  $M_W$  using Kanamori [1977]:

$$M_W = \frac{\log M_0}{1.5} - 6.07. \quad (4.1)$$

Slip could then be derived from

$$M_0 = G S d, \quad (4.2)$$

where  $G$  is the shear modulus,  $S$  is the surface area of the fault plane and  $d$  is the average displacement. The ratio of displacement to surface area is determined by the stress drop  $\Delta\sigma$ . Following the relation of Eshelby [1957] for stress drop  $\Delta\sigma$  on a circular rupture of radius  $r$ ,

$$\Delta\sigma = \frac{7\pi G d}{16 r} = \frac{7\pi M_0}{16 r^3}, \quad (4.3)$$

the fault radius and the displacement can be determined using a stress drop value together with equation 4.2. Stress drops from fluid induced events have been analyzed for the injection experiments at the KTB project [Jost et al., 1998] and at the Basel Deep Heat Mining project [Goertz-Allmann et al., 2011]. For the Soultz reservoir, stress drops and source dimensions have been studied by Charléty et al. [2007]. In general agreement with the previously mentioned studies at KTB and Basel, Charléty et al. [2007] found the stress drop to vary between 0.1 MPa and 10 MPa. We use the previously mentioned studies as a basis for a statistically distributed value of  $\Delta\sigma$ . We use a constant log-mean value of 1 MPa for the following study; the influence of variable stress drop on the significance of the results is discussed below. The method to differentiate the fault plane and the auxiliary plane from the two nodal planes given by the focal mechanism is described in section 4.3. Figure 4.1 shows the events and their fault planes derived by the procedure above.

Elastic rock properties have been assumed in agreement with the previous study by Dorbath et al. [2008], i.e. a shear modulus of  $G = 32$  GPa and a Poisson's ratio  $\nu = 0.25$ . The coefficient of friction is assumed to be 0.8, which is the lower estimate of the two models developed by Cornet et al. [2007]. A comparison of density of fracture normals in the three wells GPK2-4 obtained from UBI wellbore

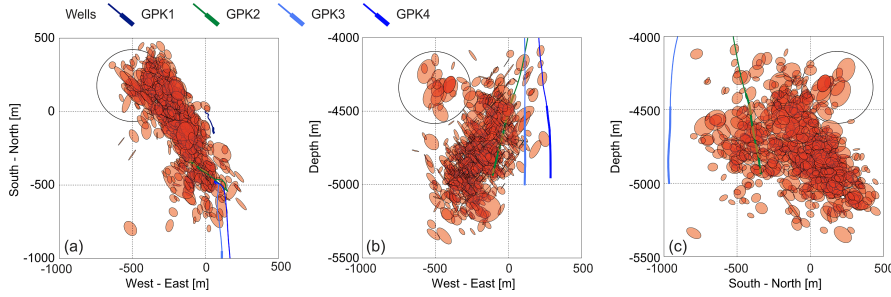


Figure 4.1: (a) Map view and (b, c) depth views of the fault planes obtained from focal mechanisms. The circles mark a cluster of events discussed in section 4.5.3.

logging with those of the fracture planes from focal mechanisms is given in Figure 4.2a-c. These plots show two major fracture families dominating the reservoir (average orientations are strike N180°E, dip 80° and strike N335°E, dip 80°, respectively). Note the slight counter-clockwise rotation of average azimuth with depth (Figures 4.2a vs 4.2c). The fracture families are also evident in the fault planes derived from the focal mechanisms (Figure 4.2d). The focal mechanisms are in better agreement with the deeper fractures, which consistent with the greater depth of the focal mechanisms. The focal mechanisms have generally lower dip angles than the fractures identified in the wellbore image logs. Elastic rock properties have been assumed in agreement with the previous study by Dorbath et al. [2008], i.e. a shear modulus of  $G = 32$  GPa and a Poisson's ratio  $\nu = 0.25$ . The coefficient of friction is assumed to be 0.8, which is the lower estimate of the two models developed by Cornet et al. [2007]. A comparison of density of fracture normals in the three wells GPK2-4 obtained from UBI wellbore logging with those of the fracture planes from focal mechanisms is given in Figure 4.2a-c. These plots show two major fracture families dominating the reservoir (average orientations are strike N180°E, dip 80° and strike N335°E, dip 80°, respectively). Note the slight counter-clockwise rotation of average azimuth with depth (Figures 4.2a vs 4.2c). The fracture families are also evident in the fault planes derived from the focal mechanisms (Figure 4.2d). The focal mechanisms are in better agreement with the deeper fractures, which consistent with the greater depth of the focal mechanisms. The focal mechanisms have generally lower dip angles than the fractures identified in the wellbore image logs.

#### 4.3 METHOD

The displacement field in a homogeneous elastic half space due to a dislocation on a rectangular fault has been analytically derived by Okada [1992]. We use a code based on the software EDCMP [Wang et al., 2003] to calculate the displacement field in the reservoir as it

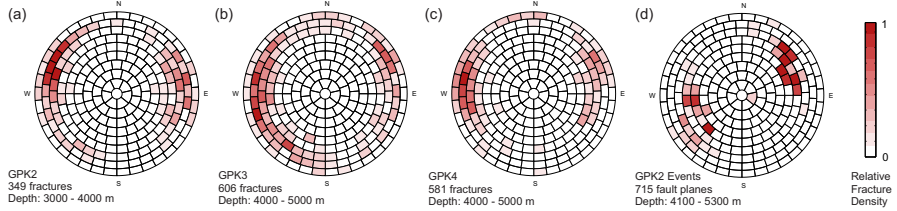


Figure 4.2: Distribution of fracture plane normal densities in a lower hemisphere projection, where a point in the center indicates a horizontal fracture while a point near the outer edge is a vertical fracture with dip direction as indicated on the edge. (a-c) show fractures obtained from UBI logs of GPK<sub>2</sub>, GPK<sub>3</sub> and GPK<sub>4</sub>, while (d) shows the focal mechanisms of the stimulation of GPK<sub>2</sub>. The color shows the relative density of fractures where each segment is of equal solid angle [after Meller et al., 2012].

evolves through subsequent microseismic events during the stimulation. Having obtained the displacement field  $u$  from Okada's solutions, the strain tensor  $\epsilon$  is readily obtained from

$$\epsilon_{ij} = \frac{1}{2} \left( \frac{\partial u_i}{\partial x_j} + \frac{\partial u_j}{\partial x_i} \right). \quad (4.4)$$

We assume a linear elastic medium by applying Hooke's law to obtain the change of the stress tensor from the strain tensor. To express the effect of changes to the stress tensor on the occurrence of failure by a single quantity, the concept of Coulomb failure stress is commonly applied. Following this concept, failure occurs if the Coulomb stress  $\sigma_c$  exceeds a critical value [King et al., 1994] given by

$$\sigma_c = |\tau| - \mu(\sigma - p), \quad (4.5)$$

where  $\tau$  is the shear stress on the plane in consideration,  $\sigma$  is the corresponding normal stress,  $\mu$  is the coefficient of static friction and  $p$  is the pore fluid pressure. In this paper our focus is on stress changes due to dislocations, so we do not consider changes of pore fluid pressure. Furthermore we neglect any poroelastic interaction of stress and pore fluid pressure, which would introduce minor transient effects. Finally we obtain for changes of Coulomb failure stress

$$\Delta CFS = \Delta \tau - \mu \Delta \sigma, \quad (4.6)$$

where  $\Delta \tau$  is the change of the absolute value of shear stress and  $\Delta \sigma$  is the change of normal stress on the fault plane considered. In this concept a positive value of  $\Delta CFS$  means that the point considered is driven towards failure whereas for a negative  $\Delta CFS$  stress is released and consequently failure is hindered.

For the computation of coseismic stress changes the tectonic stress field and its orientation is not to be considered, and we may arbitrarily choose the stress field prior to stimulation to be zero. However to

obtain the orientation of optimally oriented fault planes to compute  $\Delta\text{CFS}$  we use the linear stress profiles given by Cornet et al. [2007], the orientation of  $S_{H,\text{max}}$  is assumed to be N170°. The computation of  $\Delta\text{CFS}$  on fault planes optimally oriented for failure is described in detail in King et al. [1994]. If not mentioned otherwise computations of  $\Delta\text{CFS}$  are for optimally oriented failure planes. As noted above, computations presented here neither consider changes of pore fluid pressure nor thermal stresses. Obviously, because it is based on seismicity, the  $\Delta\text{CFS}$  does not consider either stress changes induced by aseismic slip [e.g. Bourouis and Bernard, 2007; Calo et al., 2011], for which no reliable data exists.

To discriminate the two nodal planes given by the focal mechanism between the fault plane and the auxiliary plane, we apply the Coulomb criterion. The critical pore fluid pressure  $p_c$  needed to rupture a fault plane is obtained from equation 4.5:

$$p_c = \sigma - \frac{\tau}{\mu}. \quad (4.7)$$

$\sigma$  and  $\tau$  are obtained from the orientation of the planes and the tectonic stress field. The critical pore pressure is calculated for both nodal planes; the plane where  $p_c$  is lower is assumed to be the fault plane.

#### 4.4 PARTITIONING OF SOURCE ZONES

In geothermal reservoirs with microseismicity of magnitudes of up to  $M_W = 3$  fault planes with more or less circular shapes could be expected, which is what we assume in the following. Furthermore the slip must reduce to zero at the boundary of the source area to assure continuity and avoid stress singularities. The kinematics and deduced slip distribution of such circular sources were described in Madariaga [1976]. The analytical solutions for computation of displacements due to dislocations by Okada [1992] are for point sources and rectangular sources with constant slip. Due to the linear nature of the stress perturbations, the perturbations by several sources can be added linearly to obtain the cumulative stress perturbation. A widely used approximation for vanishing displacement at the fault boundary is by tapering slip by the superposition of several slip rectangles of similar aspect ratio. As will be shown in the following, this method is not suitable for modeling circular fault planes. To approximate the behavior of circular faults with vanishing displacement at their boundaries, the microseismicity sources were partitioned into superimposed rectangles of varying aspect ratio as shown in Figure 4.3a. Each rectangle is given the same slip which, summed up over all rectangles, gives the seismic moment of the recorded event. A slip distribution very similar to the elliptical one derived by Madariaga [1976] is obtained by this approximation scheme (Figure 4.3b).

The effect on the change of Coulomb failure stress using several superimposed rectangles instead of square sources is analyzed in Figure 4.4. Here we show the resulting 3D Coulomb failure stress change by one seismic event represented by different slip distributions. The event source is implemented as one square of constant slip, four squares of different sizes representing the tapering used in many studies, 3 rectangles, 10 rectangles and 30 rectangles, respectively. For reference the stress change due to a slip distribution according to the shape of Madariaga's model is implemented using a grid of  $40 \times 40$  source tiles (i.e. 1600 sources) with their respective slip. To visualize the  $\Delta\text{CFS}$  perturbation in 3D space isosurfaces of  $\pm 1 \text{ MPa}$  are plotted in Figure 4.4 along with the slip distribution. For the one square source the isosurfaces occupy only a small volume concentrated on the tips of the shear displacement. For the case of four squares superimposed on the center of the fault we obtain a stress perturbation with tips of the isosurface on the very outer edge of the source. However, comparing with Madariaga's source shows that the stress tip is pointing to the outer edge at the middle of the fault plane. This behavior is much better approximated by three rectangles of different aspect ratios (Figure 4.4d). Going further to ten rectangles gives very smooth stress perturbations close to that of the Madariaga's source. By increasing the number of rectangles further to 30 only a marginal improvement of the approximation is achieved. However, a feature that cannot be obtained by the approximation by rectangles are the small lobes of opposite stress perturbation close to the fault plane. To sum up, using three rectangles to represent the stress perturbation by a circular Madariaga source yields a much better approximation than using four squares. Additionally it provides faster computation as the effort for calculating  $\Delta\text{CFS}$  increases linearly with the number of source rectangles used. At about ten rectangles a reasonable compromise between computational efficiency and accuracy is reached. Thus, in the following this source model is used.

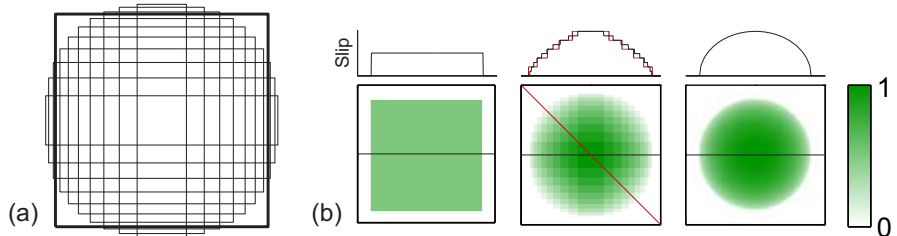


Figure 4.3: (a) Partitioning of one square source (bold) into 10 rectangles (thin). (b) Slip distribution for one square source, approximation by 10 rectangles and the Madariaga source.

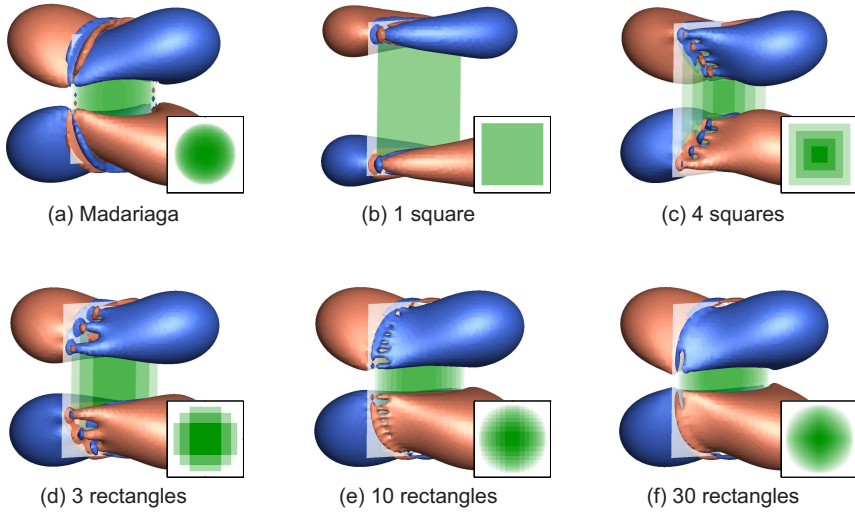


Figure 4.4:  $\Delta$ CFS isosurfaces of +1 MPa (red) and -1 MPa (blue) obtained from different slip distributions (green and insets) for a faulting mechanism with equal seismic moment corresponding to 1 mm slip on a  $10 \times 10$  m square fault.

#### 4.5 $\Delta$ CFS DURING STIMULATION OF GPK2

In order to study the temporal evolution of the  $\Delta$ CFS, the dataset is split into 14 subsets analogous to Calo et al. [2011]. They are depicted along with injection rate and wellhead pressure and number of events per hour in Figure 4.5. Figure 4.6 shows the temporal evolution of the cumulative  $\Delta$ CFS on a map view at a depth of 4700 m for each subset. This depth section is about the vertical center of the stimulated volume. During the first nine subsets the cloud of seismic events spreads continuously. The  $\Delta$ CFS perturbation is dominated by small events that create a pseudo-random pattern of areas with positive and negative  $\Delta$ CFS. The stress perturbations reach values on the order of 1 MPa, both positive (encouraging failure) and negative (hindering failure), with strong local variations. Areas of strongly positive  $\Delta$ CFS are found neighboring to areas of negative  $\Delta$ CFS, especially in the central portion of the stimulated region. Subset 10 includes the biggest induced event ( $M_W = 2.5$ ) that dominates a large area with negative  $\Delta$ CFS. In the following subsets, a number of relatively large events occur, producing mainly negative  $\Delta$ CFS areas in this depth section. In the far field of the reservoir, a large-scale area with negative  $\Delta$ CFS prevails over the whole monitored period with stress release of less than 100 kPa. No large areas with positive  $\Delta$ CFS are found, it is thus unlikely that slippage of large surface areas is triggered by static stress transfer. On the contrary, it can be speculated that slippage of large surfaces is hindered by stress release on some patches of potential large structures which would lead to segmentation of slip.

In a previous study of static stress transfer at Soultz Dorbath et al. [2008] assumed that the stress perturbation due to the thousands of microseismic events induced during the stimulation was equal to that of one large event whose seismic moment was the sum of that of all the microseismic events. The orientation and size of that one hypothetical fault plane was chosen to coincide with the geometry of the observed microseismic activity. We compare the distribution of the  $\Delta\text{CFS}$  obtained from one source according to Dorbath et al. [2008] with the computation of the  $\Delta\text{CFS}$  according to our method taking into account 715 located events with  $M_W > 1.0$  (Figure 4.7a). In contrast to Dorbath et al. [2008] we apply the source model presented in section 4.4 and partition the unique source into 10 rectangles (Figure 4.4e), while Dorbath et al. [2008] used a tapering method shown in Figure 4.4c. From comparison of Figures 4.7a and 4.7b it is obvious that the approximation to use one single source to represent the stress perturbation due to dislocation is not valid entirely. Both computations deliver fundamentally different results, in particular the central region of the stimulation is essentially free of high stress perturbations whereas many high stress perturbations and undulations result from the detailed computation in this region of the reservoir. However, looking at the far field of coseismic  $\Delta\text{CFS}$  both results are very much comparable, yielding a large-scale patterns of negative  $\Delta\text{CFS}$  along the seismic cloud and of positive  $\Delta\text{CFS}$  at the edges of the seismic cloud. From these observations and with respect to the temporal evolution of the  $\Delta\text{CFS}$  (Figure 4.6) we can derive a schematic on the development of the perturbation of  $\Delta\text{CFS}$  with three distinct zones (Figure 4.7c). These are an active zone within the seismic cloud with large variations of  $\Delta\text{CFS}$  on a local scale, where most of the induced events occur. Furthermore there is a process zone at the tips of the seismic cloud with positive  $\Delta\text{CFS}$  encouraging failure, where growth of the microseismic cloud occurs and finally a quiet zone parallel to the cloud where negative  $\Delta\text{CFS}$  predominates and failure is discouraged. These three distinct zones can also be observed in vertical direction, with a developed process zone also at the top and bottom of the stimulated volume.

#### 4.5.1 Sensitivity to Limiting Magnitude

In Figure 4.8, we compare  $\Delta\text{CFS}$  down to different magnitude values contained in the catalog of the focal mechanisms varying from  $M_W = 2.0$  down to  $M_W = 1.0$  at a depth of 4700 m. Also indicated in each subfigure of Figure 4.8 is the number of events up to a given magnitude and the cumulative seismic moment compared to the total seismic moment recorded during the experiment. For events down to  $M_W = 1.6$  about 60 % of the cumulative seismic moment is included in the perturbation of  $\Delta\text{CFS}$ . The  $\Delta\text{CFS}$  perturbation of the largest

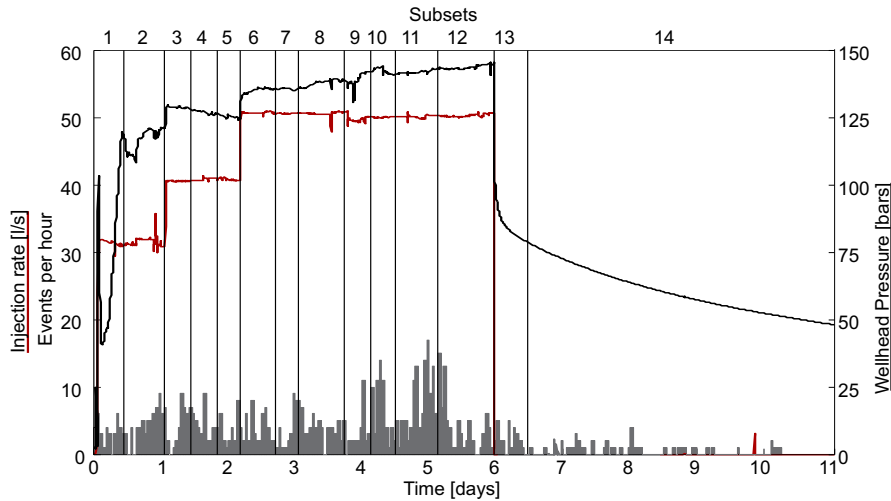


Figure 4.5: Injection rate, wellhead pressure for the hydraulic stimulation of GPK2 (June/July 2000). Dashed vertical lines mark the times for the 14 snapshots in Figure 4.6. The bars indicate the event rate per hour ( $M_W > 1$ ) during the experiment.

recorded event with magnitude 2.5 is remarkable. Its contribution to  $\Delta$ CFS dominates a region of several hundred meters radius (bottom of subplots in Figure 4.8). Figure 4.9 shows the mean of the relative variation of  $\Delta$ CFS for a reduced catalog down to  $M_{W,\text{limit}}$  compared to the full catalog down to  $M_W = 1.0$  after

$$\delta = \frac{1}{n} \sum_{n=0}^N \left| \frac{\Delta\text{CFS}_{1.0} - \Delta\text{CFS}_{M_{W,\text{limit}}}}{\Delta\text{CFS}_{1.0}} \right|, \quad (4.8)$$

with  $N$  the number of points where  $\Delta$ CFS is calculated. The difference of computed values of  $\Delta$ CFS reduces linearly with magnitudes contained in the catalog. Small events therefore contribute a significant amount of static stress transfer. Small events cause a smaller stress perturbation, but there are a greater number of them. The significant effect of small earthquakes for static stress transfer is in full agreement with the study by Helmstetter et al. [2005] on the triggering potential of small earthquakes. They find that for a set of events on a fractal fracture network of dimension  $D$  with a Gutenberg-Richter law with  $b \approx D/2$  [Aki, 1981; Chen et al., 2006] small events are as important for triggering as large events. However, including even smaller events will contribute to the  $\Delta$ CFS perturbation only very locally, on a scale where errors in location dominate any possible conclusion.

#### 4.5.2 Triggering Potential and Stress Drop

In this section we discuss the distribution of  $\Delta$ CFS values obtained from a constant stress drop and its implication for triggering. We

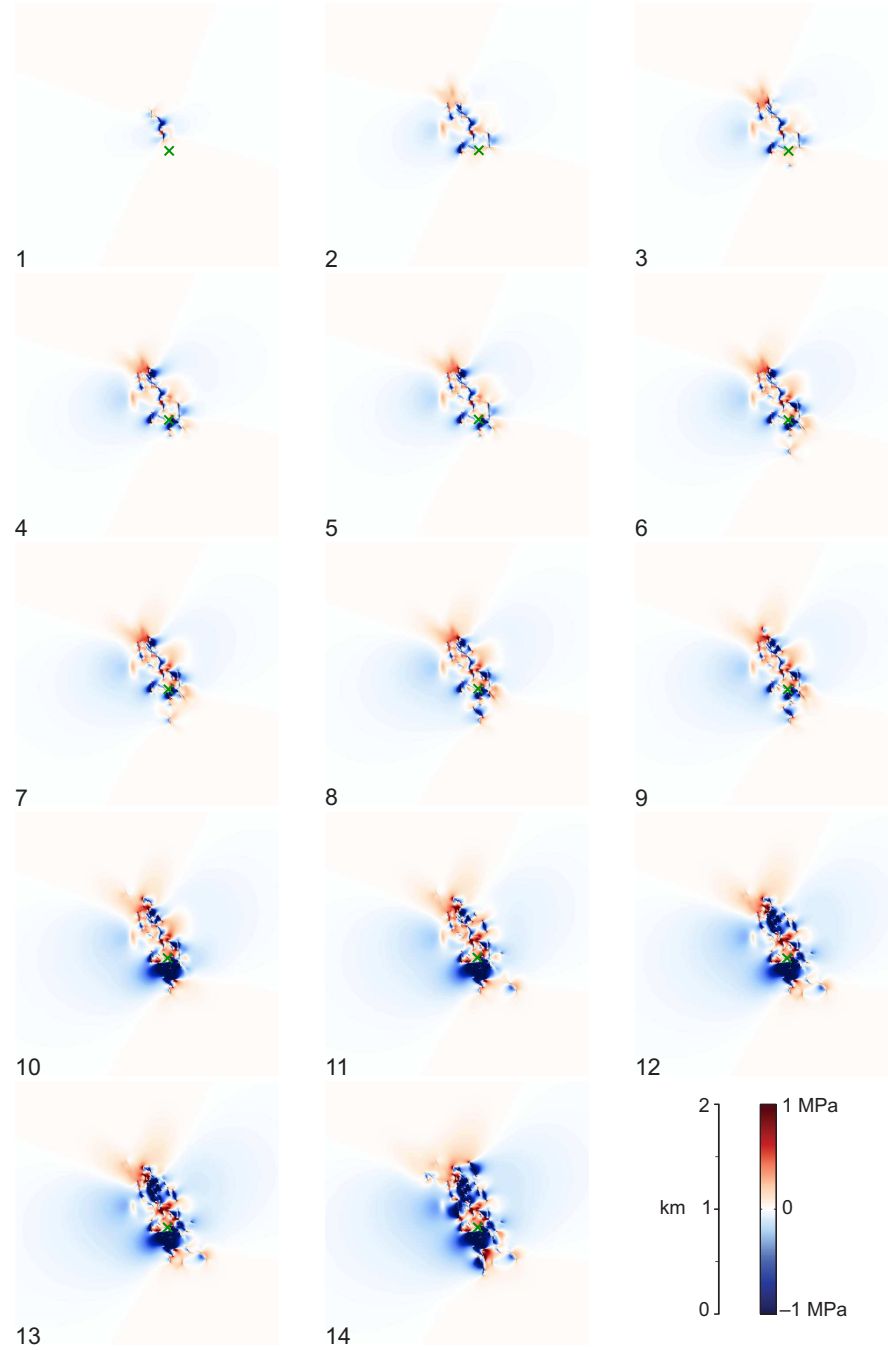


Figure 4.6: Temporal evolution of cumulative  $\Delta CFS$  during stimulation of the well GPK2 after each subset defined in Figure 4.5. Map view of the Soultz reservoir at 4700 m depth, the green cross marks the injection point of GPK2. Blue areas are where failure is discouraged ( $\Delta CFS < 0$ ), red areas are where failure is encouraged ( $\Delta CFS > 0$ ), with respect to optimal oriented fault planes.

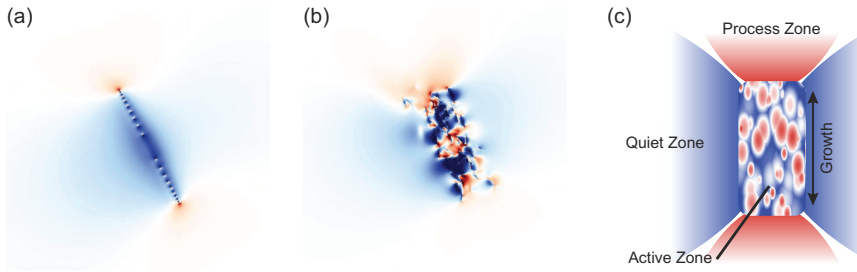


Figure 4.7:  $\Delta$ CFS for optimal oriented fault planes in the Soultz reservoir (a) for one source fault representative of all events [after Dorbath et al., 2008] and (b) for the full catalog of 715 source events, same color scale as in Figure 4.6. Figure (c) is a schematic of the time-evolving coseismic  $\Delta$ CFS perturbation in the reservoir.

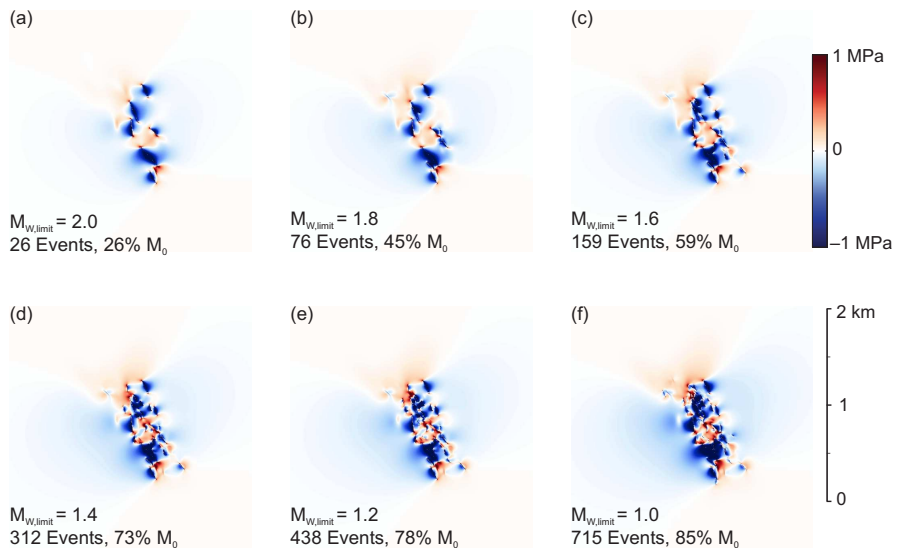


Figure 4.8: Map view of  $\Delta$ CFS at  $z = 4700$  m for a subset of the full catalog, where the magnitude  $M_{W,\text{limit}}$  down to which events are contained in the catalog varies from subfigures (a-f). The number of events of each subset and the cumulative seismic moment relative to the total recorded moment is given in each subfigure. Optimal oriented fault planes are assumed.

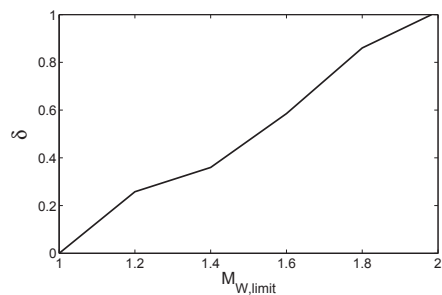


Figure 4.9: Relative error of  $\Delta$ CFS for a reduced catalog down to  $M_{W,\text{limit}}$  compared to the full catalog down to  $M_W = 1.0$  after equation 4.8.

study the effect of varying stress drop and make some preliminary conclusions. Then we analyze the distribution of  $\Delta\text{CFS}$  on the hypocenters of the microseismic events to investigate how the occurrence of microseismicity is influenced by  $\Delta\text{CFS}$ . For a given event we compute the cumulative  $\Delta\text{CFS}$  of all previous events at its located hypocenter. We do this for each event in our dataset and analyze two scenarios. In the first we compute  $\Delta\text{CFS}$  for optimally oriented fault planes, as in the calculations before. In the second calculation we compute  $\Delta\text{CFS}$  at the hypocenter using the orientation of the fault plane of the given event, to derive normal and shear stresses and finally the value of  $\Delta\text{CFS}$  (Figure 4.10a). For both fracture orientations we obtain almost a normal distribution centered on  $\Delta\text{CFS} = 0$ .

All results presented above have been acquired using the assumption of a constant stress drop of 1 MPa. For the stimulation of the granitic reservoir at Basel, stress drops were quantitatively analyzed by Goertz-Allmann et al. [2011]. They found the stress drop to vary over two orders of magnitude around a mean value of 2.3 MPa. In order to analyze the impact of our assumption on stress drop, we compute  $\Delta\text{CFS}$  using random stress drops for each event. The stress drops are chosen using a log-normal distribution to resemble the distribution of stress drop values obtained by Goertz-Allmann et al. [2011], with a log-mean of  $\Delta\sigma = 1$  MPa and a log-standard deviation of 0.5. The computation is repeated 10 times using different random number seeds (Figure 4.10b). We obtain relatively large variations of values of  $\Delta\text{CFS}$  for each single fracture. However, the overall behavior of  $\Delta\text{CFS}$  is statistically the same for different sets of stress drop including the constant stress drop of 1 MPa. We therefore conclude that the approximation of constant stress drop is acceptable for our analysis. Overall we find that 61 % and 58 % of the events occur in areas of positive  $\Delta\text{CFS}$  for optimal and the actual orientation of faults, respectively. A closer look at the distributions on  $\Delta\text{CFS}$  reveals that optimal orientation yields more negative values, especially below  $-0.5$  MPa, whereas the actual fracture orientation yields more positive values above 0.5 MPa. The variation observed is interpreted as a dependency of the triggering potential on the relative fracture orientations. When calculating the stress transfer for similarly aligned fractures, e.g. actual fracture families, constructive superposition of stress transfer is more likely than for dissimilar fracture orientations, e.g. the optimal orientation given by the stress field. Therefore similarly aligned fractures are more efficient at triggering than randomly oriented fractures.

#### 4.5.3 Triggering: An Example

For further analysis of potential triggering of seismicity by static stress transfer we analyze a cluster of relatively large events ( $1 <$

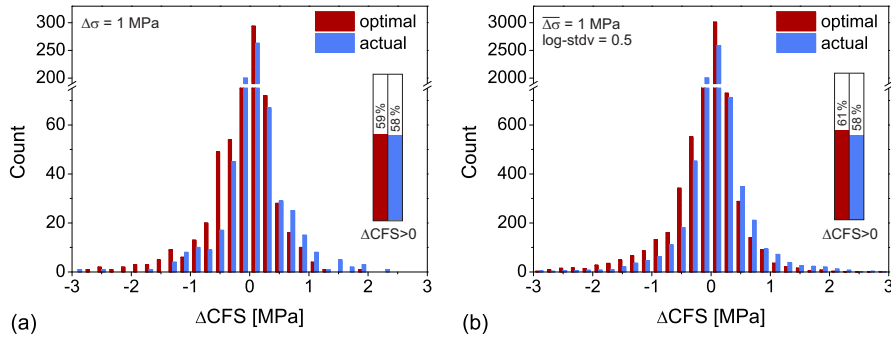


Figure 4.10: Distribution of  $\Delta$ CFS at the hypocenters for fault planes optimally oriented for failure (red) and for the actual orientations of fault planes (blue). Stress drop is (a) constant 1 MPa and (b) log-normal distributed about 1 MPa using 10 runs with different random seeds. Note the break in the y axis.

$M_W < 2.2$ ) that occurred after shut-in during a period of four days, when the general seismic activity already declined. The cluster is located at the top of the northwestern edge of the stimulated volume (Figure 4.1). It was noticed by Cuenot et al. [2008] for its large ratio of high-magnitude events to low-magnitude events and its detached location at the edge of the reservoir. Inter-event times range from six minutes to more than one day, so dynamic triggering can be ruled out. Twelve focal mechanisms from this cluster are contained in our dataset. All approximately share the same focal mechanism (Figure 4.11a). Hence it is likely, that each event ruptured a different segment of the same large scale structure. This structure coincides very well with a major fault structure named VSP-GPK1-3490 and GPK3-FZ4770 from the 3D geological model by Sausse et al. [2010], identified from a VSP study and image logs of the wells. This structure is known to hydraulically connect the wells GPK1, GPK2 and GPK3 and is probably responsible for the good hydraulic communication of these wells as revealed by tracer tests [Sanjuan et al., 2006]. Under the assumption of a fault plane common to all events of the cluster, we computed a mean focal plane (strike N135°, dip 70°) and projected all derived focal planes onto that plane, for computation of  $\Delta$ CFS. The distance of each focal plane to the mean plane was below 60 m, and within the location errors which underpins the assumption. The orientation of the mean plane was assumed for the computation of normal and shear stresses to obtain  $\Delta$ CFS. Figures 4.11b-e are snapshots of the 3D  $\Delta$ CFS with isosurfaces at 0.3 MPa. After the first three events (Figure 4.11b) a distinct pattern of matching jigsaw puzzle pieces of ruptured fault segments evolves. Each event appears to rupture a different slip patch, generating regions of positive  $\Delta$ CFS at its edge, which in turn propagates shearing along the fault zone by triggering the next event. Rupture propagation by slippage of neighboring slip patch has been already observed by Phillips et al. [2002]

on a reservoir scale. Due to the spatial proximity and the shared orientation of slip patches on a fault zone, static stress transfer is very effective. Rupture propagation is maintained during the whole sequence, with some areas being ruptured more than once.

Assessing the role of triggering by static stress transfer versus the role of pore pressure increases for the propagation of the cluster is very difficult. The cluster occurred about 900 m away from the open hole section of GPK2. The cluster of events could be associated with a large-scale fault structure with high transmissivity which is unlikely to allow high pore pressure build-up. Additionally, this cluster occurred after shut-in of the well and beyond the previous front of microseismic events (cf. Figure 4.1). Neither a reliable model for the propagation of pore pressure, especially after the shut-in of the well nor measurements of pressure away from the injection well exist. However, it is plausible that pore pressure still increased at the clusters location, also after shut-in [McClure and Horne, 2012; Baisch et al., 2010]. At the well GPK1, at a distance of about 1400 m to the open hole section of GPK2, pressure was monitored but no response could be recorded during stimulation. During a later stimulation of GPK3 (ca. 600 m away from GPK2) in 2003 the maximum pressure response measured in GPK2 was about 4 MPa before the dual stimulation with pumping in GPK2 began [Dorbath et al., 2009]. At that point seismicity progressed from GPK3 to beyond GPK2 and through a volume already stimulated during the stimulation of GPK2 in 2000. Following these observations the pore pressure at the cluster is certainly well below 4 MPa and probably below 2 MPa with a small pressure gradient. Thus, the static stress transfer contributes a considerable amount to the overall perturbation of stress, at least at the edges of individual slipping patches.

#### 4.6 DISCUSSION

From the seismic recordings of the stimulation more than 14 000 events could be located, but only from 715 events focal mechanism could be derived due to their signal-to-noise ratio. It is therefore important to note that potentially some fracture families did not generate large enough events, and their focal mechanisms are not represented in our study.

The analysis is based on the assumption of an elliptical slip distribution on a penny-shaped crack given by the Madariaga [1976] model. Estimations of slip distribution and actual shape of a sheared crack cannot be obtained from fluid induced seismicity due to their low magnitudes. The methodology applied allows calculation of arbitrary geometries. It can be speculated that the slipping areas are bounded by locked portions on a fault surface, leading to fragmentation of slip with temporal and spatial clustering of events. Slippage

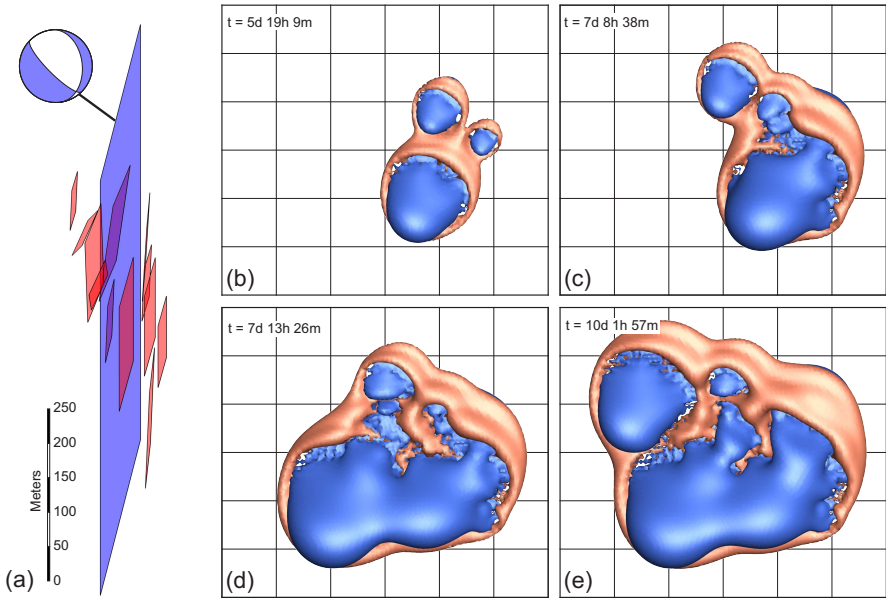


Figure 4.11: Cluster of 12 events that occurred during four days after shut-in. (a) Determined focal planes (red) and a mean fault plane (blue) on which the focal planes were projected. (b) Isosurfaces of  $+0.3$  MPa (red) and  $-0.3$  MPa (blue) for different times (given relative to the beginning of injection) during the sequence after 3, 6, 8 and all 12 events, respectively.

might also be stopped at intersections with other cracks, leading to angular areas of slippage.

Uncertainties of location and stress drop of the events are of large importance. As rupture dimensions ( $\approx 150$  m) are in the order of the location error ( $\approx 50$  m) and stress drops generally vary over two orders of magnitude great care must be taken on the interpretation of the results. We therefore analyze the  $\Delta CFS$  values in a statistical sense to confirm the robustness of the results. For varying stress drop this is given by the trade-off between small slipping areas with large slip, and large slipping areas with small slip given a certain moment magnitude. The first yields higher stress perturbations with smaller perturbed volume while the latter yields larger volumes with a smaller stress perturbation. These competing mechanisms equalize each other out within certain limits. It has been shown both, statistically and by an example, that triggering by static stress transfer is possible also in the environment of hydraulic stimulations. Also, if a slip patch is at the verge of failure e.g. by a perturbation of stress by pore fluid pressure increase, static stress transfer might deliver the last bit of stress perturbation necessary for rupture. Due to the large local scattering of the static stress transfer we cannot predict the growth of the seismic cloud due to triggering.

Above we show that triggering by static stress transfer is of little importance in a volumetric reservoir but it can be quite efficient if

the seismic response is confined to single large scale structures. The latter is exemplified on a cluster of events within the Soultz reservoir. However it is still under debate whether EGS reservoirs are dominated by single large scale structures or by a volumetric network of fractures. In general, the locations and focal mechanisms in our dataset of the stimulation of GPK2 suggest that the reservoir created by the stimulation is volumetric in structure rather than dominated by one or two major structures. This is supported by the relocations with small location errors, furthermore the focal mechanisms show distinct families of fractures which are distributed over the whole reservoir volume. Specifically, there are fracture families distributed over the whole seismic cloud with fault plane orientations almost perpendicular to the major axis of the seismic ellipsoid (see Figure 4.1). Furthermore, the b-value of 1.23 obtained by Dorbath et al. [2009] indicates a volumetric fracture network with a fractal dimension  $D > 2$ , whereas stimulations of GPK3 and GPK4 have b-values indicating to fracture networks of fractal dimension  $D \approx 2$  using the relation of b-value and fractal dimension of a fracture network by Aki [1981]. We therefore regard the reservoir created by the stimulation of GPK2 as volumetric as suggested by the locations and orientation of the focal mechanisms. On the other hand, due to inevitable location errors, events occurring on a plane will be apparently located in a volume rather than at their actual position on the plane. Hence, our method tends to underestimate the stress interaction.

Static stress transfer after seismic events was incorporated in several numerical codes simulating fracture of fault segments by elevated pore pressure. Usually slip patches are considered in different kinds of geomechanical simulations and eventually are brought to failure. Upon failure stresses are redistributed to neighboring slip patches. To compute the displacement field and derive changes to the stress tensor arising from simulated slip, the codes e.g. by McClure and Horne [2012] and Yamashita [1998] use numerical and analytical methods, respectively. Baisch et al. [2010] used a generic stress redistribution pattern for stress release at the failing slip patch and stress increase in neighboring slip patches. A number of other codes incorporating static stress transfer are currently under development by the community. All of these simulators are able to propagate failure along larger fractures and, by adding of slip of subsequently failing slip patches, are able to predict event magnitudes. The latter two codes are also used to predict b-values. Our study has shown, that considering static stress transfer is a viable means to propagate shearing of individual segments over a large fault. However application of static stress transfer on a 3D fracture network may be difficult due to large local variations of the stress perturbation.

#### 4.7 CONCLUSIONS

We use a computationally efficient method to analytically compute coseismic changes of Coulomb failure stress due to dislocations in the volume of a reservoir. This method accounts for an elliptical slip distribution on a circular fracture. We applied this approach on a dataset of 715 focal mechanisms obtained from the stimulation of GPK2 in Soultz. Changes of Coulomb failure stress of the order of  $\pm 1$  MPa were obtained and showed strong local variations due to the great number of events. Due to these variations a statistical interpretation has to be applied, rather than a deterministic one. However, static stress changes develop a consistent pattern during the stimulation with an emerging process zone, an active zone and a quiet zone. We showed that the local stress perturbation by dislocations estimated from microseismicity induced by hydraulic stimulation cannot be depicted by one large source, except if our interest is in the far field zone of the reservoir, where  $\Delta\text{CFS}$  is more uniform. On the contrary, our analysis shows a fundamentally different distribution of the stress perturbation and much more internal structure when analyzed in high detail. The values of  $\Delta\text{CFS}$  at the event hypocenters just before the events show distribution about 0 MPa with about 3 % of events with  $\Delta\text{CFS} > 1$  MPa. In a volumetric reservoir  $\Delta\text{CFS}$  by dislocation is thus only a minor contribution to the whole stress perturbation induced by stimulation, compared to e.g. an increase of pore fluid pressure. The latter typically is in the order of a few MPa, even at larger distance from the stimulated wells [see Figure 6 in Dorbath et al., 2009]. The study by Langenbruch et al. [2011] supports this result by showing that induced seismicity can be described by a Poisson process, i.e. the events are not causally related to each other. However, inevitable relocation errors tend to bias these results towards underestimating stress interaction. If more events are located on a single plane, the possibility of constructive interference of  $\Delta\text{CFS}$  will increase. Additionally we showed the triggering potential of neighboring slip patches on a larger fault zone and conclude that in such cases static stress transfer may propagate rupture, as proposed by Phillips et al. [2002].

#### ACKNOWLEDGMENTS

The work was supported by the European Commission (FP7 project GEISER, grant agreement no. 241321) and by EnBW Energie Baden-Württemberg AG. Comments by Emmanuel Gaucher, Rebecca Harrington, Oliver Heidbach, Cornelius Langenbruch are greatly acknowledged. Especially, we express our appreciation to Mark McClure for his thorough review of the manuscript.



# 5

---

## THE PECULIAR SHUT-IN BEHAVIOR OF THE WELL GPK<sub>2</sub> AT SOULTZ-SOUS-FORÊTS

---

This chapter is published in CRC Transactions, 37, 217-220.

### ABSTRACT

A better understanding of induced seismicity occurring during the creation of an enhanced geothermal system is vital for future large scale application of geothermal power. Especially the occurrence of large magnitude events ( $M_W > 2.0$ ) after shut-in is lacking a comprehensive understanding. We analyze the stimulation of well GPK<sub>2</sub> at the Soultz-sous-Forêts (Alsace, France) pilot site with emphasis on the shut-in. We observe a sudden change in spatio-temporal evolution of seismicity starting with shut-in that cannot be explained by currently available approaches to explain the occurrence of post-shut-in seismicity. We relate these observations to structural geological features of the reservoir surrounding well GPK<sub>2</sub> such as large faults and the transition between two granite facies.

### 5.1 INTRODUCTION

The European deep geothermal research project at Soultz-sous-Forêts (Alsace, France) has been developed since 1987 [Genter et al., 2010]. The geothermal reservoir is situated in a horst structure within the granite basement of the Upper Rhine Graben. The four production and injection wells reach up to about 5 km depth into the crystalline basement which is covered by 1.4 km of Cenozoic and Mesozoic sediments. In order to develop an Enhanced Geothermal System (EGS) several well stimulations have been conducted to enhance the productivity of the reservoir [Dorbath et al., 2009]. These operations were accompanied by thousands of induced microseismic events. For the prediction of future reservoir performance, knowledge of the thermo-hydro-mechanical response of the geothermal reservoir to hydraulic stimulation and production is a key issue. The phenomenon of fluid induced seismicity is widely observed and may impose barriers for future large scale operation of EGS plants [Evans et al., 2012]. The continued occurrence of large events after either massive fluid injec-

tion or production is stopped has been observed at a number of sites such as Soultz [Dorbath et al., 2009], Berlín in El Salvador [Bommer et al., 2006], Basel [Häring et al., 2008] and Landau [Bönnemann et al., 2010]. The phenomenon has been puzzling science for several years. Few approaches exist that explain the observation by means of geometric spreading effects of the pressure perturbed volume [Baisch et al., 2006, 2010; Barth et al., 2013] or the variation of b-values with distance from the injection well [Goertz-Allmann et al., 2011]. While all these approaches certainly explain part of the observations, mechanical effects of shut-in on the reservoir are still poorly understood. We revisit the case of the GPK2 stimulation in 2000 and analyze the spatio-temporal behavior of seismicity after shut-in to identify possible mechanisms that have been overlooked so far.

## 5.2 STIMULATION OF GPK2

The shallow section of the well GPK2 (ca. 3500 m) was first stimulated in 1995 and 1996 by two massive fluid injections [Gérard et al., 1997]. After deepening of the well, the deep part of the well was stimulated by massive fluid injection of about 25 000 m<sup>3</sup> of fresh water with flow rates of 30 to 50 l s<sup>-1</sup> over a period of 6 days in June and July 2000 [Weidler et al., 2002]. The stimulation of GPK2 was seismically recorded by both a down-hole and a surface network of seismometers. During the stimulation more than 30 000 events were detected by the down-hole network of which about 14 000 could be located by Dyer [2001]. We use the seismicity catalog created by Dorbath et al. [2009]. From the down-hole network, data from three stations with 4-component accelerometers at about 1500 m depth (i.e. at the top of the granitic basement) were used in the creation of this catalog. The temporary surface network consisted of 14 stations, 6 with 3-component velocimeters and 8 with 1-component vertical velocimeters. For further details on the monitoring network we refer to Dorbath et al. [2009]. They obtained hypocenter locations using a modified version of HYPOINVERSE [Klein, 1978] and station corrections, uncertainties are about 50 m in horizontal and 70 m in vertical directions. Event magnitudes were calculated from the duration of the coda [Charléty et al., 2007]. To calibrate this duration magnitudes the moment magnitude was determined for several events with magnitudes in the range 0.7 – 2.9 using waveforms with good signal-to-noise ratio recorded during the stimulation of GPK3 in 2003 by [Charléty et al., 2007]. In total, locations and magnitudes of 7215 events were obtained by Dorbath et al. [2009]. The largest event recorded during stimulation reached magnitude 2.5. The microseismic sequence obtained from the surface network used does not contain the largest events induced during the operation with magnitudes 2.6 and 2.7, respectively. They

occurred after shut-in in mid-July and the temporary monitoring network was already removed from the field.

Figure 5.1 shows the hydraulic data of the stimulation operation as well as the seismic response of the reservoir. At a flow rate of  $30\text{ s}^{-1}$  wellhead pressure settled at about 12 MPa. After increasing injection rate to  $40\text{ s}^{-1}$  pressure increased only by one MPa before falling off again to 12.5 MPa. At the last stage of pumping at  $50\text{ s}^{-1}$  wellhead pressure increased again by about one MPa to 13.5 MPa and increased continuously to about 14.5 MPa just before shut-in of the well. The event rate throughout the fluid injection phase was on the order of 50 events per hour. Towards the end of each injection rate step it decreased and increased strongly once the injection rate and hence wellhead pressure increased. No obvious correlation of event rate and fluid flow rate is observed. After shut-in seismicity fell off very quickly within one day, showing a behavior describable by Omori's law [Langenbruch and Shapiro, 2010]. However seismic activity continued for several days at a constant level. No particular evolution of maximum magnitudes over time can be observed (Figure 5.1, middle). First magnitude  $M_W = 2.2$  events occur after only 12 hours of injection. The maximum magnitude event during injection of  $M_W = 2.5$  occurred after about four days of injection. The largest events of magnitude  $M_W = 2.6$  occurred only after 10 days after shut-in [Dorbat et al., 2009]. The r-t-plot of the seismicity (Figure 5.1, bottom) shows some very remarkable features. Already after few hours seismicity propagated more than 500 m away from the well. Until shut-in seismicity progressed only slightly further outward to maximum distances of about 1000 m. But after shut-in suddenly events occurred at a distance of more than 1500 m away from the open hole section of the well. This behavior is analyzed by Michelet [2002] using the SBRC approach of Shapiro et al. [1999]. That way she interprets the different spatio-temporal evolution in terms of hydraulic diffusivity. She finds the diffusivity during injection as  $D = 0.14 \text{ m}^2 \text{ s}^{-1}$ , whereas it is  $D = 0.30 \text{ m}^2 \text{ s}^{-1}$  after shut-in. As it is highly unlikely that hydraulic diffusivity changes just by the fact of shut-in this behavior cannot be due to the hydraulic properties of the reservoir rock, but must have some origin in a different mechanical behavior for the post-shut-in period versus the injection period.

Calo et al. [2011] discuss the change in the pattern of seismicity based on refined double-difference locations. Only for the post-shut-in period are they able to discern structures in the cloud of seismicity which clearly show a delineation of planar structures. In order to investigate the peculiar spatio-temporal evolution starting with shut-in of GPK2 we analyze the locations of seismicity. The high seismic activity section of the seismicity cloud has an ellipsoidal shape with the major axis extending about 1 km along a strike of N150°. The minor axis is roughly 400 m. In the following we operate in a coordinate system rotated clockwise by 30 degrees around the z-axis. In this coordi-

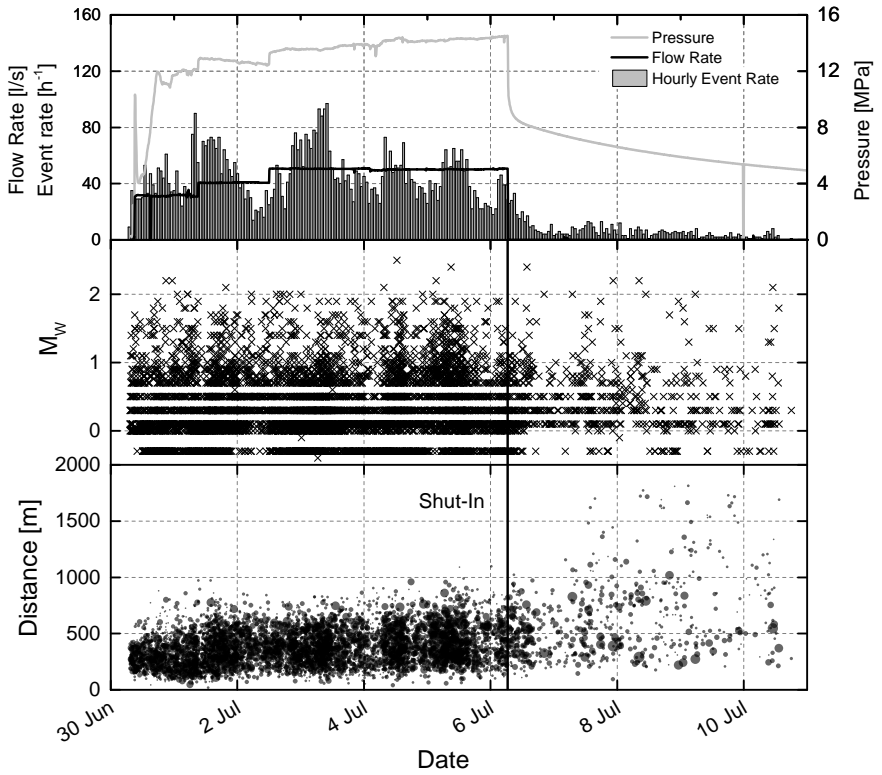


Figure 5.1: (top) Hydraulic data and seismic response in terms of hourly event rate during the stimulation. (middle) Magnitudes of events. (bottom) distance-time plot of the seismicity. Distance is calculated from the middle of the openhole section to the hypocenter. After shut-in a large increase of the maximum distances is observed.

nate system the major axis of the cloud stretches parallel to the  $y'$ -axis. We bin the events in moving windows of 100 events each, overlapping by 25 events on either side. For each bin we display the statistical distribution of seismicity along each coordinate by means of the median, the 25 and 75 percentiles and the total scatter of locations in individual boxplots (Figure 5.2). During the stimulation phases no obvious trend is seen in either of the coordinates, which means that the seismic cloud grows similarly in all directions. However, this changes considerably upon shut-in when clear trends become discernible on all three coordinate components. The  $x'$ -component does not show any systematic changes until one day after injection. However from that point it shows a drop of the median coordinate by about 150 m, dropping further later on. The  $y'$ -component shows a jump by 150 m two hours after shut-in. Then, after one more day median coordinates drop considerably to regions previously untouched. The vertical  $z'$ -component shows a remarkably steady decrease of depth starting two hours after shut-in, continuing till the end of the recording. During the later stimulation of well GPK3 in 2003 a dual stimulation was per-

formed by also injecting in GPK2 5.5 days after start of injection in GPK3 [Dorbath et al., 2009]. GPK2 was shut-in after 30 hours of injection, while injection in GPK3 continued for another three days. A similar behavior of the  $z'$ -component as described above for the stimulation in 2000 is observed upon shut-in of GPK2. No peculiarities are found for the shut-in of GPK3 later on. Therefore we conclude that GPK2 shows a special behavior of shut-in which is probably related to the structures connected to the well and reactivated during the stimulation operations.

Our interpretation of this observation is constituted of different elements. First we have to note that the open hole section is situated in two different facies of granite. After Hooijkaas et al. [2006] the

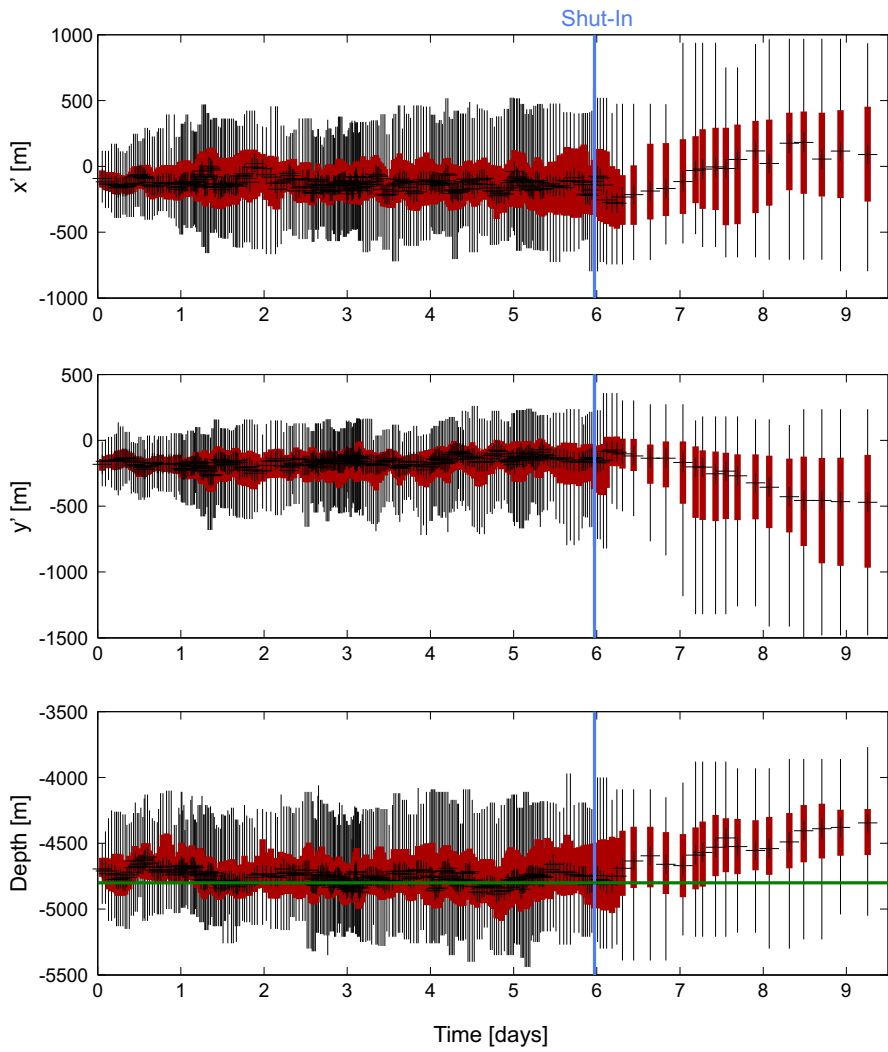


Figure 5.2: Boxplots for each coordinate in a rotated coordinate system. Black crosses are the median value for each time bin, red bars indicate the 25 and 75 percentiles, and black lines give the total range of values except for extreme outliers. The green line approximates the transition from the altered monzogranite on top to the two-mica granite on bottom [Hooijkaas et al., 2006].

crystalline basement constitutes of a two-mica granite and a more altered porphyritic granite on top of it. The boundary between the two granites was found at a depth of 4820 m and 4836 m (MD) at the wells GPK<sub>2</sub> and GPK<sub>3</sub>, respectively. The transition between these two granite facies is marked in Figure 5.2 (bottom) by the green line. During injection seismicity occurs on both side of this transition depth. However, after shut-in seismicity systematically migrates into the shallower porphyritic granite facies. This might be due to the contrast in mechanical properties, such as fracture compliance, friction angle and compressive strength of the two granite facies. Second, the planar features visible in the relocations by Calo et al. [2011] after shut-in demonstrate that few large fractures have been reactivated upon shut-in. As demonstrated by Schoenball et al. [2012] for the same stimulation experiment, rupture of small asperities of a larger fault structure can trigger rupture on neighboring asperities of the same fault structure by static stress transfer. During the injection period however, seismicity occurred in a volumetric fracture network rather than on single fracture structures. In such an environment, the triggering mechanism is less effective. Additionally, the perturbation of the stress field by the increased pore fluid pressure is expected to be much larger close to the well, than more than 1 km away from the well. Therefore static stress transfer contributes only negligibly to the total stress perturbation close to the well and especially during injection [Catalli et al., 2013]. Complementary observations of variations of the electric potential during and after the stimulation revealed a remarkable increase of the streaming potential following shut-in [Darnet et al., 2006]. This is interpreted as a persistent fluid flow in the reservoir following shut-in. This underpins our hypothesis that following shut-in fluid is pushed into single fractures leading to high flow rates and enhanced seismicity.

### 5.3 CONCLUSIONS

We have shown remarkable features of well GPK<sub>2</sub> at Soultz when subjected to hydraulic stimulation and specifically shut-in. While no trend in the location of seismicity was observed during injection a clear trend was observed for the shut-in period. Unlike observations in other wells at Soultz show, seismicity starts to migrate upwards just after shut-in. This could be related (1) to the presence of two mechanically different granite facies and (2) to large scale fault structures which permit propagation of seismicity e.g. by static stress transfer.

**ACKNOWLEDGEMENTS**

We thank EOST, Strasbourg for providing the seismic catalog and GEIE for providing the hydraulic data. We are grateful to EnBW Energie Baden-Württemberg AG for financial support.



# 6

---

## CHANGE OF STRESS REGIME DURING GEOTHERMAL RESERVOIR STIMULATION

---

This chapter is published in *Geophysical Research Letters*, 41,  
doi:10.1002/2013GL058514.

### ABSTRACT

Earthquakes are induced by man-made changes of the stress field by injection or withdrawal of fluids in hydrocarbon production, geothermal exploitation, and wastewater disposal. However, the actual perturbation of the stress field and stress release by injection-induced seismicity remains largely unknown. We provide evidence for currently not understood hydromechanical processes after shut-in of the well. We invert earthquake focal mechanisms from a massive stimulation to invert for stress resolved in time and depth to obtain changes of the stress orientation and magnitude. Prior information about fracture orientations from well logs is taken into account. Comparison with independent stress measures reveals that stresses obtained from inversion of fluid-induced seismicity are highly perturbed and not representative of the initial stress field. The horizontal stresses change by tens of megapascals, turning the stress regime from transitional normal faulting/strike-slip faulting to pure normal faulting. The observed stress changes are attributed to large-scale aseismic deformation.

### 6.1 INTRODUCTION

The detailed geological and geophysical investigations around massive fluid injection experiments make them a valuable tool for studying mechanisms of seismicity in a relatively well-controlled environment. Hence, deep fluid injection experiments have a long tradition in research on the mechanical properties and the stress state of the Earth's crust [e.g. Raleigh et al., 1976; Zoback and Harjes, 1997]. Recently, induced earthquakes in the surrounding of oil, gas and geothermal exploration, exploitation and deep wastewater injection have caused increased public awareness and the urge for a better understanding of the processes responsible for generating seismicity

[Ellsworth, 2013]. Besides, natural sequences of seismicity are often connected with deep fluid flow [e.g. Toda et al., 2002; Hainzl, 2004]. Here, induced seismicity might help us to understand such sequences and the mechanics of earthquakes.

At the exceptionally well-documented enhanced geothermal system in Soultz-sous-Forêts (France) a massive injection with wellhead pressures in the order of 14 MPa was maintained over 6 days during the stimulation treatments of well GPK2 in 2000. Obviously such a massive pressurization accompanied by thousands of recorded microearthquakes tremendously perturbs the local stress field. Yet, the actual evolution of the stress field during stimulation remains largely unknown. Based on the analysis of recorded seismicity, Cornet et al. [2007] suggest that the stress field rotates with depth. Cuenot et al. [2006] obtain different stress regimes from focal mechanism solutions (FMS) at the top and the bottom of the reservoir. Resolved spatially or temporally inversion of focal mechanisms can be used to study the evolution of the stress tensor, e.g., during aftershock sequences [Michael, 1987a; Hardebeck and Michael, 2006; Hardebeck, 2012]. Using these methods, Martínez-Garzón et al. [2013] traced changes of the stress tensor in time and depth during production in The Geysers geothermal field which correlate with production history.

In this study, we provide observations indicating hydromechanical coupled processes in connection with the shut-in of the well that have been unidentified to date. We use the stress inversion technique, extended with a probabilistic method to consider prior information of fracture planes, to study changes of the stress field in depth and time during and after injection.

## 6.2 OBSERVATIONS

The 5000 m deep well GPK2 of the Soultz-sous-Forêts enhanced geothermal system penetrates granite in a horst structure, covered by 1400 m of sediments [Genter et al., 2010]. Fresh water was pumped with rates of 30 to  $50 \text{ l s}^{-1}$  for 6 days peaking in 14.5 MPa wellhead pressure. In total, 7215 seismic events with a maximum moment magnitude of 2.5 could be localized. For 715 events with  $M_W > 1$  FMS were derived [Dorbath et al., 2009; Schoenball et al., 2012] and these form the basis of our analysis. Figure 6.1 shows the hydraulic parameters of the stimulation along with the seismic response. Seismicity rate was computed from the full catalog cut down to its completeness magnitude of  $M_c = 0.1$  to correct for varying detection thresholds.

Following Frohlich et al. [1992] the orientation of the pressure, null and tension (P, B and T) axes of the FMS are related by

$$\sin^2 \delta_P + \sin^2 \delta_B + \sin^2 \delta_T = 1, \quad (6.1)$$

where  $\delta_P$ ,  $\delta_B$ , and  $\delta_T$  are the plunges of the P, B, and T axes respectively. In this definition normal faulting (NF) mechanisms have

$\delta_P \approx 90^\circ$ , with  $\delta_B$  and  $\delta_T$  close to  $0^\circ$ . Strike-slip faulting (SS) corresponds to  $\delta_B \approx 90^\circ$ , and thrust faulting (TF) corresponds to  $\delta_T \approx 90^\circ$  with the other plunges close to zero. The relative proportions of faulting style are defined as  $f_{NF} = \sin^2 \delta_P$ ,  $f_{SS} = \sin^2 \delta_B$ , and  $f_{TF} = \sin^2 \delta_T$  [Frohlich et al., 1992].

We compute an averaged FMS by applying a moving window of 21 events and decompose it into relative proportions of  $f_{NF}$ ,  $f_{SS}$ , and  $f_{TF}$ . In agreement with earlier studies on FMS at the Soultz site [Cuenot et al., 2006; Charléty et al., 2007; Horálek et al., 2010], events have predominantly NF mechanisms with an averaged  $f_{NF} \approx 79\%$ . However, following shut-in of the well, the TF component of the averaged FMS increases significantly from an average of 7% during stimulation to around 15% after shut-in (Figure 6.1).

Further evidence for these yet not understood mechanisms is given by electric measurements that are independent of the seismic observations. Marquis et al. [2002] show that the streaming potential increases significantly just after shut-in (Figure 6.1). This observation can be interpreted as an enhancement of subsurface fluid flow during this period of the experiment. Peculiarities of postinjection seismicity migration for this stimulation experiment have been noted before [Dorbath et al., 2009]. Calo et al. [2011] found an alignment of seismicity in linear structures only during the postinjection period. Schoenball and Kohl [2013] demonstrate a clear change of event locations from stationary events during injection to a migration toward the south and upward in the postinjection period. Here static stress transfer might be responsible for progressive triggering, leading to a migration of seismicity locked on large scale faults [Schoenball et al., 2012]. Together these observations indicate to up to now not recognized hydromechanical processes in connection with shut-in.

The phenomenon of pronounced seismic activity following shut-in has been widely observed at geothermal sites, both during exploration and production phases [Evans et al., 2012], but remains poorly understood. Models by Baisch et al. [2010] and Goertz-Allmann and Wiemer [2013] may be able to explain the decrease of the  $b$  value and the occurrence of the largest events in the postinjection periods, but they cannot explain the observations such as a sudden change of earthquake mechanisms and of the hydraulic regime.

### 6.3 FAULT PLANE IDENTIFICATION

To further investigate the peculiarities observed in connection with shut-in, we conduct stress inversions from FMS to obtain the spatiotemporal evolution of the stress tensor. This technique requires the identification of the fracture plane among the nodal planes as a first step, which is a classical problem of seismology. In the well-defined environment of hydraulic stimulation, additional information is avail-

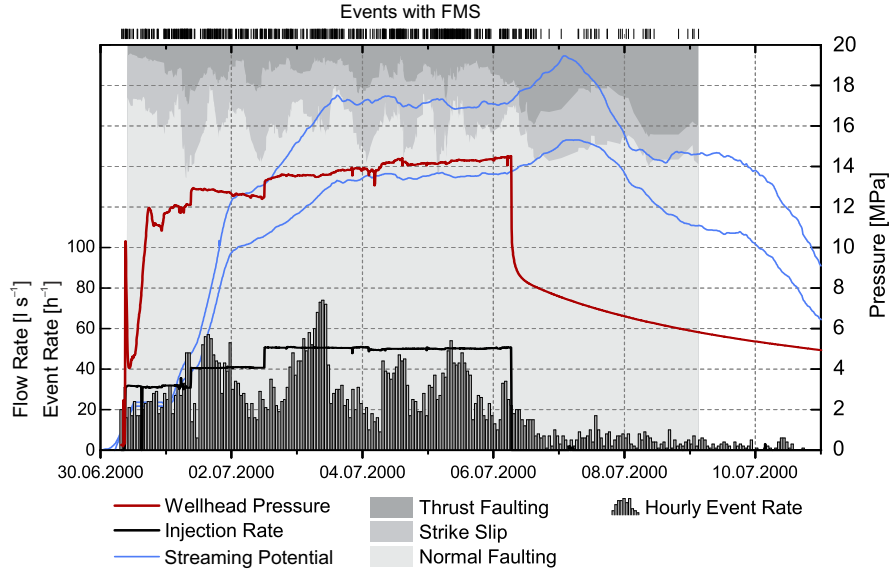


Figure 6.1: Injection rate (black) and wellhead pressure (red) of the stimulation and hourly seismicity rate (gray bars) of events larger than  $M_c$ . The gray shading shows the relative components of faulting style as  $\sin^2(\delta_{P,B,T})$  averaged over a sliding window 21 events wide. Blue are measurements of the self-potential made by Marquis et al. [2002] and averaged at two sites, drawn in arbitrary units. On the top the occurrence times of events with a focal mechanism are marked by vertical bars.

able that helps to identify the fracture plane. Schoenball et al. [2012] selected the plane, where the critical pore pressure  $p_{crit}$  needed to rupture that plane is minimal, as the fracture plane. Terakawa et al. [2012] inverted both nodal planes for the stress tensor individually and chose the plane which yields a stress tensor closer to the stress tensor obtained from independent stress measurements as the fracture plane. However, no structural information of the reservoir was taken into account in both approaches and no confidence measure was estimated.

We propose here a multistep approach to the problem by accounting for available information on fracture geometries derived from well logs. We then consider hydromechanical constraints implied by water injection. The aim is not only to identify the fault plane, but to estimate the confidence of the identification as well. Our approach is built up in a way that additional prior information about parameters or measurement errors (for example, for the FMS) can be incorporated, if available.

In the first step, the proximity of a nodal plane orientation to the existing fractures in the reservoir is used to derive a probability distribution for each nodal plane to be a preexisting fracture plane (gray path in Figure 6.2). We use fractures identified from Ultrasonic Borehole Imager and Formation Micro Imager wellbore imaging of wells

GPK2-4 in the depth section of 3000 – 5000 m (Figure 6.2a). A weight is computed for all fractures to correct for the sampling bias of inclined fractures along a wellbore wall [Terzaghi, 1965]. The correction factor  $1/\cos \alpha$  is capped at 10, corresponding to a maximum incidence angle  $\alpha$  with the wellbore trajectory of  $84^\circ$ . For each pair composed of a FMS and a randomly picked fracture, we compute the angular distance  $\angle(\text{fracture}, \text{FMS})$  of the normal vectors.

We then estimate the probability of each nodal plane to coincide with the selected fracture, considering the error prone determination of the FMS. A von Mises-Fisher [Fisher, 1993] probability density function with a mean direction  $\mu$  of a fracture normal with the concentration parameter  $\kappa$  and the normalization constant  $C(\kappa)$  is assigned as

$$\text{PDF}(x) = C(\kappa) \exp(\kappa \mu^T x). \quad (6.2)$$

We compute the cumulative distribution function (CDF) for a concentration factor  $\kappa = 200$ , corresponding to a standard deviation of the focal mechanism determination of  $4.05^\circ$  for each direction angle (Figure 6.2b). We consider the probability of a nodal plane to be the effective fracture plane as proportional to the probability density function of the angular distance to the Terzaghi-corrected fracture data set: a nodal plane is more probable to be the actual fracture plane if its orientation is close to the fracture directions determined from wellbore imaging. Based on this consideration, we draw samples from the initial fracture data set and retain them with a probability determined by inverse sampling the corresponding CDF in Figure 6.2b. Then, the critical pore pressure  $p_{\text{crit}}$  for each perturbed fracture is computed from the fracture orientation and assuming a stress field and Coulomb criterion as determined by Cornet et al. [2007]. Finally, we obtain a distribution of accepted samples  $p_{\text{crit}}$  for both nodal planes (Figure 6.2d).

In the second step, we compute a  $\text{PDF}(p_{\text{crit}})$  for each nodal plane, taking into account the error of FMS determination (red path in Figure 6.2). Since the fluid pressure decreases with distance from the injection well, the probability to trigger a fracture with a higher critical pore pressure  $p_{\text{crit}}$  is in general smaller compared to a lower  $p_{\text{crit}}$ . To account for this effect, we multiply the  $\text{PDF}(p_{\text{crit}})$  for each nodal plane with a factor 1 for critical pore pressures of  $p_{\text{crit}} = 0$  and linearly decreasing to 0 for  $p_{\text{crit}} = 20 \text{ MPa}$  (Figure 6.2c). All planes with critical pore pressures of  $p_{\text{crit}} > 20 \text{ MPa}$  are considered unrealistic given the maximum sustained injection wellhead pressure of  $14.5 \text{ MPa}$  and allowing for uncertainty and spatial variation in the determination of the Mohr-Coulomb criterion for reactivation of pre-existing fractures (Figure 6.2e). This very simplistic model for the pressure distribution was chosen on purpose over other analytical models in order to reduce a bias due to a particular model requiring further assumptions on the hydraulic flow in the reservoir as either

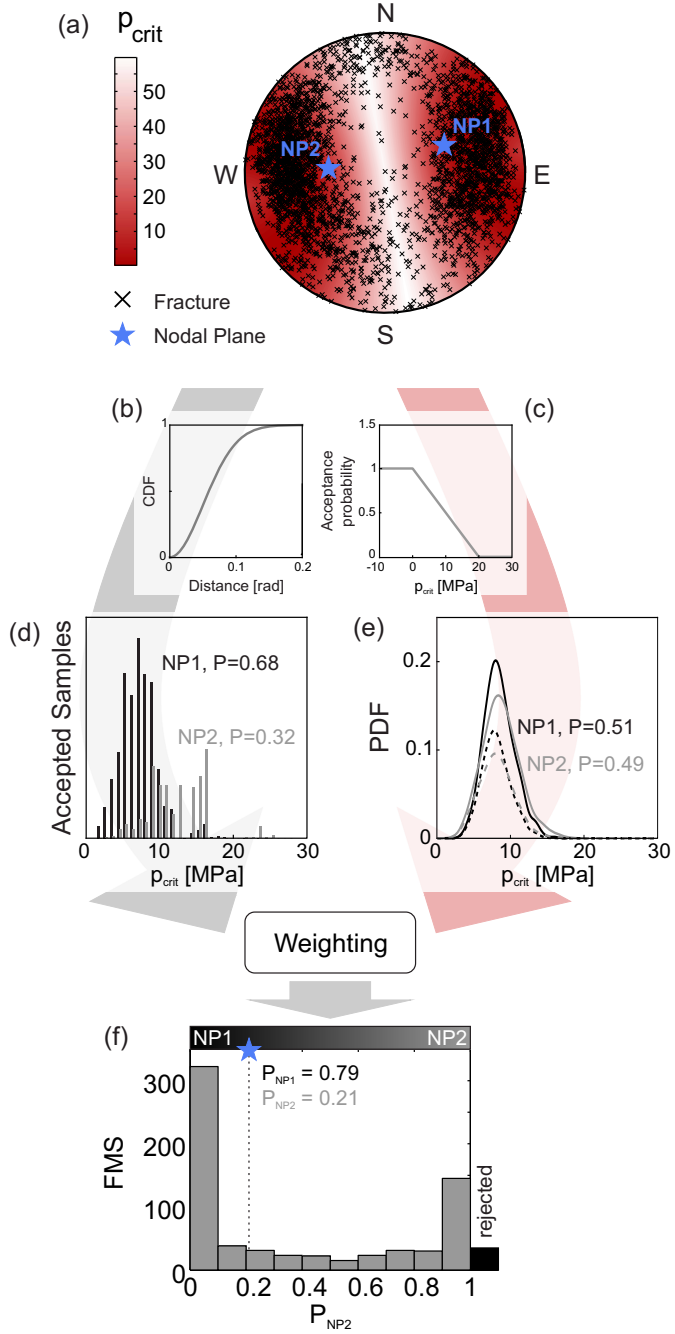


Figure 6.2: Quantification of the probability to determine the fracture plane for one sample FMS. (a) Normal vectors of fractures identified on wellbore logs and of the two nodal planes of the FMS on lower hemisphere projection. The red shading corresponds to  $p_{\text{crit}}$ . (b) Cumulative distribution function of the von Mises-Fisher distribution for  $\kappa = 200$ . (c) Probability to retain a nodal plane as function of pore pressure in the reservoir. (d) Distribution of  $p_{\text{crit}}$  for accepted samples for NP1 and NP2. (e) Distribution of critical pore pressures for nodal planes with added von Mises-Fisher distributed errors (solid) and multiplied with the pore pressure probability (dashed) for the example FMS. (f) Probability distribution of the fracture plane to be either NP1 or NP2 for all FMS.

porous matrix flow or fracture flow or mixtures. Yet it covers the first-order observation of pore pressure decrease with radial distance from the injection well. In a final step, the normalized marginals for all samples of the nodal planes are determined, yielding relative probabilities of each nodal plane to be the fracture plane.

Out of the catalog of 715 FMS the fault plane could be determined for 680 FMS and 467 fault planes could be determined with > 90 % confidence (Figure 6.2f). The fault planes of 35 FMS could not be determined by our model, as  $p_{crit} > 20 \text{ MPa}$  for both nodal planes; hence, they were rejected by the pressure distribution factor. The mechanics of these events remain unclear, as they would require unusually low friction angles to be triggered by the pore fluid pressure perturbation of the hydraulic stimulation when assuming a Coulomb criterion. We still included them in the further analysis, since they were measured and might hold valuable information. For these events we assumed a 50 % probability for each nodal plane.

#### 6.4 STRESS INVERSIONS AND RESULTS

In order to image the stress in the Soultz reservoir, we use the stress inversion code SATSI [Hardebeck and Michael, 2006]. This code enables damped inversion when spatially and/or temporally resolved inversions are performed, taking inversion results of neighboring bins into account. This procedure enables a reduction of the complexity of the resulting stress model in order to minimize artifacts due to poor data coverage or outliers [Hardebeck and Michael, 2006].

While SATSI is capable of 4-D inversion, we restrict our analysis to problems of lower dimensionality. In doing so, we implicitly assume a stress field constant along the neglected dimensions. Inversions of the 1-D temporal evolution of the stress tensor orientation showed an apparent rotation of the stress tensor during the postinjection period. However, closer investigation revealed that this might be a geometrical effect, as events migrate upward during this phase of the experiment [Schoenball and Kohl, 2013], and the observed stress rotation reflects spatial stress changes rather than temporal stress changes. Also, postinjection events have a higher TF component (Figure 6.1) which might be related to the observed rotation of the stress tensor following shut-in. From these observations we conclude that the inferred rotation of the stress tensor is either related to (a) the location of seismicity in depth, which might be due to changing geology. In fact, the shallow section of the reservoir (down to approximately 4800 m) is different to the one in the deep section [Hooijkaas et al., 2006]. Or (b) temporal changes of the stress tensor are caused by hydromechanical couplings related to the transition from coinjection to postinjection phases of the experiment.

For further analysis we bin the catalog of FMS in 20 bins each in time and depth, implicitly assuming no variation of the stress field in horizontal directions. Due to the damping used during inversion even bins with very few events still yield consistent results. To test the robustness and estimate confidence intervals of our results we perform 2000 inversions each on a data set perturbed as follows. For each FMS, we randomly draw the fault plane according to the previously determined probability distribution of the nodal planes. In order to capture the location uncertainty, we add normally distributed errors with a standard deviation of 50 m to the depth coordinate and von Mises-Fisher distributed errors with  $\kappa = 200$ , as described above, to the P, B, and T axes of the nodal plane. To test the robustness toward removal of data points, we perform 100 jackknife tests for each of these data sets by randomly removing 10 % of the FMS from the data set that is used for the inversions. The damping parameter  $e$  for the inversion is retrieved from the trade-off between the complexity of the resulting model versus the misfit of the model with measured data (Figure 6.3a). A slightly overdamped value of  $e = 0.8$  was chosen. Stress inversion yields the nonisotropic parts of the principal stresses  $\sigma_1$ ,  $\sigma_2$ , and  $\sigma_3$  and therefore also the shape factor

$$\phi = \frac{\sigma_2 - \sigma_3}{\sigma_1 - \sigma_3}. \quad (6.3)$$

The isotropic part of the stress tensor (which includes the pore pressure perturbation due to fluid injection) and hence stress magnitudes cannot be determined from stress inversions without further assumptions.

We find a normal faulting regime with  $\sigma_1$  close to vertical for the entire experiment. Taking the stress magnitudes of the unperturbed stress field as determined by Cornet et al. [2007], we would expect  $\phi \approx 1$ . The results of the stress inversion, however, show very different values. In Figure 6.3d, we show  $\phi$  averaged from all inversions and the orientation of the maximum subhorizontal stress  $S_{H\max}$ . Figures 6.3b and 6.3c show the distribution of  $\phi$  in sections of the 2-D inversion (location of sections indicated with black lines in Figure 6.3d). Starting from the open hole section of the well GPK2 between 4390 m and 4940 m depth, a front of very low  $\phi$  propagates both upward and downward, delineating the propagation of induced seismicity. Initially, shallower parts of the reservoir show a high value of  $\phi$  but do not reach the expected order for the unperturbed rock of  $\phi \approx 1$ , since their stress field is already perturbed by seismicity. A minimum of  $\phi$  is reached after 3 days in the depth where the open hole section of the well is cut by two major inflow zones as identified by Sausse et al. [2010]. Here  $\phi$  is reduced to almost zero, which translates to  $\sigma_2 \approx \sigma_3$  or applied to the NF stress field in Soultz that  $S_{H\max} \approx S_{h\min}$ . Assuming that the vertical stress is equivalent to the overburden, we can consider it to be constant throughout the stimulation. A change in  $\phi$

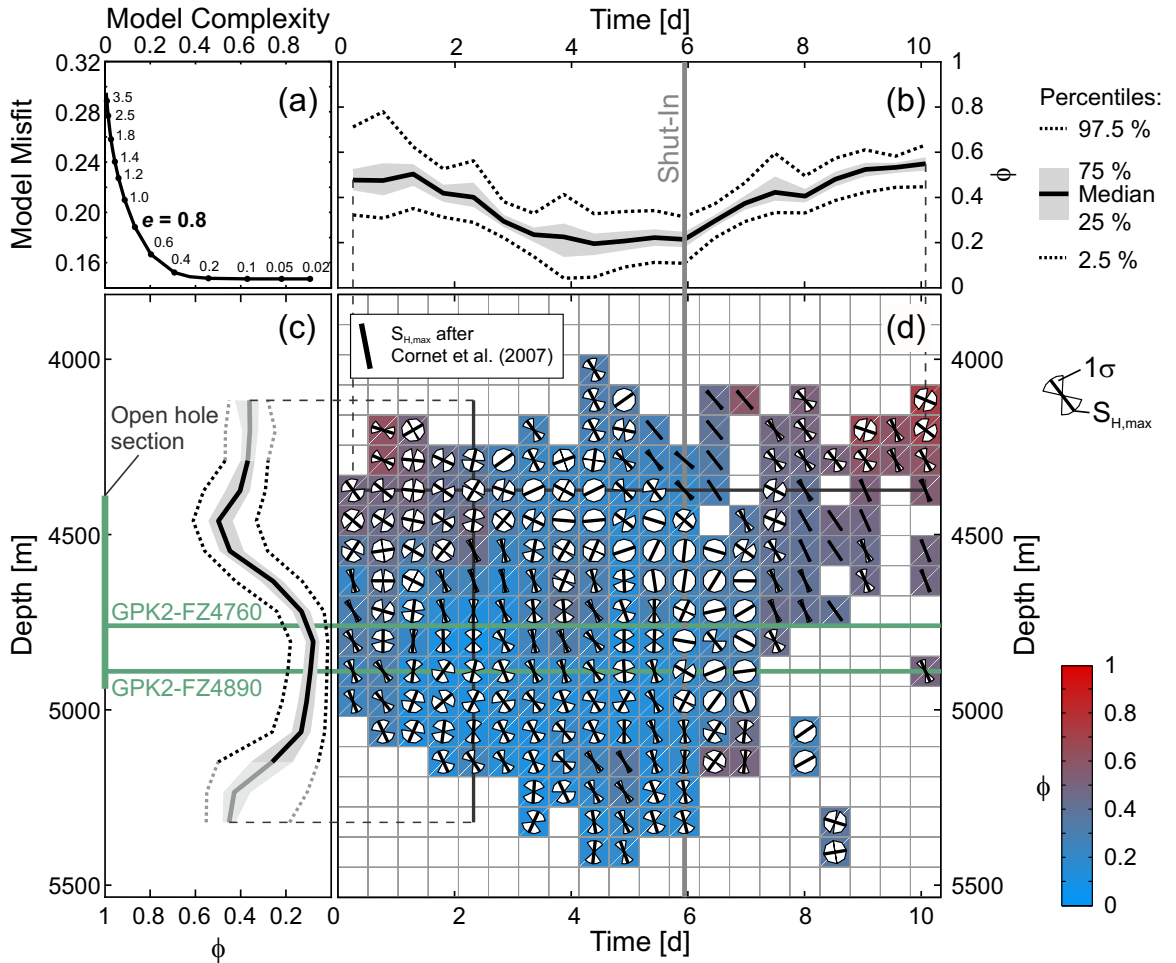


Figure 6.3: Two-dimensional stress inversion in time-depth space. (a) The trade-off between the complexity of the model, the data misfit and the damping parameter  $e$ . (b and c) Sections of the results in time and depth, respectively, showing median of  $\phi$ , its variation by first and third quartiles (shading), and range of the 95 % confidence interval (dashed). (d) Color-coded  $\phi$ ; the position of Sections in Figures 6.3b and 6.3c is indicated with black lines. The symbols in each bin indicate the direction of  $S_{H,\max}$  and its  $1\sigma$  variation. Bins that were successfully determined in less than 25 % of the inversions (representing single events with large perturbations of depth) are not drawn. The gray line marks the time of shut-in; green lines highlight two major fracture zones with significant fluid inflow.

can therefore be attributed to an increase of  $S_{h,\min}$  or a decrease of  $S_{H,\max}$  or both. Either way, the stress changes required to change  $\phi$  as determined are in the order of tens of megapascals, as shown by the stress polygon after Zoback et al. [2003] in Figure 6.4.

The edges of the stimulated region show only a small perturbation of the stress field, whereas the strongest stress perturbations are confined to the seismically active volume. Analyzing induced seismicity in The Geysers hydrogeothermal field, Martínez-Garzón et al. [2013] find similar reductions of  $\phi$  within the reservoir, and increasing values outside. This behavior was predicted for production scenarios considering poroelastic coupling by Segall and Fitzgerald [1998].

Following shut-in,  $\phi$  increases gradually. This is mostly a geometrical effect, as after shut-in seismicity migrates into areas which were not active previously and therefore contain a largely unperturbed stress field, as observed at the beginning of the injection in the shallow part. Seismic activity in the previously active volume practically stops.

Also shown in Figure 6.3d is the orientation of  $S_{H,\max}$  and its standard deviation for each bin. Areas showing low values of  $\phi$  typically show a strong variation of the  $S_{H,\max}$  orientation. This behavior is expected as even small stress perturbations can lead to significant stress tensor rotations when  $S_{H,\max} \approx S_{h,\min}$ . Our findings of a strong reduction of horizontal shear stresses are supported by the fact that it is difficult to distinguish between NF ( $\sigma_1$  vertical) and SS ( $\sigma_2$  vertical) stress regimes from stress measurements based on borehole data, since  $S_v \approx S_{H,\max}$  [Cornet et al., 2007]. Yet, seismicity is predominantly of NF type. A reduction of  $S_{H,\max}$  changes the stress regime from a transitional NF/SS regime ( $S_v \approx S_{H,\max}$ ) to a pure NF regime with  $S_v > S_{H,\max}$ ; hence, only NF mechanisms are observed.

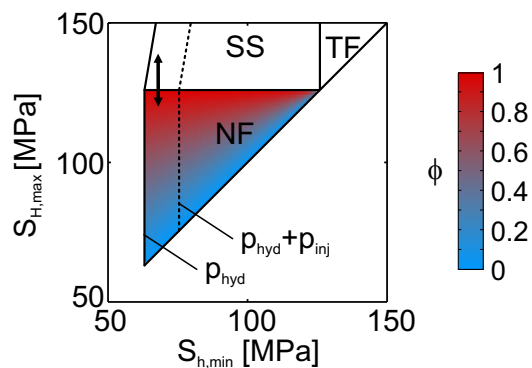


Figure 6.4: Lower part of stress polygon after Zoback et al. [2003] at 5000 m depth with shading for  $\phi$ . The range of the unperturbed stress field (double arrow) and coefficient of friction  $\mu = 1.0$  are taken from Cornet et al. [2007]. Dashed lines mark the change of allowed stress states for a pore pressure increase by 15 MPa.

## 6.5 CONCLUSIONS

New evidence is presented for the complexity of hydromechanical couplings occurring after termination of massive hydraulic stimulation treatments. In a detailed investigation, we determined a changing behavior of seismicity showing an upward migration and a change in mechanism during and after the stimulation experiment. This observation can partly be related to triggering by static stress transfer [Schoenball et al., 2012]. The observed change of earthquake mechanism and the enhanced fluid flow seen on measurements of the streaming potential Marquis et al. [2002] have not been explained previously.

Our analysis is based on stress inversions in which potential fracture planes were identified with a probabilistic method considering 715 FMS and additional structural and independent stress data as prior information. Random perturbation of the initial data set in its uncertainty domain allowed to quantify uncertainties in the stress distributions in time and depth. Derived spatiotemporal stress changes during massive hydraulic stimulation revealed a strong reduction of the maximum subhorizontal stress, changing the stress regime from transitional NF/SS to a pure NF regime. As a result, almost only pure NF earthquakes are observed during the stimulation. Similar results were obtained by Martínez-Garzón et al. [2013] for The Geysers geothermal reservoir in production conditions where a NF/SS stress regime was determined in an otherwise SS-dominated region. The observed change in earthquake mechanisms following shut-in can be explained as a result of the migration of seismicity into previously seismically inactive areas sampling a relatively unperturbed stress field.

Calo et al. [2011] obtained a large low-velocity zone centered on the microseismicity cloud of the GPK2 stimulation from 4-D tomography which was interpreted as a zone of large-scale release of stress in the order of several tens of megapascals. These complementary observations agree well with our findings. The comparison of our results with an analysis of the coseismic static stress transfer [Schoenball et al., 2012] reveals a large discrepancy with much more stress released than seismically observed. In line with the analysis of Calo et al. [2011] and indirect observations of large-scale creep at previous stimulations in Soultz [Cornet et al., 1997; Bourouis and Bernard, 2007], the stress discrepancy is strong evidence for large-scale aseismic deformations occurring during massive hydraulic stimulation. If we succeed in triggering specifically these aseismic processes during stimulation, we might hold the key to mitigate induced seismicity while meeting our goals for reservoir enhancement.

Furthermore, we propose that stress orientations gained from inversion of focal mechanisms of fluid-induced events are not representative of the initial virgin stress field. This interpretation is ob-

vious when comparing results of inversions with independent stress measurements obtained from wellbore logs. First, they sample the perturbed stress field and second, due to the strong reduction of  $S_{H\max}$  during stimulation, small (local) perturbations are sufficient to change the stress orientation significantly.

#### ACKNOWLEDGMENTS

This research was conducted within the portfolio topic GEOENERGIE of the Helmholtz Association of German Research Centres. We greatly thank the GEIE "Heat Mining" for support on the hydraulic, seismic and structural data. We are grateful to EnBW Energie Baden-Württemberg for financial support. Florian Wellmann was funded by a CSIRO Office of the Chief Executive Post-Doctoral Fellowship scheme within the CSIRO Earth Science and Resource Engineering Division. Fruitful discussions with Oliver Heidbach are greatly acknowledged.

# 7

---

## TIME-DEPENDENT BRITTLE CREEP AS A MECHANISM FOR TIME-DELAYED WELLBORE FAILURE

---

This chapter has been accepted for publication in International Journal of Rock Mechanics and Mining Sciences, doi:10.1016/j.ijrmms.2014.05.012.

### ABSTRACT

By drilling a wellbore cavity, high stresses arise at the wellbore wall, leading to the formation of breakouts which enlarge the hole to an elongated shape oriented along the direction of the minimum principal stress. If formation of breakouts is delayed, rock debris falls on the drill bit which may lead to stuck pipe problems or even abandonment of the drill string. Reasons for such time-delayed failure of the wellbore may be due to chemical fluid-rock interaction, especially in swelling clays. However, such delayed instabilities have also been observed e.g. in gneiss formations at the KTB borehole (Germany) that are not known to exhibit a swelling behavior. We propose to explain observations of delayed wellbore failure by time-dependent brittle creep, which has been observed for many types of rocks. Following this approach, rock fails under loads less than their short-time strength but after a long enough time span. This time is in exponential relation to the load applied to the rock. We implement a model developed for the creation of shear bands on the basis of time-dependent brittle creep by Amitrano and Helmstetter (2006). Here, progressive damage of the formation is captured by a damage parameter D and the time-to-failure TTF. Young's modulus E is decreased by a factor every time TTF is expired, i.e. when failure is reached. Subsequently, stresses are redistributed according to the new distribution of E in the formation. Using this approach, we obtain closure of the well with primary and secondary creep phases. Wellbore breakouts are formed progressively with deepening and widening of the initially damaged zone. After a certain time the formation of breakouts comes to an end with an Omori-like decay of failure approaching a steady-state.

### 7.1 INTRODUCTION

Analysis of the stability of underground excavations is a standard engineering task for the construction of boreholes, tunnels and mining shafts. Such man-made cavities perturb the local stress field tremendously, potentially leading to different kinds of rock failure. Besides the safety aspects of controlling rock failure, stability problems are a major cost factor for the creation of underground cavities. To prevent such problems, it is necessary to calculate the stress and displacement fields around artificial cavities to plan for adequate measures in order to prevent excessive failure of the rock. Stresses around a wellbore orthogonal to principal stresses were derived in the classical paper by Kirsch [1898]. Solutions for a more general case for inclined wellbores have been derived by Hiramatsu and Oka [1968]. At the wellbore wall, compressive stresses reach a maximum in the direction of minimal principal stress, leading to the formation of breakouts. Excessive breakouts can be an obstacle for the further drilling process, as e.g. material may fall on the drill bit leading to stuck pipe problems, which delays the drilling progress or may even end in the abandonment of the drill string and the wellbore. Besides, breakouts forming at the wellbore wall are used to determine the stress state of the crust. As breakouts in a vertical wellbore form in the direction of minimum horizontal stress, breakouts can be used to determine the orientation of the tectonic stress tensor. Zoback et al. [1985, 2003] show breakout growth in depth, but no growth in width is observed in their numerical simulations. This forms the basis to use breakouts as stress indicators for stress magnitudes by determination of breakout geometry and width [Vernik et al., 1992; Brudy et al., 1997; Haimson and Chang, 2002]. The previously mentioned studies use an elastic approach and a time-independent failure criterion to calculate the formation of breakouts. These approaches yield breakouts with a round shape. However, in laboratory experiments and in-situ V-shaped breakouts are frequently found [Lee and Haimson, 1993; Haimson, 2007; Zang and Stephansson, 2010]. Zoback et al. [1985] describe the growth of breakouts at depth using elastic solutions applied to iteratively generated geometries of the wellbore cross-section including the breakout. However, they lack to answer the question why breakout growth at depth stops at some point, but already point to inelastic effects necessary for a stabilization of breakouts.

There is ample evidence for time-dependent evolution of breakouts [Triantafyllidis et al., 2010]. Through repeated logging runs several examples of time-dependent breakout formation have been found. At KTB-VB scientific wellbore caliper logs were run 74 times over a period of over a year, making it possible to study time-dependent formation of breakouts at depths of 500 to 3000 m where the well advanced in gneiss and amphibolite rocks [Kessels, 1989]. For several depth intervals growth of breakouts within the first 20 to 100 days

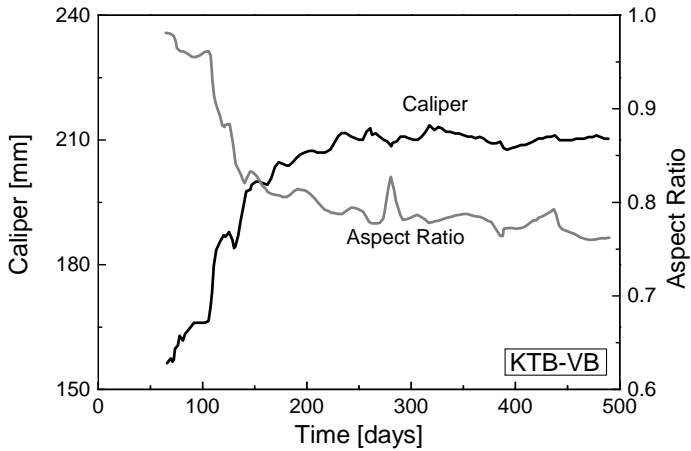


Figure 7.1: Caliper and ellipticity of well KTB-VB at the depth section 575-600 m obtained from 74 caliper runs showing the evolution of breakouts with time [modified from Kessels, 1989].

after drilling was observed, followed by stabilization and cessation of breakout growth (Figure 7.1). At the Soultz geothermal project no breakouts were observed in the granite formation immediately after drilling, but after 1 year extensive breakouts had formed [Cornet et al., 2007]. More recently, IODP scientific wells in muddy sediments south of Japan showed a time-dependent growth of breakouts [Moore et al., 2011].

Haimson [2007] describes the micromechanical processes of breakout formation as observed for different rock types in laboratory experiments. Possible mechanisms for time-dependent mechanical behavior are chemical interaction, most notable in clayey formations [Chen et al., 2003], or in the form of stress solution at crack tips [Rutter, 1976], diffusion of pore fluid pressure [Detournay and Cheng, 1988], thermal stresses and mechanical creep. The latter mechanism is subject of this study and is treated by the principle of time-dependent brittle creep as a consequence of e.g. subcritical crack growth or stress corrosion [Anderson and Grew, 1977; Scholz, 1968; Das and Scholz, 1981; Atkinson, 1984; Brantut et al., 2013]. Lockner [1998] experimentally derived a generalized law for the behavior of Westerly granite under general loading conditions. Using this law, he simulates time-dependent brittle creep with numerical methods. Amitrano and Helmstetter [2006] and Xu et al. [2012] model time-dependent brittle creep of 2D samples using the finite element method and explicit implementation of a time-to-failure law in the constitutive relations. They are able to numerically simulate e.g. creep strain curves and failure event rates that fit those of lab experiments very well. [Gran et al., 2012] use a block-slider model to simulate seismicity sequences. Specifically, to introduce the decaying activity of aftershock sequences, he introduces a time-to-failure approach. Within a cer-

tain parameter range, they obtain an event rate scaling conforming to Omori's law.

In this paper we combine a wellbore stress analysis with the numerical approach developed by Amitrano and Helmstetter [2006] in order to study the temporal evolution of breakouts. For this, we develop a finite element simulator for the problem of an arbitrarily oriented wellbore and implement the time-to-failure approach, incorporating effective elastic moduli. We propose to link the damage at the wellbore wall to Young's modulus by a linear relation between damage and Young's modulus as in Amitrano and Helmstetter [2006] but test also two different relations. We study the temporal evolution of breakout growth, as well of the shape of the breakouts and compare it with laboratory studies.

## 7.2 TIME-DEPENDENT BRITTLE CREEP

When rocks are subjected to high loads, but below their short-term strength they begin to creep. If the load is large enough, they show a trimodal behavior: the primary creeping phase is marked by a relatively high strain rate leveling off to a minimum value before it increases again. This phase of minimal strain rate was classically termed the secondary creeping phase, but there is debate over its actual existence [Brantut et al., 2013]. Tertiary creep is marked by an acceleration of strain rate after a certain amount of creep strain is reached [Baud and Meredith, 1997] leading to failure of the rock. The time from the beginning of such an experiment till the ultimate failure of the sample is termed time-to-failure  $t_f$ , and can be related to the applied load by an exponential law [Wiederhorn and Bolz, 1970]

$$t_f = t_0 e^{-b \frac{\sigma}{\sigma_0}}, \quad (7.1)$$

where  $\sigma$  is the applied load,  $\sigma_0$  is the short term strength of the rock and  $b$  and  $t_0$  are material constants of the rock. This kind of behavior is observed in many materials. It was first noted in glass and ceramics [Charles, 1958; Wiederhorn and Bolz, 1970] but later found also in natural rock material such as granite [Kranz, 1980; Kranz et al., 1982; Lockner, 1993; Masuda, 2001], sandstone [Baud and Meredith, 1997; Heap et al., 2009], limestone [Brantut et al., 2013], and basalt [Heap et al., 2011]. It is likely that the behavior of time-dependent brittle creep is not restricted to these materials. However for other rock types such as shales, the necessary experimental program to obtain the  $t_f$ - $\sigma$ -relationship is very tough, since the repeatability of rock strength experiments must be assured within narrow bounds.

Elastic approaches predict the wellbore wall to fail in compression by shear failure. Observations of breakouts under controlled laboratory environments however, show that tensile failure modes play an important role in the creation of breakouts [Haimson, 2007; Anders-

son et al., 2009]. This apparent discrepancy is typically explained by coalescence of tensile microcracks leading to macroscopic failure under compressional stresses [Brantut et al., 2012, 2013]. In our modeling we do not consider any particular failure mode, since brittle creep experiments are typically conducted in compression but showing evidence for tensile failure modes. However, the macroscopic observable, time-to-failure, is independent of microscopic failure modes.

### 7.3 NUMERICAL MODEL

For our simulations we use the commercial finite element software Abaqus (Simulia), version 6.11-2. In order to compute stresses around an arbitrarily oriented wellbore we model a 3-D slice orthogonal to the wellbore axis. We apply an initial stress field at an angle to the modeled domain to take the relative orientation of the stress tensor to the wellbore into account. Boundary conditions are chosen after Ewy [1993], i.e. the outer nodes are fixed, inner nodes of the wellbore wall are free. Periodic boundary conditions along the wellbore axis are realized by tying the nodes on the top of the modeling domain to the nodes on the bottom in pairs, such that their respective displacements in all three directions are identical (Figure 7.2). These conditions guarantee that lines parallel to the wellbore axis remain parallel and ensure a constant thickness of the modeled volume. Yet they allow for non-planarity and warping of the modeled volume. Using these boundary conditions, the analytical solutions for stresses around an arbitrarily oriented wellbore [Fjaer et al., 2008] are matched very well. In order to simulate the effect of the weight of the drilling mud, which is used to stabilize the wellbore wall, a surface load is applied to the wellbore wall. At the beginning of the simulation the nodes at the wellbore wall are fixed to simulate the undisturbed rock. Drilling of the well is simulated by instantaneous release of this boundary condition. Additionally a radial pressure is applied to the wellbore wall representing the weight of the drilling fluid. While in principal any orientation of the wellbore can be modeled by this setup, results shown hereafter are for the case of a vertical wellbore.

To incorporate time-dependent brittle creep, we follow closely the approach developed by Amitrano and Helmstetter [2006]. It bases on the assumption that time-dependent brittle creep increases the density of microcracks in a rock material. This is underpinned by numerous experiments [e.g. Heap et al., 2009], which show a remarkably congruent evolution of energy released by acoustic emission, strain and porosity changes over the time of the experiment. Increased crack density leads to degradation of the elastic moduli [Kemeny and Cook, 1986; Heap et al., 2010], thus reducing the capability of rock to support stress. Because of the degradation, stresses are redistributed increasing the load on neighboring elements. The basic con-

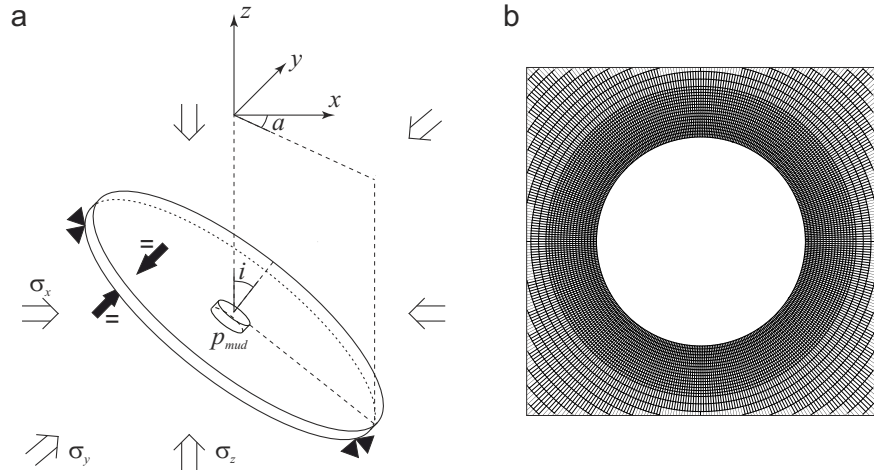


Figure 7.2: (a) Schematic of the FE model of a borehole with arbitrary orientation of azimuth  $\alpha$  and inclination  $i$ , fixed displacements at the outer boundary and tied displacements of upper and lower nodes. (b) shows a closeup of the refined mesh around the wellbore.

stitative behavior of the rock is modeled with linear elasticity. The time-dependent failure model is incorporated in Abaqus using a subroutine. Here the damage state of the model is read and updated according to the current stress state after each time step. The damage state of each element is described by the damage variable  $D$ , which takes the value  $D = 0$  for undamaged and  $D = 1$  for completely damaged states, and the consumed lifetime variable. If time-to-failure is not reached in an element, the proportion of time-to-failure which has passed in the last time step is stored and added to the consumed lifetime variable. When the time-to-failure is finally reached, damage is applied to the element by increasing  $D$  by a constant value  $D_0$  and the consumed lifetime is reset to 0 for this element. Time increments are adjusted in each increment accounting for the time-to-failure of the element closest to failure. The numerical model is summarized in a flowchart in Figure 7.3.

To calculate time-to-failure we employ Equation 7.1. In Amitrano and Helmstetter [2006]  $\sigma$  is the mean major stress, which is typically the vertical stress in a uniaxial compressive test. For our wellbore environment we have almost a uniaxial stress state with  $\sigma_{rr}$  being the difference between formation pressure and mud pressure, thus close to zero. The hoop stress  $\sigma_{\theta\theta}$  is the principal stress determining failure at the wellbore wall, thus we replace  $\sigma$  in Equation 7.1 with  $\sigma_{\theta\theta}$ . The hoop stress is obtained from the Cartesian stress components  $\sigma_x$ ,  $\sigma_y$  and the in-plane shear stress  $\tau_{xy}$ :

$$\sigma_{\theta\theta} = \frac{1}{2} (\sigma_x + \sigma_y) - \frac{1}{2} (\sigma_x - \sigma_y) \cos 2\theta - \tau_{xy} \sin 2\theta. \quad (7.2)$$

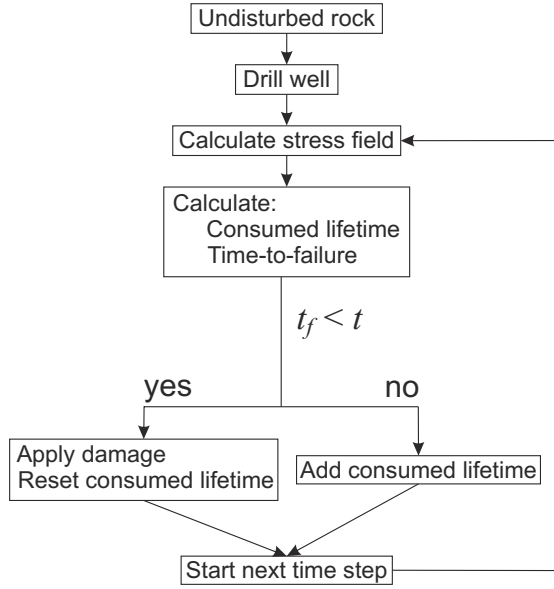


Figure 7.3: Flowchart of the FE simulation with time-dependent failure of single elements.

Input parameters are summarized in Table 7.1. The time-to-failure parameters  $t_0$  and  $b$  used are taken from Masuda [2001], who conducted creep experiments on granite samples. Other rock parameters are generic but are chosen with reasonable values commonly found in the literature. We have to emphasize here, that input parameters determined from slow creep tests are not straight forward to compare with our input parameters. The experimentally obtained values for  $t_f$  are for macroscopic failure of one sample. However in our simulations,  $t_f$  is considered for microscopic failure, which accumulates to macroscopic failure only after many cycles. We neglect any effects of varying water saturation or temperature changes, although they have a large impact on the actual time-to-failure behavior of rocks [Kranz et al., 1982; Heap et al., 2009].

The degradation of Young's modulus with increasing damage has been analyzed in several studies. From cyclic compressional tests on different rock samples Heap et al. [2010] find an approximately linear decrease of the macroscopic Young's modulus with increasing crack density. Nevertheless we tested several relationships with linear, concave and convex progression of Young's modulus as a function of damage to account for the uncertainty in the actual behavior of different rock types. Here we have to differentiate between the experimentally determined values of  $E$  being macroscopic quantities lumped over the whole sample, whereas in our simulations we need to use a microscopic  $E$  valid only for each element. Therefore, we reduce  $E$  to almost zero for complete damage of  $D = 1$ . This is unlike the experimentally obtained macroscopic values, where  $E$  is reduced by 10 – 30 % until macroscopic failure of the sample is reached, de-

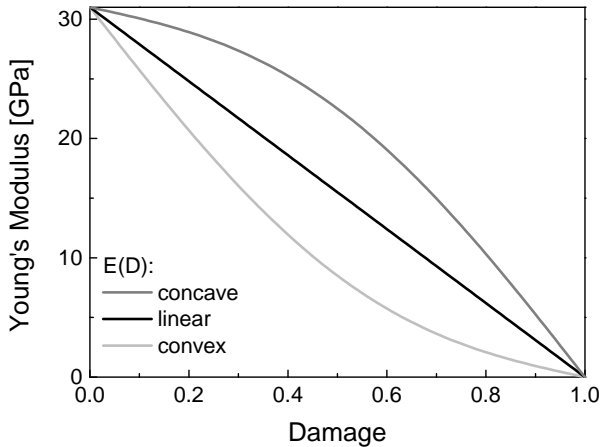
Parameter	Description	Value
<i>Strength parameters</i>		
$t_0$	TTF time factor	$2 \cdot 10^{22}$ s
$b$	TTF exponent	46
$\sigma_0$	uniaxial compressive strength	70 MPa
$D_0$	damage parameter	0.01
<i>Elastic parameters</i>		
$E_0$	initial Young's modulus	31 GPa
$\nu$	Poisson's ratio	0.36
<i>Stress field, effective stresses</i>		
$\sigma_{H,\max}$	maximum horizontal stress	35 MPa
$\sigma_{h,\min}$	minimum horizontal stress	20 MPa
$\sigma_v$	vertical stress	30 MPa
$p_{\text{mud}}$	mud overpressure	2 MPa

Table 7.1: Mechanical input parameters of the numerical model.

pending on the rock type. The used relationships between Young's modulus and damage are shown in Figure 7.4. As is discussed below, in all simulations damage does not increase further than to where the effective Young's modulus  $E_{\text{eff}}$  is reduced to about half its original value  $E_0$ .

#### 7.4 RESULTS

Figure 7.5 shows the evolution of breakouts for snapshots log-spaced in time in terms of hoop stress  $\sigma_{\theta\theta}$  and damage D. A gradual growth

Figure 7.4: Relation  $E(D)$  of Young's modulus  $E$  with increasing damage  $D$  for the three different models.

of the breakout with time is observed over the modeled period of  $10^6$  s (11.5 days). At the beginning, damage accumulates in a curved area adjacent to the wellbore wall. Here the hoop stress decreases very strongly as time and hence damage progresses. Due to the ongoing redistribution of stress following damage, the point of maximum hoop stress moves away from the wellbore wall to the inside of the formation. With increasing deepening of the breakout, slight stress increase is observed in the vicinity of the breakout tip. In the end, a stress distribution with only small stress gradients is observed which leads to much larger  $t_f$  and hence a much slower accumulation of damage.

The evolution of the breakout dimensions in width in degrees and depth  $a$ , normalized by the wellbore radius  $r$ , is shown in Figure 7.6. Here, any damaged elements are considered as part of the breakout. It is marked by a number of distinct features. At the beginning of breakout growth the shape is round with a shallow depth and an already large angular extend of around  $30^\circ$ . Then the breakout widens considerably to more than  $60^\circ$  and depth increases moderately from around  $0.05 a/r$  at the beginning to more than  $0.4 a/r$  in the end. The slope of growth in width decreases and the slope of growth in depth increases considerably when plotted in a semi-log plot as in Figure 7.6. Towards the end of the simulation, growth of breakouts is now mostly in depth, and width increases only moderately. Remarkable is the almost identical evolution of the breakout size for the three  $E(D)$  relations. But, since breakout size was defined as the area with any damage, this is not relevant for real-world comparison. Instead, we plot the shape of the breakouts normalized by the  $E(D)$  relation in terms of  $E_{eff}$  in Figure 7.7. We see that the shape is slightly dependent on the relation  $E(D)$  with linear and convex  $E(D)$  result in rounded breakouts, while for a concave  $E(D)$  the breakout tip is more pronounced and the breakout takes a V-shape. Although the amount of damage in the developed breakout is very different for the  $E(D)$  relations,  $E_{eff}$  is very similar for all simulations. This again underpins the robustness of our approach towards different relations for damage accumulation.

In the following, we analyze in further detail the late evolution of the breakouts coming to a stable state. For this we retrieve the event rate from the number of elements where damage was applied in one time step divided by the time increment. Figure 7.8 shows the evolution of event rate  $n$  over time. The log-log plot shows a power law decay of events as it is typically observed e.g. in earthquake aftershock sequences, which are commonly described by Omori's law [Utsu et al., 1995], one of the fundamental empirical relationships of seismology. The modified Omori law is

$$n(t) = \frac{k}{(c + t)^p}, \quad (7.3)$$

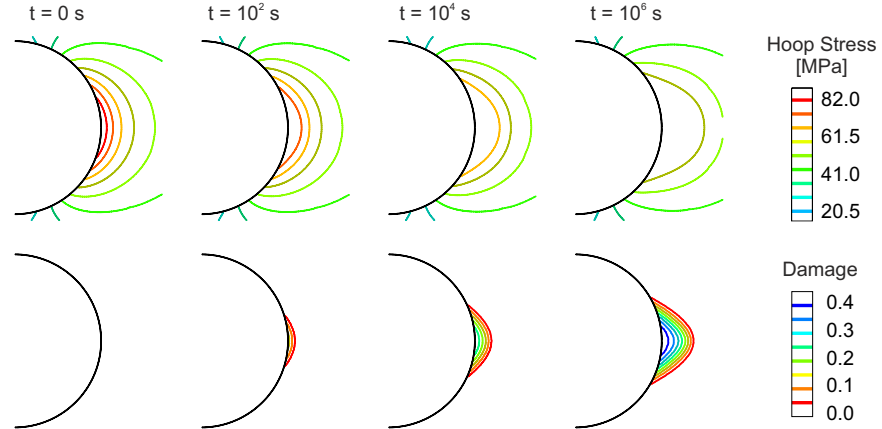


Figure 7.5: Evolution of hoop stress  $\sigma_{\theta\theta}$  (top) and damage (bottom) over time. Note the increase of stress away from the wellbore wall.

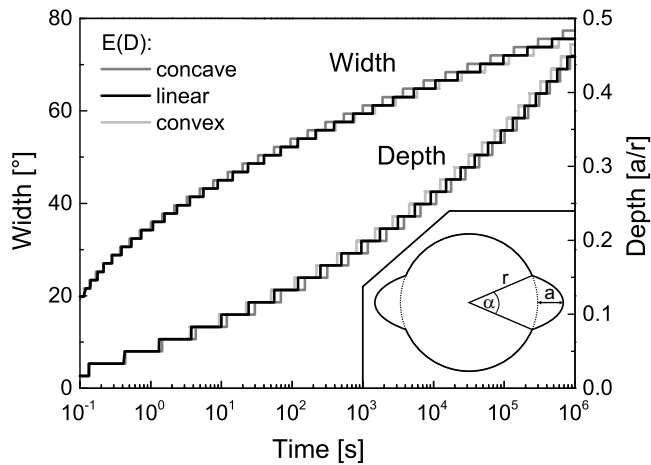


Figure 7.6: Growth of the breakouts for the linear and non-linear degradation relations. The width  $\alpha$  and the depth  $a$  are used as defined in the inset. Any damaged elements are considered as part of the breakout. Up to about  $10^3 \text{ s}$  growth of the breakouts in width and depth is observed, while later the breakout growths only in depth.

where  $k$  is the amplitude of aftershock activity,  $c$  is a time offset and  $p$  is an exponent describing the decay rate. Neglecting the time offset (which is a debatable quantity related to overlapping recordings of seismicity), we fit a decay exponent  $p$  in the order of 0.77 to 0.81 to the event rate, depending on the  $E(D)$  relation. These values are a bit lower than what is observed for aftershock sequences. Here values of  $p = 1.0$  to 1.2 are commonly found [Shcherbakov et al., 2004] representing a faster decline of activity. Our relatively small values of  $p$  is in agreement with the numerical experiments of uniaxial compression by Amitrano and Helmstetter [2006] and suggests a slower decay of activity by the process of time-dependent brittle creep, compared to most aftershock sequences.

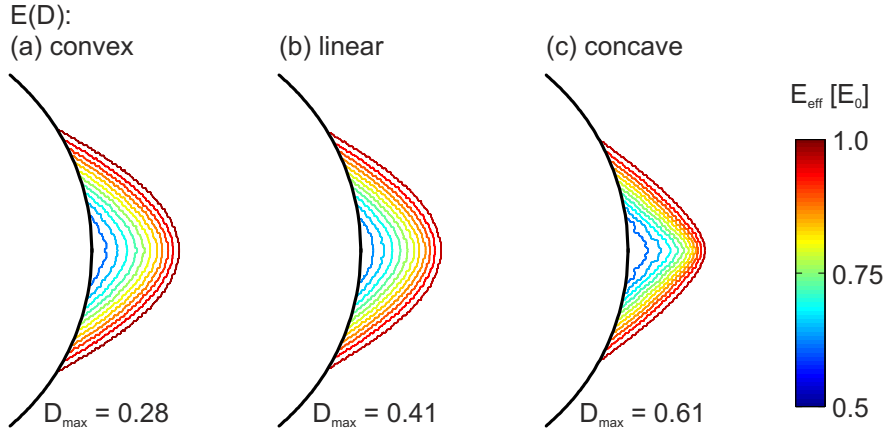


Figure 7.7: Shape of the breakout for different degradation relations of Young's Modulus drawn in effective Young's Moduli  $E_{\text{eff}} = E(D)$ .

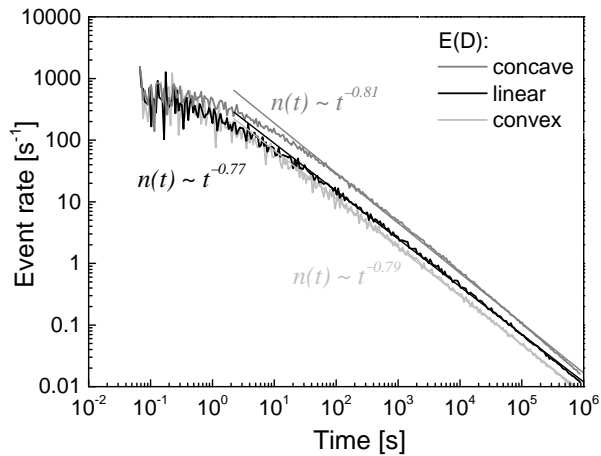


Figure 7.8: Decay of event rate during breakout formation for the three degradation relations along with fits of Omori's law with  $c = 0$ . All behave very similarly and comply with Omori's law with  $p \approx 0.8$ .

Laboratory experiments on uniaxially stressed samples suggest that Poisson's ratio  $\nu$  increases with increasing damage and progressive stiffness degradation of  $E$  [Heap et al., 2010]. We therefore checked the effect of increasing  $\nu$  with increasing damage for the linear  $E(D)$  relation.  $\nu$  was increased linearly with damage from 0.25 for undamaged matrix to 0.5 for  $D = 1$ . Comparing with the result for constant  $\nu$  the overall shape and size of the breakout is the same, however the areas of large damage have a slightly larger extent, both in width and depth. While the overall breakout has a round shape, the highly damaged areas take a V-shape.

For one test we solve the constitutive equations of poroelasticity [Rice and Cleary, 1976] incorporated in Abaqus instead of the elastic constitutive model. The boundary conditions were the same, ex-

cept for an additional condition for the additional degree of freedom, namely pore fluid pressure  $p$ . According to the mud pressure which is applied as surface load to the wellbore wall in all previous simulations, also pore fluid pressure is prescribed with the same value at the wellbore wall. Following the poroelastic approach, the time-to-failure criterion is evaluated using effective stresses ( $\sigma_{\text{eff}} = \sigma - p \cdot I$ ). To incorporate also the effect of increasing crack density with increasing damage on the hydraulic properties of the formation, hydraulic permeability  $k$  (in  $\text{m}^2$ ) is defined exponentially dependent on the damage variable, with  $\log(k) = -13$  for  $D = 0$  and  $\log(k) = -9$  for  $D = 1$  and linearly interpolated between these values. The effect of increasing pressure solution with increasing pore fluid pressure in the rock matrix is not captured by this simplistic poroelastic model, besides there is no experimental evidence that increased pore fluid pressure, but constant effective stresses, actually enhances subcritical crack growth [Heap et al., 2009]. Because of the stabilizing effect of pore fluid pressure in the rock matrix, the propagation of breakouts is slower for a poroelastic material than for an elastic material but follows the same general trend and shape. Therefore we did not study effects of poroelasticity any further.

## 7.5 DISCUSSION

Although they are almost never considered in typical analyses of wellbore failure, there is no reason why inelastic effects such as creep and accompanied time-dependent brittle failure should be absent along the borehole wall. Haimson [2007] observed the micromechanical processes of breakout formation in different kinds of rock. For the example of Lac-du-Bonnet granite he observes successive spallation of rock flakes from the borehole wall, that leave small cantilevers of rock behind, when the rock flakes fall off. The residual strength of these small cantilevers is enough to reduce the next flakes length. Eventually this cascade of less and less damaged rock leads to stable V-shaped breakouts. Comparing to our damage mechanics approach, the formation of individual rock flakes with microcracks in between can be regarded as stiffness degradation of a damaged rock material. Thus, the progressive failure of flakes of rock, combined with the accompanied stress redistribution can be suitably analyzed by a damage mechanics approach.

The evolution of borehole breakouts show common features of seismic aftershock sequences. The drilling of the well causes large localized stress perturbations, comparable to localized stress increases following an earthquake main shock. Similar to the release of stress peaks on fault asperities, heterogeneities along the wellbore wall caused by an increased microcrack density, fail over time through the processes of stress corrosion or brittle creep [Das and Scholz,

1981]. This releases localized stress peaks and eventually leads to a stable state, where stress perturbations are such that the time-to-failure grows to orders which are irrelevant for engineering processes.

## 7.6 CONCLUSIONS

We propose a simple geomechanical model to explain the time-dependency of wellbore breakouts. Using an implementation of time-dependent brittle creep to the commercial finite element package Abaqus we are able to match several characteristics of breakout growth in time, as observed in-situ. These are a relatively quick widening of the breakouts and subsequent growth mainly in depth, leading to a distinct V-shape. Overall the evolution of the breakout size comes to a halt by an Omori-type decay of event rate. The breakout geometry resulting from the time-dependent evolution shows the typical V-shape observed in many wells. This is caused by the development of an excavation damaged zone around the wellbore and the breakout reducing stresses in damaged elements and redistributing, i.e. increasing stresses to neighboring elements. With time, stresses are redistributed more and more such, that the residual strength of the excavation damaged zone is sufficient to support the residual stresses for very long time spans and the growth of breakouts stops. When using the geometry of breakouts to infer stress magnitudes, great care must be taken that a stable state has been reached. Still then the assumptions used to predict breakout size from a given stress state need to be verified and calibrated by experiments.

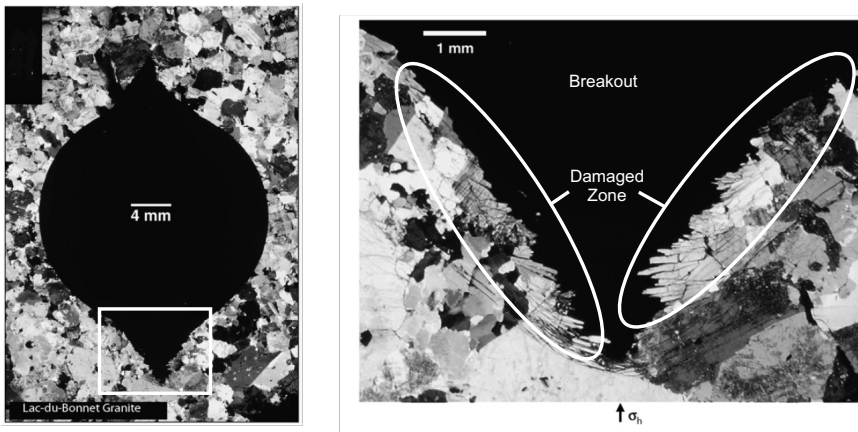


Figure 7.9: Breakout with dog ear-shape in a Lac-du-Bonnet granite sample created in a lab test. Adapted from Haimson [2007].

**ACKNOWLEDGEMENTS**

The work presented was partly conducted under the project "Reduzierung der geologisch bedingten bohrtechnischen Risiken - Bohrlochstabilität in tertiären Tonsteinfolgen im Oberrheingraben als Hindernis für die Erschließung geothermischer Reservoir" under management of Institute of Soil Mechanics and Rock Mechanics at Karlsruhe Institute of Technology with financial support by the German Federal Ministry for the Environment, Nature Conservation and Nuclear Safety, BMU, grant agreement no. 0327599. Additional funding by EnBW Energie Baden-Württemberg AG is acknowledged.

# 8

---

## CONCLUSIONS

---

In the last few years, induced seismicity has become an issue frequently encountered during projects for geothermal exploitation, non-conventional production of hydrocarbons and deep wastewater disposal [Ellsworth, 2013]. For future use of these techniques, the physical processes of induced seismicity have to be better understood to facilitate future mitigation of felt seismicity. Authorities, issuing permissions for such underground activities, require easy to handle and objective guidelines for the permission process to determine boundary conditions for a safe and sustainable use of these forms of energy exploitation. Likewise, politics and the society demand guaranteed safety and minimal nuisance by the exploitation to be able to accept the application of these technologies. In short, this requires reliable methods to forecast the seismic response of the reservoir to the projected hydraulic treatment and adequate means to control seismicity. In turn, these requirements lead to the funding of several joint research projects, e.g. the European project GEISER and the German project MAGS, that explicitly targeted the processes and possible means of mitigation of induced seismicity.

Forecasting natural seismicity is a highly controversial topic since many decades [Kanamori, 2003, and references therein]. While several cases exist where forecasts by various methods were successful, no convincing and reproducible forecasting methods could be established. Reasons are, among others, the lack of continuous measurements in space and time of field variables determining the state of the faults in the seismic cycle and the general complexity of geology. In the face of these difficulties, inevitable geological uncertainties need to be accounted for by probabilistic measures.

However, unlike natural systems, for cases of induced seismicity a lot more information on the state of the reservoir, e.g. from well logs, and specifically on the man-made perturbation of the stress field, e.g. by fluid injection, is known. This knowledge can already be used to predict the general behavior of seismicity during stimulation [Kohl and Mégel, 2007; Zang et al., 2013]. However, quantitative forecasts based on deterministic reservoir models still need to prove their reliability. Instead, current quantitative forecasting methods use statistical models, calibrated by real-time observation of induced seismicity

[Bachmann et al., 2011; Mena et al., 2013]. They are quite successful in forecasting the seismic response within a time frame of hours during the co-injection phase, i.e. when reservoir conditions do not change abruptly. Since these models do not typically take into account any physical processes but rely entirely on seismicity that already occurred during the operation, they are less useful to forecast the seismic response *a priori* or for sudden changes of the injection pattern, such as the shut-in.

The central objective of this thesis was to analyze the contributions of different time-dependent processes on the stress state in the reservoir and consequently their influence on the seismic response. I used methods developed for analysis of natural seismicity sequences and applied them to the induced seismicity case of hydraulic stimulation at Soultz-sous-Forêts. The additional knowledge of the reservoir as compared to typical systems bearing natural seismicity, stemming from logging data and stress measurements were used e.g. to tackle the classical problem of identifying the fault plane among the two nodal planes of one focal mechanism solution (Chapter 6). To account for remaining uncertainties originating from uncertainties of the focal mechanism solutions, variations of the stress field and the more or less unknown pressure perturbation within the reservoir, a probabilistic measure was derived to rank the quality of the fault plane identification.

Key to the analyses performed in this dissertation is the dataset of the stimulation of the well GPK2 of the EGS at Soultz-sous-Forêts, which consists of structural information from the wells in Soultz, hydraulic data and seismic catalogs, and most importantly the set of 715 focal mechanism solutions of all seismic events with  $M_w > 1$ . This unique dataset enabled analyses which were not possible at any other site up to now. This dataset was complemented by well logging data, stress measurements and precise geological models, resulting from more than 20 years of research at the Soultz-sous-Forêts pilot EGS site. This wealth of geological and geophysical information of the reservoir offered a unique opportunity for an integrated analysis of the seismicity, the hydraulic regime and the changes of the stress field of the reservoir undergoing hydraulic stimulation. This demonstrates the enormous scientific value of outstanding datasets and should be motivation for future efforts to acquire exceptional data.

## 8.1 MAJOR FINDINGS

The objective of the first study (Chapter 4) was to investigate whether the triggering effect by static stress transfer [King et al., 1994] plays a relevant role for induced seismicity during reservoir engineering by massive hydraulic stimulation. While this effect was successfully used to explain aftershock activity [Toda and Stein, 2003] and suc-

cessive failure of fault zone segments [Stein et al., 1997], its role in a seemingly pore fluid pressure dominated system, such as massive hydraulic stimulation, was an open question.

The analysis, based on a semi-analytical approach, has revealed that the static stress transfer produces a pattern of strong local variation of stress increases and stress decreases. Except for very localized regions on the meter scale, absolute stress perturbations are below 1 MPa with a linear decrease with distance from the fault plane. Only about 60 % of events analyzed were in areas of a positive stress perturbation, that is in areas where static stress transfer by previous events produced an enhanced triggering potential. Hence the triggering process plays a much smaller role, compared to e.g. aftershock sequences, where the seismicity pattern often appears to strictly follow positive stress perturbations [King et al., 1994].

While during the co-injection phase of the GPK2 stimulation in 2000, seismicity is active in a volumetric region which remains stationary in location, that pattern changes for the post-injection period. As discussed in Dorbath et al. [2009] and Calo et al. [2011] and analyzed in greater detail in Chapter 5, seismicity starts to migrate upon shut-in. The seismic activity moves into the shallower part of the reservoir above 4800 m depth and further to the south-east, where the more altered porphyritic granite facies occurs. Furthermore, seismicity now aligns in linear patterns [Calo et al., 2011], which is evidence for reactivation of single fault zones, confining the seismic activity. It appears that triggering by static stress transfer might play an increasing role at the edge of the stimulated volume where pore pressure perturbations are low and especially when seismicity is confined to single large scale structures, that are host to neighboring seismic asperities. Then the typical migration can be explained as triggered seismicity along a fault zone with a strong directionality. This migration behavior is very characteristic of natural swarm seismicity, where diffuse sources of stress perturbations cause seismicity [Hainzl and Fischer, 2002; Chen and Shearer, 2011]. The enhanced role of triggering during the post-injection period was confirmed later by an analogous study performed on the Basel stimulation dataset by Catalli et al. [2013].

The question, why exactly seismicity starts to behave differently during the post-injection period compared to the co-injection period remains unclear. It has been observed several times that the largest events of a sequence of induced seismicity typically occur during the post-injection period [Schindler et al., 2008; Bönnemann et al., 2010; Evans et al., 2012]. Few models exist that explain the general trend of larger events and decreasing b-value with time during the stimulation [Baisch et al., 2010; Goertz-Allmann and Wiemer, 2013]. These base on the continued propagation of the pressure front also after shut-in of the well, and hence an increasing affected volume. Then, since

events tend to get larger during injection, they continue to do so also following shut-in.

I demonstrated, that the change of earthquake characteristics with shut-in are not limited to a systematic change in magnitude or  $b$ -value. The migration pattern changes from a stationary spreading of the seismicity cloud to directional spreading along a fault zone. I showed that the focal mechanisms after shut-in are significantly different from those of the co-injection phase, showing a systematically larger thrust faulting component. Further evidence for up to now unrecognized hydro-mechanically coupled processes occurring during the singular transition from co- to post-injection phases is given by measurements of the streaming potential by Marquis et al. [2002]. These show an anomalous increase of the streaming potential just after shut-in, corresponding to an enhanced fluid flow.

While stress field determinations based on borehole breakouts and drilling induced tensile features [Cornet et al., 2007; Valley, 2007] reveal a stress regime at the verge of normal to strike-slip faulting, almost only normal faulting events were observed during the stimulation of GPK2, but also in other stimulations in Soultz [Horálek et al., 2010]. Interestingly, all focal mechanisms analyzed by Horálek et al. [2010] were in agreement with a pure double-couple model, hence pure shear-type faulting. Using focal mechanism solutions to invert for the stress tensor, I quantified the effect of the stimulation and resulting deformation on the stress field. I showed that the stress tensor apparently rotates, beginning with shut-in (see Figure 2.17). I also found that shallower focal mechanisms tend to have a larger component of thrust faulting. Based on this observation of change of focal mechanisms and stress orientations in depth and time, inversions were binned in 2D, with one dimension being time and the other being depth.

A strong reduction of the shape factor  $\phi$  with time, which could be translated to a strong reduction of the maximum horizontal stress  $\sigma_H$  and/or a strong increase of the minimum horizontal stress  $\sigma_h$ , was deduced. The stress regime changes from a transitional normal faulting/strike-slip regime to a pure normal faulting regime, which is the reason why mostly normal faulting events are observed. In this view, the observed change of faulting mechanism during the post-injection phase can be explained by the seismicity occurring in a largely unperturbed area. The faulting mechanisms with higher thrust faulting components are thus more representative of the initial stress field compared to co-injection events in the highly perturbed reservoir.

Comparing the results of the stress inversion with that of the static stress transfer analysis, reveals that the stress changes observed from inversion cannot be explained by displacements observed seismically. While the co-seismic stress changes are limited to the order of  $\pm 1$  MPa and high stress changes are strongly localized, the stress changes de-

rived from inversion of focal mechanisms is at least one order of magnitude larger. This is a strong indicator of large-scale aseismic movements, which was also suggested by Calo et al. [2011], based on results of a 4D tomography that revealed a strong reduction of P-wave velocities after the water injections. They inferred that stress changes in the order of tens of MPa are necessary to explain the observed velocity changes.

It is long known from laboratory experiments, that failure of rock samples is a time-dependent process. Such brittle creep is thought to play an important role in the seismic cycle of active fault zones [Das and Scholz, 1981; Gomberg, 2001]. To analyze the effect of time-dependency of stress release and stress transfer on failure, I applied a damage mechanics approach to the wellbore scale to investigate time-dependent wellbore failure (Chapter 7). Analogously to observations of time-dependent growth of wellbore breakouts, I demonstrated the evolution of breakout growth with time, both in width and depth. Due to stiffness deterioration with increasing damage, stresses are transferred from damaged elements to the neighboring elements. This dissipates stress peaks and eventually a stable regime is reached. The decrease of breakout growth follows the empirical law of Omori [1894], usually used to describe the declining aftershock activity following a main shock. The decay exponent  $p$  for breakout growth, is slightly smaller than that for natural aftershock sequences. When using the geometries of breakouts to determine the stress tensor magnitudes in the subsurface, e.g. using methods of Haimson and Chang [2002], the temporal growth of breakouts needs to be taken into account.

## 8.2 OUTLOOK

In order to facilitate large-scale application of geothermal power plants with many wells tapping a single large EGS reservoir, seismicity needs to be predictable during the development phases, that include the hydraulic stimulations, necessary for economic reservoir operation. This is a prerequisite for successful application of a traffic light system with adequate options to change the reservoir treatment. Furthermore, proper reservoir management is needed that allows the mitigation of seismicity during long-term operation [Genter et al., 2012; Held et al., 2014], which also includes shut-in of the installation for maintenance purposes [Bönnemann et al., 2010]. Therefore, future research on induced seismicity must concentrate on the improvement of quantitative forecasting methods, to reliably estimate the seismic impact of a reservoir operation [e.g. Hakimhashemi et al., 2014].

The occurrence of largest seismicity following shut-in is still a puzzling phenomenon, with the semblance of lost control. It is therefore

of great importance to develop a sound model for the exact hydro-mechanically coupled processes, that lead to a sudden change in the behavior of seismicity following the singular transition introduced by the shut-in. Only then, adequate means to avoid unwanted seismicity, can be developed.

There is ample evidence for aseismic processes, contributing a large proportion of the productivity-gain through hydraulic stimulation. These are direct indicators such as observed large slip at wellbore walls [Cornet et al., 1997] and indirect indicators such as observations of multiplets distributed along fault zones and accumulating more than 10 cm of slip on single asperities [Bourouis and Bernard, 2007]. Between these seismic asperities, slip has to accumulate aseismically, since no corresponding seismic events have been observed. Furthermore, the 4D tomography by Calo et al. [2011] and the comparison of static stress changes from seismic events (Chapter 4) and total stress changes obtained from stress inversion (Chapter 6) indicate large-scale stress release, incompatible with seismically observed events alone. Therefore, aseismic processes hold the key to optimize the reservoir productivity and simultaneously minimize the seismic footprint of a stimulation. If we succeed to specifically target and trigger aseismic deformation, we will have resolved one major obstacle of the EGS technology.

---

## REFERENCES

---

- Abercrombie, R. E. (1995). Earthquake source scaling relationships from -1 to 5 ML using seismograms recorded at 2.5-km depth. *Journal of Geophysical Research*, 100(B12):24015.
- Aki, K. (1981). A probabilistic synthesis of precursory phenomena. In Simpson, D. and Richards, P., editors, *Earthquake Prediction: An International Review*, pages 566–574. AGU, Washington, DC, USA.
- Amitrano, D. (2003). Brittle-ductile transition and associated seismicity: Experimental and numerical studies and relationship with the b value. *Journal of Geophysical Research*, 108(B1):2044.
- Amitrano, D. and Helmstetter, A. (2006). Brittle creep, damage, and time to failure in rocks. *Journal of Geophysical Research*, 111(B11):B11201.
- Anderson, E. M. (1951). *The dynamics of faulting and dyke formation with applications to Britain*. Oliver and Boyd.
- Anderson, O. L. and Grew, P. C. (1977). Stress corrosion theory of crack propagation with applications to geophysics. *Reviews of Geophysics*, 15(1):77.
- Andersson, J. C., Martin, C. D., and Stille, H. (2009). The Äspö Pillar Stability Experiment: Part II-Rock mass response to coupled excavation-induced and thermal-induced stresses. *International Journal of Rock Mechanics and Mining Sciences*, 46(5):879–895.
- Angelier, J. (1979). Determination of the mean principal directions of stresses for a given fault population. *Tectonophysics*, 56(3-4):T17–T26.
- Atkinson, B. K. (1984). Subcritical Crack Growth in Geological Materials. *Journal of Geophysical Research*, 89(B6):4077–4114.
- Auradou, H., Drazer, G., Hulin, J. P., and Koplik, J. (2005). Permeability anisotropy induced by the shear displacement of rough fracture walls. *Water Resources Research*, 41(9):W09423.
- Båth, M. (1965). Lateral inhomogeneities of the upper mantle. *Tectonophysics*, 2(6):483–514.
- Bachmann, C. E., Wiemer, S., Goertz-Allmann, B. P., and Woessner, J. (2012). Influence of pore-pressure on the event-size distribution of induced earthquakes. *Geophysical Research Letters*, 39(9):L09302.
- Bachmann, C. E., Wiemer, S., Woessner, J., and Hainzl, S. (2011). Statistical analysis of the induced Basel 2006 earthquake sequence: introducing a probability-based monitoring approach for Enhanced Geothermal Systems. *Geophysical Journal International*, 186(2):793–807.
- Baisch, S., Carbon, D., Dannwolf, U., Delacou, B., Devaux, M., Dunand, F., Jung, R., Koller, M., Martin, C., Sartori, M., Secanell, R., and Vörös, R. (2009). Deep Heat Mining Basel - Seismic Risk Analysis. Technical report,

SERIANEX Group, Departement für Wirtschaft, Soziales und Umwelt des Kantons Basel-Stadt, Basel.

- Baisch, S. and Harjes, H.-P. (2003). A model for fluid-injection-induced seismicity at the KTB, Germany. *Geophysical Journal International*, 152:160–170.
- Baisch, S., Vörös, R., Rothert, E., Stang, H., Jung, R., and Schellschmidt, R. (2010). A numerical model for fluid injection induced seismicity at Soultz-sous-Forêts. *International Journal of Rock Mechanics and Mining Sciences*, 47(3):405–413.
- Baisch, S., Weidler, R., Vörös, R., and Jung, R. (2006). A conceptual model for post-injection seismicity at Soultz-sous-Forêts. *GRC Transactions*, 30:601–606.
- Bak, P. and Tang, C. (1989). Earthquakes as a self-organized critical phenomenon. *Journal of Geophysical Research*, 94(B11):15635–15637.
- Baria, R., Garnish, J., Baumgärtner, J., Gerard, A., and Jung, R. (1995). Recent developments in the European HDR research programme at Soultz-sous-Forêts (France). In *World Geothermal Congress*, Florence, Italy.
- Barth, A., Wenzel, F., and Langenbruch, C. (2013). Probability of earthquake occurrence and magnitude estimation in the post shut-in phase of geothermal projects. *Journal of Seismology*, 17(1):5–11.
- Barton, N., Bandis, S., and Bakhtar, K. (1985). Strength, Deformation and Conductivity Coupling of Rock Joints. *International Journal of Rock Mechanics and Mining Sciences & Geomechanics Abstracts*, 22(3):121–140.
- Baud, P. and Meredith, P. G. (1997). Damage accumulation during triaxial creep of Darley Dale sandstone from pore volumometry and acoustic emission. *International Journal of Rock Mechanics and Mining Sciences*, 34(3–4):24.e1–24.e10.
- Biot, M. A. (1941). General theory of three dimensionally consolidation. *Journal of Applied Physics*, 12:155.
- Biot, M. A. (1962). Mechanics of deformation and acoustic propagation in porous media. *Journal of Applied Physics*, 33(4):1482–1498.
- Bommer, J. J., Oates, S., Cepeda, J. M., Lindholm, C., Bird, J., Torres, R., Marroquín, G., and Rivas, J. (2006). Control of hazard due to seismicity induced by a hot fractured rock geothermal project. *Engineering Geology*, 83(4):287–306.
- Bönnemann, C., Schmidt, B., Ritter, J., Gestermann, N., Plenefisch, T., Weigler, U., Schulz, R., Heidbach, O., Erbas, K., Baisch, S., Rothert, E., Hauffe, P., Baumgärtner, J., Hettkamp, T., Rogulic, B., Teza, D., Baria, R., Fritsch, R., Pettitt, W., and Andrews, J. (2010). Das seismische Ereignis bei Landau vom 15. August 2009. Technical report, BGR, Hannover.
- Bott, M. H. P. (1959). The mechanics of oblique slip faulting. *Geological Magazine*, 96(2):109–117.

- Bourouis, S. and Bernard, P. (2007). Evidence for coupled seismic and aseismic fault slip during water injection in the geothermal site of Soultz (France), and implications for seismogenic transients. *Geophysical Journal International*, 169(2):723–732.
- Brace, W. F. and Byerlee, J. D. (1966). Stick-slip as a mechanism for earthquakes. *Science*, 153(3739):990–992.
- Brantut, N., Baud, P., Heap, M., and Meredith, P. G. (2012). Micromechanics of brittle creep in rocks. *Journal of Geophysical Research*, 117(B8):B08412.
- Brantut, N., Heap, M., Meredith, P., and Baud, P. (2013). Time-dependent cracking and brittle creep in crustal rocks: A review. *Journal of Structural Geology*, 52:17–43.
- Brudy, M., Zoback, M. D., Fuchs, K., Rummel, F., and Baumgärtner, J. (1997). Estimation of the complete stress tensor to 8 km depth in the KTB scientific drill holes: Implications for crustal strength. *Journal of Geophysical Research*, 102(B8):18453–18475.
- Bruel, D. (2002). Impact of induced thermal stresses during circulation tests in an engineered fractured geothermal reservoir - Example of the Soultz-sous-Forets European Hot Fractured Rock Geothermal Project, Rhine Graben, France. *Oil & Gas Science and Technology-Revue De L Institut Français Du Pétrole*, 57(5):459–470.
- Brune, J. N. (1970). Tectonic stress and the spectra of seismic shear waves from earthquakes. *Journal of Geophysical Research*, 75(26):4997–5009.
- Burkhard, M. and Grünthal, G. (2009). Seismic source zone characterization for the seismic hazard assessment project PEGASOS by the Expert Group 2 (EG1b). *Swiss Journal of Geosciences*, 102(1):149–188.
- Byerlee, J. D. (1978). Friction of Rocks. *Pure and Applied Geophysics*, 116(4–5):615–626.
- Calo, M., Dorbath, C., Cornet, F. H., and Cuenot, N. (2011). Large-scale aseismic motion identified through 4-D P-wave tomography. *Geophysical Journal International*, 186(3):1295–1314.
- Carter, N., Horseman, S., Russell, J., and Handin, J. (1993). Rheology of rocksalt. *Journal of Structural Geology*, 15(9):1257–1271.
- Catalli, F., Cocco, M., Console, R., and Chiaraluce, L. (2008). Modeling seismicity rate changes during the 1997 Umbria-Marche sequence (central Italy) through a rate- and state-dependent model. *Journal of Geophysical Research*, 113(B11):B11301.
- Catalli, F., Meier, M.-A., and Wiemer, S. (2013). The role of Coulomb stress changes for injection-induced seismicity: The Basel enhanced geothermal system. *Geophysical Research Letters*, 40(1):72–77.
- Célérier, B., Etchecopar, A., Bergerat, F., Vergely, P., Arthaud, F., and Laurent, P. (2012). Inferring stress from faulting: From early concepts to inverse methods. *Tectonophysics*, 581:206–219.
- Charles, R. (1958). The static fatigue of glass. *Journal of Applied Physics*, 29:1549–1560.

- Charléty, J., Cuenot, N., Dorbath, L., Dorbath, C., Haessler, H., and Frogneux, M. (2007). Large earthquakes during hydraulic stimulations at the geothermal site of Soultz-sous-Forêts. *International Journal of Rock Mechanics and Mining Sciences*, 44(8):1091–1105.
- Chen, C.-C., Wang, W.-C., Chang, Y.-F., Wu, Y.-M., and Lee, Y.-H. (2006). A correlation between the b-value and the fractal dimension from the aftershock sequence of the 1999 Chi-Chi, Taiwan, earthquake. *Geophysical Journal International*, 167(3):1215–1219.
- Chen, G., Chenevert, M. E., Sharma, M. M., and Yu, M. (2003). A study of wellbore stability in shales including poroelastic, chemical, and thermal effects. *Journal of Petroleum Science and Engineering*, 38:167–176.
- Chen, X. and Shearer, P. M. (2011). Comprehensive analysis of earthquake source spectra and swarms in the Salton Trough, California. *Journal of Geophysical Research*, 116(B9):B09309.
- Chen, Z., Narayan, S. P., Yang, Z., and Rahman, S. S. (2000). An experimental investigation of hydraulic behaviour of fractures and joints in granitic rock. *International Journal of Rock Mechanics and Mining Sciences*, 37(7):1061–1071.
- Cornet, F. H. (2000). Comment on 'Large-Scale in situ permeability tensor of rocks from induced microseismicity' by S. A. Shapiro, P. Audigane and J.-J. Royer. *Geophysical Journal International*, 140:465–469.
- Cornet, F. H., Bérard, T., and Bourouis, S. (2007). How close to failure is a granite rock mass at a 5 km depth. *International Journal of Rock Mechanics and Mining Sciences*, 44(1):47–66.
- Cornet, F. H., Helm, J., Poitrenaud, H., and Etchecopar, A. (1997). Seismic and Aseismic slips induced by large-scale fluid injections. *Pure and Applied Geophysics*, 150:563–585.
- Coulomb, C. (1773). Application des règles de maxima et minima à quelques problèmes de statique relatifs à l'Architecture. *Mémoires de Mathématiques et de Physiques présentés à l'Académie Royale des Sciences*, 7:343–382.
- Cuenot, N., Charléty, J., Dorbath, L., and Haessler, H. (2006). Faulting mechanisms and stress regime at the European HDR site of Soultz-sous-Forêts, France. *Geothermics*, 35(5-6):561–575.
- Cuenot, N., Dorbath, C., and Dorbath, L. (2008). Analysis of the microseismicity induced by fluid injections at the EGS site of Soultz-sous-Forêts (Alsace, France): Implications for the characterization of the geothermal reservoir properties. *Pure and Applied Geophysics*, 165(5):797–828.
- Cuenot, N., Frogneux, M., Calo, M., and Dorbath, C. (2011). Induced microseismicity monitoring during hydraulic circulations 2008-2011. In *Soultz Geothermal Conference*, Soultz-sous-Forêts, France.
- Darcy, H. (1856). *Les Fontaines de la Ville de Dijon*. Victor Dalmont, Paris.
- Darnet, M., Marquis, G., and Sailhac, P. (2006). Hydraulic stimulation of geothermal reservoirs: fluid flow, electric potential and microseismicity relationships. *Geophysical Journal International*, 166(1):438–444.

- Das, S. and Scholz, C. H. (1981). Theory of time-dependent rupture in the Earth. *Journal of Geophysical Research*, 86(B7):6039–6051.
- Delépine, N., Cuenot, N., Rothert, E., Parotidis, M., Rentsch, S., and Shapiro, S. A. (2004). Characterization of fluid transport properties of the Hot Dry Rock reservoir Soultz-2000 using induced microseismicity. *Journal of Geophysics and Engineering*, 1(1):77–83.
- Detournay, E. and Cheng, A. H. D. (1988). Poroelastic response of a borehole in a non-hydrostatic stress field. *International Journal of Rock Mechanics and Mining Sciences & Geomechanics Abstracts*, 25(3):171–182.
- Dieterich, J. H. (1979). Modeling of rock friction: 1. Experimental results and constitutive equations. *Journal of Geophysical Research*, 84(B5):2161.
- Dieterich, J. H. (1994). A constitutive law for rate of earthquake production and its application to earthquake clustering. *Journal of Geophysical Research*, 99(B2):2601–2618.
- Dorbath, L., Cuenot, N., Genter, A., and Frogneux, M. (2009). Seismic response of the fractured and faulted granite of Soultz-sous-Forêts (France) to 5 km deep massive water injections. *Geophysical Journal International*, 177(2):653–675.
- Dorbath, L., Cuenot, N., and Stein, R. R. (2008). Coulomb stress change by the stimulation of GPK2 and the orientation of the seismicity induced by the stimulation of GPK3. In *EHDRA scientific conference*, Soultz-sous-Forêts, France.
- Dyer, B. C. (2001). Soultz GPK2 stimulation June/July 2000. Seismic monitoring report. Technical report, Semore Seismic.
- Dyer, B. C. (2005). Soultz GPK4 stimulation September 2004 to April 2005. Seismic monitoring report. Technical report, Semore Seismic.
- Dyer, B. C., Baria, R., and Michelet, S. (2004). Soultz GPK3 stimulation and GPK3-GPK2 circulation May to July 2003. Seismic monitoring report. Technical report, Semore Seismic.
- Ellsworth, W. L. (2013). Injection-induced earthquakes. *Science*, 341:1225942.
- Ershaghi, I., Abdassah, D., Bonakdar, M., and Ahmad, S. (1983). Estimation of geothermal brine viscosity. *Journal of Petroleum Technology*, 35(3):621–628.
- Eshelby, J. D. (1957). The determination of the elastic field of an ellipsoidal inclusion, and related problems. *Proceedings of the Royal Society of London. Series A, Mathematical and Physical Sciences*, 241(1226):376–396.
- Evans, K. F., Moriya, H., Niitsuma, H., Jones, R. H., Phillips, W. S., Genter, A., Sausse, J., Jung, R., and Baria, R. (2005). Microseismicity and permeability enhancement of hydrogeologic structures during massive fluid injections into granite at 3 km depth at the Soultz HDR site. *Geophysical Journal International*, 160(1):389–412.
- Evans, K. F., Zappone, A., Kraft, T., Deichmann, N., and Moia, F. (2012). A survey of the induced seismic responses to fluid injection in geothermal and CO<sub>2</sub> reservoirs in Europe. *Geothermics*, 41:30–54.

- Ewy, R. T. (1993). Yield and closure of directional and horizontal wells. *International Journal of Rock Mechanics and Mining Sciences & Geomechanics Abstracts*, 30(7):1061–1067.
- Fabre, G. and Pellet, F. (2006). Creep and time-dependent damage in argillaceous rocks. *International Journal of Rock Mechanics and Mining Sciences*, 43(6):950–960.
- Felzer, K. R. and Brodsky, E. E. (2006). Decay of aftershock density with distance indicates triggering by dynamic stress. *Nature*, 441(7094):735–8.
- Fisher, N. I. (1993). *Statistical analysis of circular data*. Cambridge University Press, Cambridge.
- Fjaer, E., Holt, R. M., Horsrud, P., Raaen, A. M., and Risnes, R. (2008). *Petroleum Related Rock Mechanics*. Elsevier.
- Frohlich, C., Interiors, P., and Unu, T. (1992). Triangle diagrams: ternary graphs to display similarity and diversity of earthquake focal mechanisms. *Physics of the Earth and Planetary Interiors*, 75(1-3):193–198.
- GEISER Project (2013). Geothermal Engineering Integrating Mitigation of Induced Seismicity in Reservoirs. <http://www.geiser-fp7.fr/>.
- Gens, A., Vaunat, J., Garitte, B., and Wileveau, Y. (2007). In situ behaviour of a stiff layered clay subject to thermal loading: observations and interpretation. *Geotechnique*, 57(2):207–228.
- Genter, A., Cuenot, N., Goerke, X., Melchert, B., Sanjuan, B., and Julia Scheiber (2012). Status of the Soultz geothermal project during exploitation between 2010 and 2012. In *Proceedings 37th Workshop on Geothermal Reservoir Engineering, Stanford University*, volume 37, pages 704–715, Stanford, California. Curran Associates, Red Hook, New York.
- Genter, A., Evans, K. F., Cuenot, N., Fritsch, D., and Sanjuan, B. (2010). Contribution of the exploration of deep crystalline fractured reservoir of Soultz to the knowledge of enhanced geothermal systems (EGS). *Comptes Rendus Geoscience*, 342(7-8):502–516.
- Genter, A. and Trainea, H. (1992). Borehole EPS-1, Alsace, France: preliminary geological results from granite core analyses for Hot Dry Rock research. *Scientific Drilling*, 3:205–214.
- Gephart, J. W. and Forsyth, D. W. (1984). An improved method for determining the regional stress tensor using earthquake focal mechanism data: Application to the San Fernando Earthquake Sequence. *Journal of Geophysical Research*, 89(B11):9305.
- Gérard, A., Baumgärtner, J., Baria, R., and Jung, R. (1997). An attempt towards a conceptual model derived from 1993–1996 hydraulic operations at Soultz. In *NEDO International Geothermal Symposium*, NEDO, Sendai, Japan.
- Ghassemi, A., Tarasovs, S., and Cheng, A. H. D. (2007). A 3-D study of the effects of thermomechanical loads on fracture slip in enhanced geothermal reservoirs. *International Journal of Rock Mechanics and Mining Sciences*, 44(8):1132–1148.

- Goertz-Allmann, B. P., Goertz, A., and Wiemer, S. (2011). Stress drop variations of induced earthquakes at the Basel geothermal site. *Geophys. Res. Lett.*, 38(9):L09308.
- Goertz-Allmann, B. P. and Wiemer, S. (2013). Geomechanical modeling of induced seismicity source parameters and implications for seismic hazard assessment. *Geophysics*, 78(1):KS25–KS39.
- Gomberg, J. (2001). The failure of earthquake failure models. *Journal of Geophysical Research-Solid Earth*, 106(B8):16253–16263.
- Gomberg, J., Beeler, N., and Blanpied, M. (2000). On rate-state and Coulomb failure models. *Journal of Geophysical Research*, 105(B4):7857.
- Gran, J. D., Rundle, J. B., and Turcotte, D. L. (2012). A possible mechanism for aftershocks: time-dependent stress relaxation in a slider-block model. *Geophysical Journal International*, 191(2):459–466.
- Gross, D. and Seelig, T. (2011). *Bruchmechanik: Mit einer Einführung in die Mikromechanik*. Springer.
- Gutenberg, B. and Richter, C. F. (1954). *Seismicity of the Earth and Associated Phenomena*. Princeton University Press, 2nd edition.
- Haimson, B. C. (2007). Micromechanisms of borehole instability leading to breakouts in rocks. *International Journal of Rock Mechanics and Mining Sciences*, 44(2):157–173.
- Haimson, B. C. and Chang, C. (2002). True triaxial strength of the KTB amphibolite under borehole wall conditions and its use to estimate the maximum horizontal in situ stress. *Journal of Geophysical Research*, 107(B10):2257.
- Hainzl, S. (2004). Seismicity patterns of earthquake swarms due to fluid intrusion and stress triggering. *Geophysical Journal International*, 159(3):1090–1096.
- Hainzl, S. and Fischer, T. (2002). Indications for a successively triggered rupture growth underlying the 2000 earthquake swarm in Vogtland/NW Bohemia. *Journal of Geophysical Research*, 107(B12):2338.
- Hakimhashemi, A. H., Schoenball, M., Heidbach, O., Zang, A., and Grünthal, G. (2014). Forward Modelling of Seismicity Rate Changes in Georeservoirs with a Hybrid Geomechanical-Statistical Prototype Model. *Geothermics*, in press,(doi: 10.1016/j.geothermics.2014.01.001).
- Hardebeck, J. L. (2012). Coseismic and postseismic stress rotations due to great subduction zone earthquakes. *Geophysical Research Letters*, 39(21):L21313.
- Hardebeck, J. L. and Michael, A. J. (2006). Damped regional-scale stress inversions: Methodology and examples for southern California and the Coalinga aftershock sequence. *Journal of Geophysical Research*, 111(B11):B11310.
- Hardebeck, J. L., Nazareth, J. J., and Hauksson, E. (1998). The static stress change triggering model: Constraints from two southern California aftershock sequences. *Journal of Geophysical Research*, 103(B10):24427–24437.

- Häring, M. O., Schanz, U., Ladner, F., and Dyer, B. C. (2008). Characterisation of the Basel 1 enhanced geothermal system. *Geothermics*, 37(5):469–495.
- Hasegawa, A., Yoshida, K., Asano, Y., Okada, T., Iinuma, T., and Ito, Y. (2012). Change in stress field after the 2011 great Tohoku-Oki earthquake. *Earth and Planetary Science Letters*, 355:231–243.
- Healy, J. H., Rubey, W. W., Griggs, D. T., and Raleigh, C. B. (1968). The Denver earthquakes. *Science*, 161(3848):1301–1310.
- Heap, M., Baud, P., Meredith, P. G., Bell, A. F., and Main, I. G. (2009). Time-dependent brittle creep in Darley Dale sandstone. *Journal of Geophysical Research*, 114(B7):B07203.
- Heap, M., Baud, P., Meredith, P. G., Vinciguerra, S., Bell, A. F., and Main, I. G. (2011). Brittle creep in basalt and its application to time-dependent volcano deformation. *Earth and Planetary Science Letters*, 307(1-2):71–82.
- Heap, M., Faulkner, D. R., Meredith, P. G., and Vinciguerra, S. (2010). Elastic moduli evolution and accompanying stress changes with increasing crack damage: implications for stress changes around fault zones and volcanoes during deformation. *Geophysical Journal International*, 183(1):225–236.
- Heidbach, O., Tingay, M., Barth, A., Reinecker, J., Kurfeß, D., and Müller, B. I. (2010). Global crustal stress pattern based on the World Stress Map database release 2008. *Tectonophysics*, 482(1-4):3–15.
- Held, S., Genter, A., Kohl, T., Kölbel, T., Sausse, J., and Schoenball, M. (2014). Economic evaluation of geothermal reservoir performance through modeling the complexity of the operating EGS in Soultz-sous-Forêts. *Geothermics*, 51:270–280.
- Helmstetter, A., Kagan, Y. Y., and Jackson, D. D. (2005). Importance of small earthquakes for stress transfers and earthquake triggering. *Journal of Geophysical Research*, 110(B5):B05So8.
- Hiramatsu, Y. and Oka, Y. (1968). Determination of the stress in rock unaffected by boreholes or drifts, from measured strains or deformations. *International Journal of Rock Mechanics and Mining Sciences & Geomechanics Abstracts*, 5(4):337–353.
- Hooijkaas, G. R., Genter, A., and Dezayes, C. (2006). Deep-seated geology of the granite intrusions at the Soultz EGS site based on data from 5 km-deep boreholes. *Geothermics*, 35(5-6):484–506.
- Horálek, J., Jechumtállová, Z., Dorbath, L., and Šílený, J. (2010). Source mechanisms of micro-earthquakes induced in a fluid injection experiment at the HDR site Soultz-sous-Forêts (Alsace) in 2003 and their temporal and spatial variations. *Geophysical Journal International*, 181(3):1547–1565.
- Hubbert, M. K. and Rubey, W. W. (1959). Role of fluid pressure in mechanics of overthrust faulting. *Geological Society of America Bulletin*, 70(2):115.
- IEA (2011). *Technology Roadmap: Geothermal Heat and Power*. IEA Technology Roadmaps. OECD Publishing.

- Jaeger, J. C., Cook, N. G. W., and Zimmerman, R. W. (2007). *Fundamentals of Rock Mechanics*. Blackwell Publishing.
- Jennejohn, D., Hines, B., Gawell, K., and Blodgett, L. (2012). Geothermal: International Market Overview Report. Technical report, Geothermal Energy Association, Washington D.C., USA.
- Jones, R. H., Beauch, A., Jupe, A., Fabriol, H., and Dyer, B. C. (1995). Imaging induced microseismicity during the 1993 injection tests at Soultz-sous-Forêts, France. In *World Geothermal Congress*, Florence, Italy.
- Jost, M. L., Büßelberg, T., and Harjes, H.-P. (1998). Source parameters of injection-induced microearthquakes at 9 km depth at the KTB deep drilling site, Germany. *Bulletin of the Seismological Society of America*, 88:815–832.
- Jung, R. (2013). EGS - goodbye or back to the future. In Jeffrey, R., editor, *Effective and Sustainable Hydraulic Fracturing*. InTech.
- Kanamori, H. (1977). The energy release in great earthquakes. *Journal of Geophysical Research*, 82(20):2981–2987.
- Kanamori, H. (2003). Earthquake prediction: An overview. In *International Handbook of Earthquake and Engineering Seismology*, volume 81, pages 1205–1216. Academic Press.
- Kanamori, H. and Anderson, D. L. (1975). Theoretical basis of some empirical relations in seismology. *Bulletin of the Seismological Society of America*, 65(5):1073–1095.
- Kanamori, H. and Brodsky, E. E. (2004). The physics of earthquakes. *Reports on Progress in Physics*, 67(8):1429–1496.
- Kemeny, J. and Cook, N. G. W. (1986). Effective moduli, nonlinear deformation and strength of a cracked elastic solid. *International Journal of Rock Mechanics and Mining Sciences & Geomechanics Abstracts*, 23(2):107–118.
- Kessels, W. (1989). Observation and interpretation of time-dependent behaviour of borehole stability in the Continental Deep Drilling pilot borehole. *Scientific Drilling*, 1:127–134.
- King, G. C. P., Stein, R. S., and Lin, J. (1994). Static stress changes and the triggering of earthquakes. *Bulletin of the Seismological Society of America*, 84(3):935–953.
- Kirsch, G. (1898). Die Theorie der Elastizität und die Bedürfnisse der Festigkeitslehre. *Zeitschrift des Vereins Deutscher Ingenieure*, 42:797–807.
- Klein, F. W. (1978). Hypocenter location program HYPOINVERSE, Part1: user guide to version 1,2,3 and 4. Technical report, USGS.
- Koh, J., Roshan, H., and Rahman, S. S. (2011). A numerical study on the long term thermo-poroelastic effects of cold water injection into naturally fractured geothermal reservoirs. *Computers and Geotechnics*, 38(5):669–682.
- Kohl, T., Bächler, D., and Rybach, L. (2000). Steps towards a comprehensive thermo-hydraulic analysis of the HDR test site Soultz-sous-Forêts. In *World Geothermal Congress*, pages 2671–2676.

- Kohl, T., Baujard, C., and Mégel, T. (2006). Conditions for mechanical re-stimulation of GPK4. In *EHDRA scientific conference*, page 6, Soultz-sous-Forêts, France.
- Kohl, T., Evans, K. F., Hopkirk, R. J., Jung, R., and Rybach, L. (1997). Observation and simulation of non-Darcian flow transients in fractured rock. *Water Resources Research*, 33(3):407–418.
- Kohl, T. and Mégel, T. (2007). Predictive modeling of reservoir response to hydraulic stimulations at the European EGS site Soultz-sous-Forêts. *International Journal of Rock Mechanics and Mining Sciences*, 44(8):1118–1131.
- Kranz, R. L. (1980). The effects of confining pressure and stress difference on static fatigue of granite. *Journal of Geophysical Research*, 85(B4):1854–1866.
- Kranz, R. L., Harris, W. J., and Carter, N. L. (1982). Static fatigue of granite at 200 C. *Geophysical Research Letters*, 9(1):1–4.
- Kurashige, M. (1989). A thermoelastic theory of fluid-filled porous materials. *International Journal of Solids and Structures*, 25(9):1039–1052.
- Langenbruch, C., Dinske, C., and Shapiro, S. A. (2011). Inter event times of fluid induced earthquakes suggest their Poisson nature. *Geophysical Research Letters*, 38(21):L21302.
- Langenbruch, C. and Shapiro, S. A. (2010). Decay rate of fluid-induced seismicity after termination of reservoir stimulations. *Geophysics*, 75(6):MA53–MA62.
- Lay, T. and Wallace, T. C. (1995). *Modern Global Seismology*. Academic Press.
- Lee, M. and Haimson, B. C. (1993). Laboratory study of borehole break-outs in Lac du Bonnet granite: a case of extensile failure mechanism. *International Journal of Rock Mechanics and Mining Sciences & Geomechanics Abstracts*, 30(7):1039–1045.
- Lockner, D. A. (1993). Room temperature creep in saturated granite. *Journal of Geophysical Research*, 98(B1):475–487.
- Lockner, D. A. (1998). A generalized law for brittle deformation of Westerly granite. *Journal of Geophysical Research-Solid Earth*, 103(B3):5107–5123.
- MacInnes, B. T., Gusman, A. R., LeVeque, R. J., and Tanioka, Y. (2013). Comparison of earthquake source models for the 2011 Tohoku event using tsunami simulations and near-field observations. *Bulletin of the Seismological Society of America*, 103(2B):1256–1274.
- Madariaga, R. (1976). Dynamics of an expanding circular fault. *Bulletin of the Seismological Society of America*, 66(3):639–666.
- Majer, E. L., Baria, R., Stark, M., Oates, S., Bommer, J. J., Smith, B., and Asanuma, H. (2007). Induced seismicity associated with enhanced geothermal systems. *Geothermics*, 36(3):185–222.
- Marquis, G., Darnet, M., Sailhac, P., Singh, A. K., and Gérard, A. (2002). Surface electric variations induced by deep hydraulic stimulation: An example from the Soultz HDR site. *Geophysical Research Letters*, 29(14):1662.

- Martínez-Garzón, P., Bohnhoff, M., Kwiatek, G., and Dresen, G. (2013). Stress tensor changes related to fluid injection at The Geysers geothermal field, California. *Geophysical Research Letters*, 40(11):2596–2601.
- Masuda, K. (2001). Effects of water on rock strength in a brittle regime. *Journal of Structural Geology*, 23:1653–1657.
- Maury, J., Cornet, F. H., and Dorbath, L. (2013). A review of methods for determining stress fields from earthquakes focal mechanisms; Application to the Sierentz 1980 seismic crisis (Upper Rhine graben). *Bulletin de la Societe Geologique de France*, 184(4-5):319–334.
- Maxwell, S. C., Jones, M., Parker, R., Leaney, S., Mack, M., Dorvall, D., Amico, D. D., Logel, J., Anderson, E., and Hammermaster, K. (2010). Fault activation during hydraulic fracturing. In *72nd EAGE Conference, Barcelona*, page 5.
- McClure, M. W. and Horne, R. N. (2010). Numerical and analytical modeling of the mechanisms of induced seismicity during fluid injection. *GRC Transactions*, 34:381–396.
- McClure, M. W. and Horne, R. N. (2012). Investigation of injection-induced seismicity using a coupled fluid flow and rate/state friction model. *Geophysics*, 76:WC183.
- McTigue, D. F. (1986). Thermoelastic Response of Fluid-Saturated Porous Rock. *Journal of Geophysical Research*, 91(B9):9533–9542.
- Meller, C., Genter, A., and Kohl, T. (2014). The application of a neural network to map clay zones in crystalline rock. *Geophysical Journal International*, 196(2):837–849.
- Meller, C., Kohl, T., and Gaucher, E. (2012). Approach for determination of the failure probability of fractures at the Soultz-Sous-Forêts EGS Project. In *Proceedings 37th Workshop on Geothermal Reservoir Engineering, Stanford University*, volume 37, pages 843–850. Curran Associates, Red Hook, New York.
- Mena, B., Wiemer, S., and Bachmann, C. (2013). Building robust models to forecast the induced seismicity related to geothermal reservoir enhancement. *Bulletin of the Seismological Society of America*, 103(1):383–393.
- Menke, W. (2012). *Geophysical Data Analysis: Discrete Inverse Theory*. Academic Press, 3rd edition.
- Michael, A. J. (1984). Determination of stress from slip data: Faults and folds. *Journal of Geophysical Research*, 89(B13):11517.
- Michael, A. J. (1987a). Stress rotation during the Coalinga Aftershock Sequence. *Journal of Geophysical Research*, 92(B8):7963.
- Michael, A. J. (1987b). Use of focal mechanisms to determine stress: A control study. *Journal of Geophysical Research*, 92(B1):357.
- Michelet, S. (2002). *Rock site Source Parameter Analysis and Interpretation for Microseismic Data from the Soultz-sous-Forêts Hot Dry Rock Site*. PhD thesis, Université Louis Pasteur, Strasbourg.

- Mohr, C. O. (1914). *Abhandlungen aus dem Gebiete der Technischen Mechanik*. Ernst und Sohn, Berlin, 2nd edition.
- Moore, J. C., Chang, C., McNeill, L., Thu, M. K., Yamada, Y., and Huftile, G. (2011). Growth of borehole breakouts with time after drilling: Implications for state of stress, NanTroSEIZE transect, SW Japan. *Geochemistry Geophysics Geosystems*, 12:Q04D09.
- Moriya, H. (2003). Multiplet-Clustering Analysis Reveals Structural Details within the Seismic Cloud at the Soultz Geothermal Field, France. *Bulletin of the Seismological Society of America*, 93(4):1606–1620.
- Narteau, C., Byrdina, S., Shebalin, P., and Schorlemmer, D. (2009). Common dependence on stress for the two fundamental laws of statistical seismology. *Nature*, 462(7273):642–5.
- Norton, F. H. (1929). *The Creep of Steel at High Temperatures*. McGraw-Hill.
- Nowacki, W. (1986). *Thermoelasticity*. Pergamon Press, Oxford, 2nd edition.
- Nur, A. and Booker, J. R. (1972). Aftershocks Caused by Pore Fluid Flow? *Science*, 175:885–887.
- Okada, Y. (1992). Internal deformation due to shear and tensile faults in a half-space. *Bulletin of the Seismological Society of America*, 82(2):1018–1040.
- Omori, F. (1894). On the aftershocks of earthquakes. *Journal of the College of Science, Imperial University of Tokyo*, 7:111–200.
- Orlecka-Sikora, B., Papadimitriou, E. E., and Kwiatek, G. (2009). A study of the interaction among mining-induced seismic events in the Legnica-Glogow Copper District, Poland. *Acta Geophysica*, 57(2):413–434.
- Palciauskas, V. V. and Domenico, P. A. (1982). Characterization of drained and undrained response of thermally loaded repository rocks. *Water Resources Research*, 18(2):281–290.
- Phillips, W., Rutledge, J., House, L., and Fehler, M. (2002). Induced microearthquake patterns in hydrocarbon and geothermal reservoirs: Six case studies. *Pure and Applied Geophysics*, 159(1):345–369.
- Prejean, S. G., Hill, D. P., Brodsky, E. E., Hough, S. E., Johnston, M. J. S., Malone, S. D., Oppenheimer, D. H., Pitt, A. M., and Richards-Dinger, K. B. (2004). Remotely triggered seismicity on the United States west coast following the M-W 7.9 Denali fault earthquake. *Bulletin of the Seismological Society of America*, 94(6):S348–S359.
- Raleigh, C. B., Healy, J. H., and Bredehoeft, J. D. (1976). An experiment in earthquake control at Rangely, Colorado. *Science*, 191(4233):1230–1237.
- Rice, J. R. and Cleary, M. P. (1976). Some basic stress diffusion solutions for fluid-saturated elastic porous media with compressible constituents. *Reviews of Geophysics and Space Physics*, 14(2):227–241.
- Rivera, L. and Cisternas, A. (1990). Stress tensor and fault plane solutions for a population of earthquakes. *Bulletin of the Seismological Society of America*, 80(3):600–614.

- Rudnicki, J. W. (1986). Fluid mass sources and point forces in linear elastic diffusive solids. *Mechanics of Materials*, 5(1986):383–393.
- Ruina, A. (1983). Slip instability and state variable friction laws. *Journal of Geophysical Research*, 88(B12):10359.
- Rutqvist, J. (2011). Status of the TOUGH-FLAC simulator and recent applications related to coupled fluid flow and crustal deformations. *Computers and Geosciences*, 37(6):739–750.
- Rutqvist, J. and Stephansson, O. (2003). The role of hydromechanical coupling in fractured rock engineering. *Hydrogeology Journal*, 11(1):7–40.
- Rutter, E. H. (1976). Kinetics of rock deformation by pressure solution. *Philosophical Transactions of the Royal Society of London Series a-Mathematical Physical and Engineering Sciences*, 283(1312):203–219.
- Sanjuan, B., Pinault, J.-L., Rose, P., Gérard, A., Brach, M., Braibant, G., Crouzet, C., Foucher, J.-C., Gautier, A., and Touzelet, S. (2006). Tracer testing of the geothermal heat exchanger at Soultz-sous-Forêts (France) between 2000 and 2005. *Geothermics*, 35(5-6):622–653.
- Sausse, J., Dezayes, C., Dorbath, L., Genter, A., and Place, J. (2010). 3D model of fracture zones at Soultz-sous-Forêts based on geological data, image logs, induced microseismicity and vertical seismic profiles. *Comptes Rendus Geoscience*, 342(7-8):531–545.
- Schindler, M., Nami, P., Schellschmidt, R., Teza, D., and Tischner, T. (2008). Correlation of hydraulic and seismic observations during stimulation experiments in the 5 km deep crystalline reservoir at Soultz. In *EHDRA scientific conference*, page 8, Soultz-sous-Forêts, France.
- Schoenball, M., Baujard, C., Kohl, T., and Dorbath, L. (2012). The role of triggering by static stress transfer during geothermal reservoir stimulation. *Journal of Geophysical Research*, 117(B9):B09307.
- Schoenball, M. and Kohl, T. (2013). The peculiar shut-in behavior of the well GPK2 at Soultz-sous-Forêts. *GRC Transactions*, 37:217–220.
- Schoenball, M., Müller, T. M., Müller, B. I., and Heidbach, O. (2010). Fluid-induced microseismicity in pre-stressed rock masses. *Geophysical Journal International*, 180(2):813–819.
- Schoenball, M., Selzer, M., Kühnle, N., Nestler, B., Schmittbuhl, J., and Kohl, T. (2013). Flow anisotropy in sheared fractures with self-affine surfaces. In *European Geothermal Congress*, pages PS2–05.
- Scholz, C. H. (1968). Mechanism of creep in brittle rock. *Journal of Geophysical Research*, 73(10):3295.
- Scholz, C. H. (2002). *The Mechanics of Earthquakes and Faulting*. Cambridge University Press.
- Schorlemmer, D., Wiemer, S., and Wyss, M. (2005). Variations in earthquake-size distribution across different stress regimes. *Nature*, 437(7058):539–542.

- Seeber, L. and Armbruster, J. (2000). Earthquakes as beacons of stress change. *Nature*, 407(6800):69–72.
- Segall, P. (2010). *Earthquake and Volcano Deformation*. Princeton University Press.
- Segall, P. and Fitzgerald, S. D. (1998). A note on induced stress changes in hydrocarbon and geothermal reservoirs. *Tectonophysics*, 289(1-3):117–128.
- Shapiro, S. A., Audigane, P., and Royer, J.-J. (1999). Large-scale in situ permeability tensor of rocks from induced microseismicity. *Geophysical Journal International*, 137(2):207–213.
- Shapiro, S. A., Rothert, E., Rath, V., and Rindschwentner, J. (2002). Characterization of fluid transport properties of reservoirs using induced microseismicity. *Geophysics*, 67(1):212–220.
- Shcherbakov, R., Turcotte, D. L., and Rundle, J. B. (2004). A generalized Omori's law for earthquake aftershock decay. *Geophysical Research Letters*, 31(11):L11613.
- Shearer, P. M. (2009). *Introduction to Seismology*. Cambridge University Press.
- Sibson, R. H. (1974). Frictional constraints on thrust, wrench and normal faults. *Nature*, 249:542–544.
- Simpson, D. W. (1976). Seismicity changes associated with reservoir loading. *Engineering Geology*, 10(2):123–150.
- Simulia Inc. (2012). Abaqus Version 6.11, Documentation.
- Snow, D. (1965). *A parallel plate model of fractured permeable media*. PhD thesis, Berkeley, California.
- Stein, R., Barka, A., and Dieterich, J. H. (1997). Progressive failure on the North Anatolian fault since 1939 by earthquake stress triggering. *Geophysical Journal International*, 123(3):594–604.
- Stjern, G., Agle, A., and Horsrud, P. (2003). Local rock mechanical knowledge improves drilling performance in fractured formations at the Heidrun field. *Journal of Petroleum Science and Engineering*, 38(3-4):83–96.
- Talwani, P. and Acree, S. (1984). Pore pressure diffusion and the mechanism of reservoir-induced seismicity. *Pure and Applied Geophysics*, 122:947–965.
- Tembe, S., Lockner, D., and Wong, T.-F. (2009). Constraints on the stress state of the San Andreas Fault with analysis based on core and cuttings from San Andreas Fault Observatory at Depth (SAFOD) drilling phases 1 and 2. *Journal of Geophysical Research*, 114(B11):1–21.
- Terakawa, T., Miller, S. A., and Deichmann, N. (2012). High fluid pressure and triggered earthquakes in the enhanced geothermal system in Basel, Switzerland. *Journal of Geophysical Research*, 117(B7):B07305.
- Terzaghi, K. (1936). The shearing resistance of saturated soils and the angle between planes of shear. In *Proceedings of the First International Conference on Soil Mechanics and Foundation Engineering*, pages 54–56. Harvard University Press, Cambridge, Massachusetts.

- Terzaghi, R. (1965). Sources of Error in Joint Surveys. *Geotechnique*, 15(3):287–304.
- Toda, S. and Stein, R. S. (2003). Toggling of seismicity by the 1997 Kagoshima earthquake couplet: A demonstration of time-dependent stress transfer. *Journal of Geophysical Research*, 108(B12):2567.
- Toda, S., Stein, R. S., and Sagiya, T. (2002). Evidence from the AD 2000 Izu islands earthquake swarm that stressing rate governs seismicity. *Nature*, 419(6902):58–61.
- Toda, S., Stein, R. S., Sevilgen, V., and Lin, J. (2011). Coulomb 3.3 Graphic-rich deformation and stress-change software for earthquake, tectonic, and volcano research and teaching - user guide. Technical report, U.S. Geological Survey Open-File Report 2011-1060.
- Townend, J. and Zoback, M. (2000). How faulting keeps the crust strong. *Geology*, 28:399–402.
- Triantafyllidis, T., Kreuter, H., Mutschler, T., Schoenball, M., Tembe, S., Rübel, S., Osan, C., Balthasar, K., Wenke, A., and Sperber, A. (2010). Reduzierung der geologisch bedingten bohrtechnischen Risiken Bohrlochstabilität in tertiären Tonsteinfolgen im Oberrheingraben. Technical report, Grant no. 0327599, Institute of Soil Mechanics and Rock Mechanics, Karlsruhe Institute of Technology.
- Tsang, C.-F. (1991). Coupled hydromechanical-thermochemical processes in rock fractures. *Reviews of Geophysics*, 29(4):537–551.
- Utsu, T., Ogata, Y., and Matsuura, R. S. (1995). The centenary of the Omori formula for a decay law of aftershock activity. *Journal of Physics of the Earth*, 43(1):1–33.
- Valley, B. C. (2007). *The relation between natural fracturing and stress heterogeneities in deep-seated crystalline rocks at Soultz-sous-Forêts (France)*. PhD thesis, ETH Zürich, Zurich, Switzerland.
- Vernik, L., Zoback, M. D., and Brady, M. (1992). Methodology and application of the wellbore breakout analysis in estimating the maximum horizontal stress magnitude in the KTB pilot hole. *Scientific Drilling*, 3:161–169.
- Wang, H. F. (2000). *Theory of Linear Poroelasticity with Application to Geomechanics and Hydrogeology*. Princeton University Press.
- Wang, R., Lorenzo-Martín, F., and Roth, F. (2003). Computation of deformation induced by earthquakes in a multi-layered elastic crust – FORTRAN programs EDGRN/EDCMP. *Computers and Geosciences*, 29(2):195–207.
- Wang, R., Lorenzo-Martín, F., and Roth, F. (2006). PSGRN/PSCMP - a new code for calculating co- and post-seismic deformation, geoid and gravity changes based on the viscoelastic-gravitational dislocation theory. *Computers and Geosciences*, 32(4):527–541.
- Wang, Y. L. and Papamichos, E. (1994). Conductive heat flow and thermally induced fluid flow around a well bore in a poroelastic medium. *Water Resources Research*, 30(12):3375–3384.

- Weidler, R., Gérard, A., Baria, R., Baumgärtner, J., and Jung, R. (2002). Hydraulic and micro-seismic results of a massive stimulation test at 5 km depth at the European Hot-Dry-Rock test site, Soultz, France. In *Twenty-Seventh Workshop on Geothermal Reservoir Engineering*, volume 27, pages 95–100. Curran Associates, Red Hook, New York.
- Wiederhorn, S. M. and Bolz, L. H. (1970). Stress corrosion and static fatigue of glass. *Journal of The American Ceramic Society*, 50:543–548.
- Wiemer, S. (2001). A software package to analyze seismicity: ZMAP. *Seismological Research Letters*, 72(3):373–382.
- Willis-Richards, J., Watanabe, K., and Takahashi, H. (1996). Progress toward a stochastic rock mechanics model of engineered geothermal systems. *Journal of Geophysical Research-Solid Earth*, 101(B8):17481–17496.
- Witherspoon, P. A., Wang, J. S. Y., Iwai, K., and Gale, J. E. (1980). Validity of Cubic Law for fluid flow in a deformable rock fracture. *Water Resources Research*, 16(6):1016–1024.
- Xiong, X., Shan, B., Zheng, Y., and Wang, R. (2010). Stress transfer and its implication for earthquake hazard on the Kunlun Fault, Tibet. *Tectonophysics*, 482(1-4):216–225.
- Xu, T., Tang, C., Zhao, J., Li, L., and Heap, M. (2012). Modelling the time-dependent rheological behaviour of heterogeneous brittle rocks. *Geophysical Journal International*, 189(3):1781–1796.
- Yamashita, T. (1998). Simulation of seismicity due to fluid migration in a fault zone. *Geophysical Journal International*, 132(3):674–686.
- Zang, A. and Stephansson, O. (2010). *Stress Field of the Earth's Crust*. Springer.
- Zang, A., Yoon, J. S., Stephansson, O., and Heidbach, O. (2013). Fatigue hydraulic fracturing by cyclic reservoir treatment enhances permeability and reduces induced seismicity. *Geophysical Journal International*, 195(2):1282–1287.
- Zimmerman, R. W. (2000). Coupling in poroelasticity and thermoelasticity. *International Journal of Rock Mechanics and Mining Sciences*, 37(1-2):79–87.
- Zoback, M. D. (2010). *Reservoir Geomechanics*. Cambridge University Press.
- Zoback, M. D., Barton, C. A., Brady, M., Castillo, D. A., Finkbeiner, T., Grolimund, B. R., Moos, D. B., Peska, P., Ward, C. D., and Wiprut, D. J. (2003). Determination of stress orientation and magnitude in deep wells. *International Journal of Rock Mechanics and Mining Sciences*, 40(7-8):1049–1076.
- Zoback, M. D. and Harjes, H.-P. (1997). Injection induced earthquakes and the crustal stress at 9 km depth at the KTB deep drilling site, Germany. *Journal of Geophysical Research*, 1002:18477–18492.
- Zoback, M. D., Moos, D., Mastin, L., and Anderson, R. N. (1985). Well bore breakouts and in situ stress. *Journal of Geophysical Research*, 90(B7):5523–5530.

---

## DECLARATION OF AUTHORSHIP

---

### *Study 1: Static Stress Transfer during Reservoir Stimulation (Chapter 4)*

*Citation:*

M. Schoenball, C. Baujard, T. Kohl and L. Dorbath, (2012), The role of triggering by static stress transfer during geothermal reservoir stimulation, *Journal of Geophysical Research*, 117, B09307, doi:10.1029/2012JB009304.

The first study presented in Chapter 4 was conducted under the framework of the GEISER Project [2013] in a collaboration with Ecole et observatoire des sciences de la terre (EOST), Université de Strasbourg, France and Geowatt AG, Zürich, Switzerland. In this study I developed the method to partition the slip distribution of circular fault planes by a summation of rectangles. I adapted the code EDCMP [Wang et al., 2003] to the static stress transfer problem and used on the dataset of focal mechanisms of the GPK2 stimulation, provided by L. Dorbath. I conducted all the computations, interpreted the results and wrote the manuscript.

### *Study 2: Peculiar shut-in behavior of GPK2 (Chapter 5)*

*Citation:*

Schoenball, M. and Kohl, T. (2013). The peculiar shut-in behavior of the well GPK2 at Soultz-sous-Forêts. *GRC Transactions*, 37:217-220.

The second short chapter is the result of a study preliminary to the next study on stress inversion. In this study I performed analysis to highlight the migration trend of seismicity during the post-injection period. I interpreted the results and wrote the manuscript.

*Study 3: Change of stress during reservoir stimulation (Chapter 6)*

*Citation:*

M. Schoenball, L. Dorbath, E. Gaucher, J. F. Wellmann and T. Kohl, Change of stress regime during geothermal reservoir stimulation, *Geophysical Research Letters*, 41, doi:10.1002/2013GL058514.

This study was carried out partly while on my research visit to CSIRO Earth Science and Resources Engineering, Perth, Australia, leading to a collaboration with J. F. Wellmann. It is based on the same dataset provided of focal mechanisms provided by L. Dorbath. In this study I performed the analysis of temporal changes of faulting type. Under the guidance of J. F. Wellmann, I developed the procedure for identification of the fault plane among the two nodal planes based on structural information of the reservoir. I conducted the different stress inversions applying the SATSI code [Hardebeck and Michael, 2006], interpreted the results and wrote the manuscript.

*Study 4: Brittle creep as mechanism for time-delayed wellbore failure (Chapter 7)*

*Citation:*

M. Schoenball, D. P. Sahara, T. Kohl, (2013), Time-dependent brittle creep as mechanism for time-delayed wellbore failure, *International Journal of Rock Mechanics and Mining Sciences*, in press, doi:10.1016/j.ijrmms.2014.05.012.

The study was carried out as part of the project »Reduzierung der geologisch bedingten bohrtechnischen Risiken – Bohrlochstabilität in tertiären Tonsteinfolgen im Oberrheingraben als Hindernis für die Erschließung geothermischer Reservoirs« at Institute of Soil Mechanics and Rock Mechanics at Karlsruhe Institute of Technology, funded by the Federal Ministry for the Environment, Nature Conservation and Nuclear Safety under grant agreement number 0327599. I developed the finite element simulator using the software Abaqus. I implemented the time-dependent behavior using a Fortran subroutine and conducted the numerical simulations. I interpreted the results using observations performed at the KTB by Kessels [1989] and by applying Omori's law. Finally, I wrote the manuscript.

PEER-REVIEWED PUBLICATIONS

D.P. Sahara, M. Schoenball, T. Kohl, B.I.R. Müller, Impact of fracture networks on borehole breakout heterogeneities in crystalline rock, *International Journal of Rock Mechanics and Mining Sciences*, submitted.

C. Baujard, M. Schoenball, T. Kohl and L. Dorbath, The use of the hydraulic energy as a proxy for Mmax prediction during stimulation and operation of geothermal reservoirs, *Geothermics*, submitted.

M. Schoenball, D.P. Sahara, T. Kohl, Time-dependent brittle creep as mechanism for time-delayed wellbore failure, *International Journal of Rock Mechanics and Mining Sciences*, in press, doi:10.1016/j.ijrmms.2014.05.012.

A.H. Hakimhashemi, M. Schoenball, O. Heidbach, A. Zang and G. Grünthal, (2014), Forward Modelling of Seismicity Rate Changes in Georeservoirs with a Hybrid Geomechanical-Statistical Prototype Model, *Geothermics*, in press, doi:10.1016/j.geothermics.2014.01.001.

S. Held, A. Genter, T. Kohl, T. Kölbel, J. Sausse, M. Schoenball, (2014), Economic evaluation of geothermal reservoir performance through modeling the complexity of an operating EGS, *Geothermics*, 51, 270-280, doi:10.1016/j.geothermics.2014.01.001.

M. Schoenball, L. Dorbath, E. Gaucher, J. F. Wellmann and T. Kohl, (2014), Change of stress regime during geothermal reservoir stimulation, *Geophysical Research Letters*, 41, doi:10.1002/2013GL058514.

M. Schoenball, C. Baujard, T. Kohl and L. Dorbath, (2012), The role of triggering by static stress transfer during geothermal reservoir stimulation, *Journal of Geophysical Research*, 117, B09307, doi:10.1029/2012JB009304.

M. Schoenball, T.M. Müller, B.I.R. Müller and O. Heidbach (2010). Fluid-induced microseismicity in pre-stressed rock masses. *Geophysical Journal International*, 180, 813-819, doi:10.1111/j.1365-246X.2009.04443.x.

M. Kronberger, P. Teutsch, B. Alessi, M. Steine, L. Ferrero, K. Graczewski, M. Juchert, D. Patchick, D. Riddle, J. Saloranta, M. Schoenball, C. Watson (2006). New galactic open cluster candidates from DSS and 2MASS imagery. *Astronomy & Astrophysics*, 447(3), 921-U53, doi:10.1051/0004-6361.



---

## ACKNOWLEDGMENTS

---

I have to be thankful to many people for their support during the work on this thesis.

Thank you to my supervisor Thomas Kohl who gave me a lot of trust and freedom to develop my own ideas but also encouraged and demanded me to take on new challenges. I could be sure of his absolute support in good and in difficult times.

I am thankful to Friedemann Wenzel for taking the responsibility of being co-examiner, and for stimulating discussions on science and seismicity.

Thanks to Frank Schilling for inspiring discussions and for numerous advice throughout my work.

Special thanks to Oliver Heidbach and Arno Zang for careful reviews of my research and for reflections from a broad perspective of geomechanics. Working with you was (and hopefully will be) a pleasure!

Thanks to Louis Dorbath for letting me work on his dataset and for his support in analyzing it.

Thanks to Birgit Müller and Emmanuel Gaucher for so many good discussions, for sharing your experience and your proofreading skills.

Thanks to GRACE and Klaus Regenauer-Lieb for providing me the opportunity to stay at CSIRO in Perth, which eventually turned out to be the most productive three months during the whole PhD project. Part of the fruit is due to Florian Wellmann through insights to uncertainty and Perth nightlife.

I thank all members of the Petrotherm working groups for an awesome working atmosphere, which kept me motivated when science was less motivating! Birgit's continuous supply of sweets contributed immeasurably to this thesis. Thanks to Caro for proofreading and the occasional cake. Bike rides with Fabian, Jörg, Niklas, Manuel, Sebastian and radsport\_KA prevented any weight gain, thanks for waiting after the downhills!

A big thank you is due to Silke Schlichting and Hannah Krause, who kept the working groups running!

Many thanks to Muriel for accompanying me through the highs and lows of the last years and until the Asian jungle. Finally, I thank my parents for their unconditional support in all aspects.

Merci beaucoup – Vielen Dank!